

August 16, 2013  
DRAFT

# Thermal Modeling of Disordered Materials

Jason M. Larkin

August 2013

School of Computer Science  
Carnegie Mellon University  
Pittsburgh, PA 15213

**Thesis Committee:**

Alan J. H. McGaughey, Chair  
Jonathan Malen  
Craig Maloney  
Michael Widom

*Submitted in partial fulfillment of the requirements  
for the degree of Doctor of Philosophy.*

Copyright © 2013 Jason M. Larkin

August 16, 2013  
DRAFT

**Keywords:** Phonon

## Acknowledgments

D) Acknowledgments must include financial support acknowledgment as discussed in Section 5

SED

This work is supported by AFOSR award FA95501010098. We thank John A. Thomas (Johns Hopkins University Applied Physics Laboratory) for helpful discussions.

VC

This work was supported by AFOSR award FA95501010098 and by a grant of computer time from the DOD High Performance Computing Modernization Program at the US Army Engineer Research and Development Center. We thank Davide Donadio, Jivtesh Garg, Asad Hasan, Ankit Jain, Craig Maloney, and Zhiting Tian for helpful discussions.

MFP

August 16, 2013  
DRAFT

August 16, 2013  
DRAFT

## **Abstract**

Thermal transport in ordered (crystalline) materials is well understood in terms of the phonon gas model. Theoretical formulations date back to... Theory has been compared extensively to experimental measurements, which typically leads to good quantitative agreement.(cite)

Disordering a crystal (i.e., alloying, amorphization, etc..) breaks down the phonon gas theory and a new theoretical formulation is necessary. Typically, theoretical formulations begin with perturbation theory, which is valid for weakly disordered systems. These perturbation theories lead to simple models which can be fit empirically to experimental measurements. However, predictive methods which do not rely on perturbation theory are still in active developed, particularly for use with *ab initio* computational techniques.

Why disordered materials are important... Thermal management (i.e., heat spreaders and thermal insulators) depends critically on accurate predictions of thermal conductivity. Often the scattering from defects and boundaries reduces the thermal conductivity in these materials and devices, which is still being understood. Recently, the search for more efficient thermoelectric materials has focused on reducing the thermal conductivity by alloying.

Thermal transport in alloys and amorphous materials is studied in this work using four predictive methods. Because disordering complicates the theory of thermal transport, each predictive method provides complimentary information which is compared wherever possible. By comparison, critical information about the vibrational mode-level properties is identified. Important assumptions about the nature of thermal transport in disordered materials are investigated using fully atomistic models. The predicted results are compared to phenomenological, empirical, and perturbative models. The results presented in this work provide a theoretical and computational framework for the study of emerging disordered and nanoscaled systems.

Disordered materials are

August 16, 2013  
DRAFT

August 16, 2013  
DRAFT

# Contents

<b>1</b>	<b>Introduction (WORK)</b>	<b>1</b>
1.1	Thermal Conductivity Theory . . . . .	1
1.1.1	Green-Kubo Formulation . . . . .	1
1.1.2	Kinetic Phonon Gas and Perturbation Theory . . . . .	1
1.1.3	Diffuson Theory . . . . .	3
1.1.4	Bottom-up versus Top-Down Thermal Conductivity . . . . .	4
1.1.5	Computational Cost and Modeling Choices . . . . .	6
<b>2</b>	<b>Vibrational Lifetimes from Molecular Dynamics</b>	<b>7</b>
2.1	Introduction . . . . .	8
2.2	Phonon Spectral Energy Density . . . . .	10
2.2.1	As Derived from Normal Mode Coordinates, $\Phi$ . . . . .	10
2.2.2	Formulation in the Time-Domain (WORK) (READ) . . . . .	11
2.2.3	Alternative Formulation, $\Phi'$ . . . . .	12
2.3	Computational Details . . . . .	13
2.3.1	Allowed Wavevectors . . . . .	13
2.3.2	Phonon Lifetimes and Frequencies (WORK) . . . . .	14
2.3.3	Thermal Conductivity . . . . .	15
2.3.4	Computational Cost and Work Flow Optimization (WORK) . . . . .	17
2.4	Case Studies . . . . .	19

2.4.1	Lennard-Jones Argon . . . . .	19
2.4.2	Stillinger-Weber Silicon . . . . .	23
2.4.3	Carbon Nanotube . . . . .	26
2.5	Summary . . . . .	26
<b>3</b>	<b>Predicting alloy vibrational mode properties using lattice dynamics calculations, molecular dynamics simulations, and the virtualcrystal approximation</b>	<b>29</b>
3.1	Introduction . . . . .	30
3.2	Theoretical and Computational Framework . . . . .	32
3.2.1	Thermal Conductivity Prediction . . . . .	32
3.2.2	Virtual Crystal Approximation . . . . .	33
3.2.3	Calculation and Simulation Details . . . . .	36
3.3	Vibrational Mode Properties in Alloys . . . . .	38
3.3.1	Density of States . . . . .	38
3.3.2	Dispersion and Group Velocity . . . . .	41
3.3.3	Lifetimes . . . . .	45
3.3.3.1	From VC-NMD and Gamma-NMD . . . . .	45
3.3.3.2	From VC-ALD . . . . .	49
3.3.4	Diffusivities . . . . .	53
3.3.5	Discussion . . . . .	56
3.4	Thermal Conductivity Prediction . . . . .	57
3.5	SW silicon . . . . .	61
3.6	Summary . . . . .	65
<b>4</b>	<b>Vibrational Mean Free Paths and Thermal Conductivity Accumulation Functions for Amorphous Materials</b>	<b>69</b>
4.1	Introduction . . . . .	69
4.2	Theoretical Formulation of Vibrational Thermal Conductivity . . . . .	72

4.3	Calculation Details . . . . .	75
4.3.1	Sample Preparation . . . . .	75
4.3.2	Simulation Details . . . . .	77
4.4	Vibrational Mode Properties . . . . .	78
4.4.1	Density of States . . . . .	78
4.4.2	Structure Factor . . . . .	79
4.4.3	Sound Speed . . . . .	82
4.4.4	Lifetimes . . . . .	85
4.4.5	Diffusivities . . . . .	87
4.5	Thermal Conductivity . . . . .	90
4.5.1	Bulk . . . . .	90
4.5.2	Accumulation Function . . . . .	96
4.6	Summary . . . . .	99
<b>5</b>	<b>Conclusion (WORK)</b>	<b>101</b>
5.1	Contributions . . . . .	101
5.1.1	Molecular Dynamics-based Methods for Predicting Vibrational Lifetimes	101
5.1.2	Thermal Transport in Alloys and High-scatter Limits . . . . .	101
5.1.3	Mean Free Paths of Propagating Modes in Amorphous Materials . . . . .	104
5.2	Future Work . . . . .	104
5.2.1	Large Unit Cell Crystals and Disordered Materials . . . . .	104
5.2.2	Computing Exact Normal Modes of Large Finite Systems . . . . .	105
5.2.3	Predicting Timescales from very Large-Scale Molecular Dynamics Simulations . . . . .	105
5.2.4	DFT and Thermal Modeling . . . . .	106
5.2.5	“Wrapper“ Package for Thermal Transport Calculations . . . . .	106

<b>A Normal Mode Decomposition Technique and Computational Details</b>	<b>109</b>
A.1 Derivation of Phonon Spectral Energy Density, $\Phi$ (WORK,READ) . . . . .	109
A.2 Interpretation of $\Phi'$ (WORK,READ) . . . . .	114
A.3 Unit Cell and Supercell Representations (WORK) . . . . .	115
A.3.1 Primitive and Conventional Unit Cells (WORK) . . . . .	115
A.3.2 Crystal Symmetries (WORK) . . . . .	116
A.3.3 Primitive, Conventional, and Supercell Representations using Normal Mode Decomposition (WORK) . . . . .	118
A.4 NMD using Non-Exact Normal Modes (WORK) . . . . .	121
A.5 Effect of Metastability for Amorphous Solids on Normal Mode Decomposition (WORK) . . . . .	123
A.6 Finite Simulation-Size Scaling for Thermal Conductivity (WORK) . . . . .	130
<b>B Research using High Performance Computing (WORK)</b>	<b>133</b>
B.1 Setting Up Computing Environment . . . . .	133
B.1.1 Hardware and Operating System Choice . . . . .	133
B.1.2 Linux/Unix Terminal, Commands, and Environment Variables . . . . .	134
B.1.3 Working on Remote Resources . . . . .	135
B.2 Installing, Writing and Executing Programs . . . . .	136
B.2.1 Installing Available Packages . . . . .	136
B.2.2 Available Programs and Packages for Thermal Transport Modeling . . . . .	137
B.2.3 Writing Programs . . . . .	138
B.2.3.1 Coding Languages: Compiled versus Interpreted . . . . .	138
B.2.3.2 Case-study(a): Compiled Language, Lennard-Jones Argon Molec- ular Dynamics . . . . .	138
B.2.3.3 Compiled versus Interpreted Case-study(b): Lennard-Jones Dis- persion . . . . .	141

B.2.3.4 Compiled versus Interpreted Case-study(c): Allen-Feldman Diffusivity Calculation . . . . .	141
B.2.4 Executing Programs . . . . .	143
B.2.4.1 Executing Locally: Rapid Development . . . . .	143
B.2.4.2 Executing Remotely: Portable Batch Systems . . . . .	143
B.2.4.3 Scaling Calculations . . . . .	143
B.3 Preparing Journal Articles and Thesis . . . . .	144
B.3.1 Journal Articles . . . . .	144
B.3.2 Thesis . . . . .	145
B.3.3 Producing Figures . . . . .	145
B.4 Technical Advice . . . . .	145
B.4.1 Expert Advice . . . . .	145
B.4.2 Online Resources . . . . .	146
<b>Bibliography</b>	<b>147</b>
Contents	

August 16, 2013  
DRAFT

# List of Figures

2.5 Comparison of the phonon frequencies and lifetimes predicted using $\Phi(\omega, \tau)$ and $\Phi'(\omega', \tau')$ for a (8,8) CNT modeled using the REBO potential. The phonon frequencies agree well, while the phonon lifetimes show large scatter. . . . .	27
3.1 (a) Explicitly disordered supercell of Si and “heavy” Si ([100] direction into the paper). [1] (b) Equivalent VC supercell with one averaged mass. The sphere size represents increasing mass only, no bond disorder is considered. The 8-atom conventional cubic unit cell is shown in (b). . . . .	36
3.2 (a) Explicitly disordered alloy supercell of silicon and “heavy” silicon ([100] direction into the page). [1] (b) Equivalent VC supercell with one averaged mass. The sphere size represents increasing mass only, no bond disorder is considered. The 8-atom conventional cubic unit cell is shown in (b). . . . .	37
3.3 Vibrational DOS for LJ alloys calculated using the VC approximation and an explicitly disordered supercell (labeled Gamma) for concentrations of (a) 0.05, (b) 0.15, and (c) 0.5. VC and Gamma show similar low-frequency behavior for all concentrations. For increasing concentrations, the frequencies of both VC and Gamma decrease, while the high frequency DOS for Gamma spreads and reaches to a higher maximum frequency because of the explicit disorder. The supercells are of size $N_0 = 12$ (6,912 atoms). . . . .	40
3.4 Left and right panels: The structure factor for longitudinal ( $S_L$ ) and transverse ( $S_T$ ) polarizations along high-symmetry directions of the mass disordered LJ argon supercells ( $N_0 = 10$ , $c = 0.05, 0.5$ ). Center panels: The VC predicted dispersion curves (solid lines) agree well with the locations of the peaks in $S_L$ and $S_T$ (data points). The wavenumber axis in the center panel is normalized by the maximum value of the wavenumber in the given direction. . . . .	44

3.5 Lifetimes predicted using VC-NMD and Gamma-NMD from MD simulations of (a) perfect LJ argon and (b),(c),(d) mass-disordered LJ alloys for $N_0 = 10$ . $\omega^{-2}$ and $\omega^{-4}$ scalings are observed at low to mid frequencies. For both VC-NMD and Gamma-NMD, most mode lifetimes are greater than the Ioffe-Regel limit of $2\pi/\omega$ . [2] While there is more scatter in the Gamma-NMD data (see Section 3.3.3.1), the lifetime magnitudes and trends agree well, an important consideration when comparing the VC-NMD and VC-ALD lifetimes in Fig. 3.6(a). . . . .	48
3.6 (a) Predicted lifetimes using VC-NMD and VC-ALD for LJ argon ( $T = 10$ K, $N_0 = 10$ , and $c = 0.05$ ). (b) Mode diffusivities compared to the high-scatter limit, $D_{HS}$ [Eq. (3.18)], and IR limit, $D_{IR}$ [Eq. (3.19)]. VC-NMD and VC-ALD predict a large number of high-frequency modes with $D_{ph} < D_{HS}$ . (c) Thermal conductivity frequency spectrum, which peaks at high frequency, in contrast to SW silicon [(Fig. 3.9(c))]. . . . .	52
3.7 AF theory predictions of disordered mode diffusivities for LJ argon alloy and amorphous phases. The amorphous phase is well-described by a mode-independent diffusivity $D_{HS}$ [Eq. (3.18)]. The system size for the alloy is $N_0 = 10$ (6,912 atoms), and the amorphous phase has 6,912 atoms. . . . .	55
3.8 Thermal conductivity predictions for LJ argon and alloys at $T=10$ K using the VC-NMD, VC-ALD, and GK methods. The high-scatter thermal conductivity prediction $k_{HS}$ [Eq. (3.3)] and the high-scatter adjusted VC-NMD* and VC-ALD* are also plotted. . . . .	59
3.9 (a) Predicted lifetimes using VC-NMD and VC-ALD for SW silicon ( $T = 300$ K, $N_0 = 8$ , and $c = 0.05$ ). (b) Mode diffusivities compared to the high-scatter limit, $D_{HS}$ [Eq. (3.18)], and the IR limit, $D_{IR}$ [Eq. (3.19)]. VC-NMD and VC-ALD predict a large number of high-frequency modes with $D_{ph} < D_{HS}$ , as seen in the LJ argon alloys [Fig. 3.6(b)]. (c) Thermal conductivity frequency spectra, which peak at low frequency, in contrast to LJ argon [Fig. 3.6(c)]. . . . .	63

3.10 Thermal conductivity predictions for SW silicon and alloys at a temperature of 300 K using the VC-ALD and GK methods. The high-scatter thermal conductivity prediction $k_{HS}$ is also plotted. The adjusted VC-ALD* is not shown since it differs by less than one percent compared to VC-ALD.	64
3.11 The normal mode kinetic energy, $\Phi$ , of two modes (A and B) at wavevector [0.25 0 0] calculated using VC-NMD for a mass disordered LJ FCC supercell ( $N_0 = 8$ and $c = 0.5$ ) is shown in the main figure. The VC dispersion-predicted peaks are labeled by $\omega_0$ . The inset shows the same mode's energy [kinetic ( $KE$ ) and total ( $TE$ )] autocorrelation functions. Note the additional oscillation effects in the KE and TE autocorrelation functions for Mode B which are due to the two peaks in $\Phi$ . A mode lifetime can be extracted unambiguously using the integral of the TE autocorrelation function [Eq. (3.11) in Section 3.3.3.1].	67
4.1 (a) Small sample of a-SiO <sub>2</sub> created from a melt-quench technique showing the Si-O tetrahedral bond network. Bond lengths range between 1.6 and 1.8 Å. (b) Small sample of a-Si created by the modified WWW algorithm. Bond lengths range between 2.3 and 2.7 Å. Visualizations using the VESTA package.[1]	76
4.2 Vibrational DOS of a-SiO <sub>2</sub> and a-Si plotted on a log-log scale. Both models show an $\omega^{-2}$ scaling at low frequency. The DOS for a-Si has two peaks similar to the DOS of the crystalline phase.[3] The DOS for a-SiO <sub>2</sub> is flat over most of the spectrum, with a high frequency gap that separates the Si-O interactions.[4]	79
4.3 Longitudinal (left panel) and transverse (right panel) structure factors [Eq. (4.12)] for (a) a-SiO <sub>2</sub> and (b) a-Si. The wavevectors are normalized by $\kappa_{max} = 2\pi/a$ , where $a$ is 4.8 (a-SiO <sub>2</sub> ) and 5.43 (a-Si) Å, based on the lattice constants of the crystalline phases. [5, 6]	82

- 4.4 Vibrational mode lifetimes predicted by NMD [Eq. (4.22)] and the structure factors [Eq. (4.15)] for (a) a-SiO<sub>2</sub> and (b) a-Si. The NMD-predicted lifetimes are larger than the IR limit. The lifetimes predicted from the structure factors fall below the IR limit at high-frequency for a-Si and for all frequencies for a-SiO<sub>2</sub>. For a-Si, a clear  $\omega^{-2}$  scaling is observed at low frequencies, while the lifetimes plateau at higher frequencies, over a wider range of frequencies than for a-SiO<sub>2</sub>, with two peaks corresponding to the peaks in the DOS (Fig. 4.2). The transition from the low-frequency scaling to the plateau region for a-Si occurs near  $10^{13}$  rads/s, which corresponds to where the DOS first peaks in Fig. 4.2. . . . . 88
- 4.5 Vibrational mode diffusivities predicted from NMD [using Eqs. (4.5) and (4.22) with the DOS sound speed from Table 4.1] and the AF theory [Eq. (4.10)]. Also shown are extrapolations based on an  $\omega^{-2}$  scaling with Eqs. (4.5) and (4.8) for a-SiO<sub>2</sub> and a-Si, and an additional  $\omega^{-4}$  scaling for a-Si. For both systems, the diffusivities are larger than the high-scatter limit [Eq. (4.23)] except at high frequencies, where the modes are localized. . . . . 91
- 4.6 Thermal conductivities of a-SiO<sub>2</sub> and a-Si predicted using the GK method and Eq. (4.1). For a-SiO<sub>2</sub>, the GK-predicted thermal conductivity is size-independent, indicating that there is not an important contribution from propagating modes. For a-Si, there is a clear size dependence, indicating the importance of propagating modes. . . . . 94

- 4.7 (a) Predicted thermal conductivity accumulation function [Eq. (4.26)] for a-SiO<sub>2</sub> compared with experimental broadband frequency domain reflectance measurements by Regner et al.[7] and thin film measurements from Refs. 8 and 9. The predicted thermal conductivity accumulation demonstrates that the propagating contribution is negligible in our model, which is in accord with the experimental measurements. (b) Predicted thermal conductivity accumulation function for a-Si compared with experimental measurements by Regner et al. and thin film measurements fabricated by sputtering (Expt. A) [10, 11, 12] and chemical vapor deposition (Expt. B) [13, 14, 15, 16] for a range of film thicknesses. The predicted thermal conductivity accumulation demonstrates that the propagating contribution is significant for a-Si. We note that thermal conductivities as high as 6 W/m-K (not plotted) have been measured for a-Si thin films deposited using hot-wire chemical vapor deposition.[16] . . . . . 98

- A.1 Dispersion curves and full Brillouin zone density of states for a LJ crystal at a dimensionless temperature of 0.0827. (a) [100] and [111] dispersion curves and density of states based on the primitive (i.e., one atom) unit cell. (b) [100] and [111] dispersion curves and density of states based on the conventional (i.e., four atom) unit cell. The harmonic lattice dynamics calculations are performed using a resolution of sixteen wave vectors along the reciprocal lattice vectors of the conventional unit cell. The red and blue dots in (b) are the modes considered in Fig. 2.1. . . . . 125
- A.2 Lennard-Jones lifetimes from a  $N_0 = 10$  system at a temperature of 0.0827 predicted from normal mode decomposition analysis on (a) the primitive and conventional unit cells, and (b) treating the simulation cell as the unit cell (i.e., Gamma-point analysis). All lifetimes extracted from time-domain analysis. . . . 126

A.3 Size dependence of thermal conductivity for the LJ crystal at a temperature of 0.0827 from normal mode decomposition and the Green-Kubo method. . . . .	127
A.4 Virtual crystal (a) frequency-domain and (b) time-domain normal mode decomposition analysis for two modes in LJ alloys with concentrations of 0.05 and 0.5. For modes that are not well-approximated by the virtual crystal modes, the lifetime can be approximated using Eq. (??), as shown in (d). . . . .	128
A.5 (a) Time-domain and (b) frequency domain normal mode decomposition analysis for two modes in an amorphous LJ solid at a dimensionless temperature of 0.0413. . . . .	129
A.6 Lifetimes predicted by normal mode decomposition for an amorphous LJ phase at a dimensionless temperature of 0.0413. The lifetimes for the crystal at a dimensionless temperature of 0.0827 are provided for comparison. . . . .	129
A.7 Thermal conductivity predictions for LJ argon calculated using phonon lifetimes predicted by $\Phi$ and $\Phi'$ . (a) The finite simulation-size scaling extrapolation [17, 18] is used to compare the results to bulk predictions made using the Green-Kubo method. (b) The bulk results for $\Phi$ and Green-Kubo are in good agreement temperatures of 20 and 40 K with those of other atomistic simulation methods,[17] while those from $\Phi'$ differ (see Table 3.1). . . . .	131

August 16, 2013  
DRAFT

# List of Tables

1.1 Qualitative comparison of theoretical techniques for predicting vibrational mode properties and thermal conductivity. . . . .	5
2.1 Thermal conductivity values in W/m-K predicted using the $\Phi$ , $\Phi'$ , and Green-Kubo methods. The predictions for $\Phi$ and Green-Kubo for the LJ system are in good agreement with those from other atomistic simulation methods [17] while those from $\Phi'$ differ and show no consistent behavior. The uncertainties in the predicted thermal conductivities for $\Phi$ and $\Phi'$ come predominantly from the finite simulation-size scaling procedure (see Ref. [17, 18]), where the phonon properties and thermal conductivity are predicted for increasing system sizes ( $N_1 = N_2 = N_3$ ) to extrapolate a bulk thermal conductivity. For SW silicon and the CNT, the extrapolation procedure is not performed. . . . .	24
3.1 Thermal conductivity predictions using the VC-NMD, VC-ALD, and GK methods. For LJ argon alloys, the bulk extrapolation is used for all three methods. For SW silicon alloys, only VC-ALD and GK can be used to extrapolate a bulk thermal conductivity (see Section 3.4). For VC-NMD and GK, the uncertainties are estimated by omitting independent simulations from the ensemble averaging (see Section 4.3). For VC-ALD, the uncertainties are estimated by omitting extrapolation points used for Eq. (3.21). . . . .	60

4.1 Longitudinal and transverse sound speeds in m/s estimated from the elastic moduli [Eqs. (4.17) and (4.18)], structure factors [Eq. (4.16)], and DOS [Eq. (4.3)]. The pre-annealed group velocities predicted by the elastic constants are labeled as Moduli*. . . . .	85
4.2 Thermal conductivities for bulk a-SiO <sub>2</sub> and a-Si predicted by the GK method ( $k_{GK}$ ) and Eqs. (4.1) ( $k_{vib}$ ), (4.2) ( $k_{pr}$ ), and (4.9) ( $k_{AF}$ ). For the non-propagating contribution, classical and quantum specific heats are considered. . . . .	95
5.1 Available packages . . . . .	106
A.1 The unit cell for a face-centered cubic crystal can be chosen in different ways. . .	117

# Chapter 1

## Introduction (WORK)

There are two sections to this introductory chapter.

Crystals well understood, except for brand-new stuff(cite broido, esfajani)

Disordered materials, what is known or unknown.

Physics community lots of studies, but nothing pushing the towards thermal.

Kinetic Theory

Callaway/Holland-type

### 1.1 Thermal Conductivity Theory

#### 1.1.1 Green-Kubo Formulation

Discussed in other works.

#### 1.1.2 Kinetic Phonon Gas and Perturbation Theory

For a perfect lattice, all vibrational modes are phonon modes, which by definition are delocalized, propagating plane waves. [19] Using the single-mode relaxation time approximation [19] to solve the Boltzmann transport equation gives an expression for thermal conductivity kph Eq. 3.1.

The relaxation time approximation has been found to be valid for lower thermal conductivity materials (e.g., Si and SiGe alloys), [20, 21, 22] while larger thermal conductivity materials such as GaN and diamond require an iterative solution to the BTE for more accurate predictions using Eq. (3.1). [23, 24]

In the VC-ALD method, the phonon-phonon scattering is predicted using ALD.[17, 25] with phonon-phonon and phonon-defect scattering treated as perturbations. [22, 24, 26] Phonon-phonon scattering in ALD is modeled by including three-phonon processes.[22, 26, 27] The present study is concerned with temperatures much less than the melting temperature of either LJ argon [28] or SW silicon[6] so that we believe the effects of higher-order phonon processes are negligible.[27, 29] We predict the phonon-phonon lifetimes using the method described in Ref. 27, with all classical expressions for the populations to remain consistent with the classical MD-based methods from Section 3.3.3.1.

The phonon-defect scattering is treated using perturbative methods that can handle mass and/or bond disorder. [30, 31, 32, 33] Using perturbation theory, Tamura derived a general expression for phonon scattering by mass point defects to second order that was applied to study isotopic germanium.[33] Bond disorder can be accounted for using a similar expression with an average atomic radius or suitable scattering cross-section. [30, 31] In  $\text{Ni}_{0.55}\text{Pd}_{0.45}$ , which has a large mass ratio (1.8) and concentration of each species, experimental measurements of vibrational frequencies and linewidths agree well with predictions from the perturbative mass-disorder theory. [32, 33, 34]

Using DFT methods to predict the mode-specific phonon properties of the VC, Lindsay and Broido found good agreement between VC-ALD and experimental measurements of thermal conductivity for isotopically defected GaN (the gallium isotopes have concentrations of 0.6 and 0.4 and a mass ratio of 1.03).[24] Garg et al. used DFT calculations with VC-ALD to predict the thermal conductivity of SiGe alloys for all concentrations at a temperature of 300 K, obtaining good agreement with experiment.[22] By including disorder explicitly in their ALD calculations, the predicted thermal conductivity decreased by 15%. Isotopically-defected GaN and low con-

centration SiGe alloys have relatively large thermal conductivities at a temperature of 300 K ( $\sim$  100 W/m-K). Li et al. used DFT calculations with VC-ALD to predict the thermal conductivity of  $Mg_2Si_xSn_{1-x}$  ( $\sim$  10 W/m-K) in good agreement with experimental measurements for all concentrations.[35] The VC-ALD approach has also been used to predict the effect of interfacial mixing in GaAs/AlAs superlattices, but the thermal conductivity predictions were not compared with experimental measurements.[36] In our survey of experimental measurements and numerical modeling, we find that VC predictions tend to be accurate when the disordered lattice thermal conductivity is significantly above the high-scatter limit [Eq. (3.3)], which tends to be around 1 W/m-K. [22, 24, 34, 37, 38, 39, 40]

An ALD study using phonon properties from DFT calculations for crystalline PbTe[41] predicted thermal conductivities of 2 W/m-K at a temperature of 300 K in fair agreement with experiment. For PbTeSe alloys, a VC-ALD study predicted a small thermal conductivity reduction compared to the perfect crystals.[26] Experimental results are limited for these alloys,[42, 43] making it difficult to asses the validity of the VC-ALD approach for materials whose thermal conductivities approach the high-scatter limit.

Given all these results, it is unclear what limitations exist for using the VC approach. In this study, we will consider a low thermal conductivity alloy using the LJ potential and a high thermal conductivity alloy using the SW potential. The computational studies discussed above were limited to VC-ALD because of DFT calculation costs. Our use of computationally inexpensive empirical potentials allows us to include the disorder explicitly and as a perturbation and to compare the predictions.

### 1.1.3 Diffuson Theory

For disordered systems, the vibrational modes are no longer pure plane-waves (i.e., phonon modes), except in the low-frequency (long-wavelength) limit. When applied in the classical limit, the Allen-Feldman (AF) theory computes the contribution of diffusive, non-propagating

modes (i.e., diffusons) to thermal conductivity.[44]

kAF Eq. (3.2) The diffusivity of diffusons can be calculated from harmonic lattice dynamics theory. [44, 45, 46]

Assuming that all vibrational modes travel with the sound speed,  $v_s$ , and scatter over a distance of the lattice constant,  $a$ , a high-scatter (HS) limit of thermal conductivity in the classical limit is[40]

$$k_{HS} = \frac{k_B}{V_b} b v_s a, \quad (1.1)$$

where  $V_b$  is the volume of the unit cell and  $b$  is the number of atoms in the unit cell. The HS limit will be used to discuss the differences between the LJ argon and SW silicon alloys.

Harmonic theory

Does not work at low-frequencies

#### **1.1.4 Bottom-up versus Top-Down Thermal Conductivity**

Callaway-Holland (CH) theory uses empirically fit models for the mode properties. The CH empirical models can be used together with harmonic lattice dynamics calculations on atomistic models based on interatomic potentials or DFT calculations.

Because empirically fit models are used, the CH theory lacks predictive capability.

Anharmonic lattice dynamic (ALD) can be used to predict phonon properties without the need for empirical fitting.

Allen-Feldman (AF) theory

MD-based Green-Kubo (GK) method

normal mode decomposition (NMD)

Comments

Callaway/Holland model: Challenging to apply to non-isotropic systems. Requires fitting parameters.

Table 1.1: Qualitative comparison of theoretical techniques for predicting vibrational mode properties and thermal conductivity.

	CH Theory	ALD	AF Theory	GK	NMD
Description	Empirical	Predictive	Predictive	Predictive	Predictive
Input	Empirical Models, dispersion and lifetime models, experimental $k$ data	Force constants (classical or DFT)	Force constants (classical or DFT)	Forces (classical or DFT)	
Temperature	All	Low	All	All	Mid-range
Disorder	As additional perturbation	As additional perturbation	Can be naturally included	stuff	
Anharmonicity	Full	Third-order	Full	Harmonic	Quasi-Harmonic
Statistics	Bose-Einstein or Boltzmann	Bose-Einstein or Boltzmann	Boltzmann	Bose-Einstein or Boltzmann	Boltzmann
Mode Range	Low-frequency	All-frequency (crystal), low-frequency (alloy)		stuff	

ALD Partial fourth-order theory for predicting frequency shifts available. Calculation scales with the fourth power of the number of atoms in the unit cell.

Requires *a priori* harmonic lattice dynamics calculations. Can also predict  $k$  from the mode-level properties.

The Allen-Feldman (AF) theory can use quantum or classical expressions for the specific heat, while the mode properties it predicts are based on the harmonic approximation. While this should limit the applicability of the AF theory to low temperatures where the harmonic approximation is valid, anharmonic effects have been shown to be small for disordered solids such as amorphous silicon. [45]

NMD Mid-range[27]

### 1.1.5 Computational Cost and Modeling Choices

The key to explicitly incorporating the effects of disorder is to use large disordered supercells.

Efficient MD codes like LAMMPS scale linearly with the number of atoms in the system,  $N_a$ , which makes the GK method (see Section 3.4) computationally-inexpensive when used with empirical potentials.

## Chapter 2

# Vibrational Lifetimes from Molecular Dynamics

Two frequency-domain methods for predicting phonon frequencies and lifetimes using the phonon spectral energy density are described. Both methods draw input from molecular dynamics simulations and lattice dynamics calculations, but differ in the form of the phonon spectral energy density. One phonon spectral energy density expression (referred to as  $\Phi$ ) can be formally derived from lattice dynamics theory. A similar approach in the time domain has been validated [Turney et al. *Phys. Rev. B* **79**, 224305 (2009)]. The other phonon spectral energy density expression (referred to as  $\Phi'$ ) has been proposed [Thomas et al., *Phys. Rev. B* **81**, 081411(R) (2010)] but not validated. The expressions for  $\Phi$  and  $\Phi'$  are presented and then applied to predict the phonon properties and thermal conductivities of three systems: Lennard-Jones argon, Stillinger-Weber silicon, and a carbon nanotube modeled using the Reactive Empirical Bond Order potential.  $\Phi'$  does not capture the total phonon spectral energy density predicted by  $\Phi$  and therefore cannot correctly predict the phonon lifetimes or thermal conductivity. Its use in future work is discouraged and we recommend the use of  $\Phi$ .

## 2.1 Introduction

Phonons are the dominant carriers of thermal energy in dielectric and semiconducting crystals [47, 48, 49, 50, 51, 52]. While substantial effort has been devoted to developing theories of phonon transport, the current understanding is incomplete, even in bulk materials. For example, which phonon modes dominate thermal energy transport and the importance of interactions involving four or more phonons are still being investigated [20, 25, 47, 49, 50]. The situation becomes more complicated in nanostructures, where the phonons also interact with free surfaces and interfaces [3, 8, 18, 53, 54, 55, 56, 57, 58, 59, 60, 61, 62].

Analytical models of thermal transport, such as the Debye model, are limited by the necessary approximations and assumptions [60, 63, 64]. With the Green-Kubo or non-equilibrium direct methods, molecular dynamics (MD) simulations can be used to predict thermal conductivity, but only in a classical (i.e., high-temperature) framework [17, 25, 59, 65, 66, 67, 68]. Because the analysis in these two MD-based methods is performed at the system level, no information about the phonons is obtained. Phonon specific heats, group velocities, and lifetimes are the required inputs for predicting thermal conductivity at the phonon-mode-level using Boltzmann transport equation-based models [17, 18, 25, 60, 65, 66, 68]. These phonon properties can be predicted using harmonic and anharmonic lattice dynamics calculations [17, 50, 52, 65, 69, 70], where quantum statistical effects can be naturally included. Anharmonic lattice dynamics calculations are limited to three-phonon scattering events, however, and are thus only valid at low temperatures [17, 25, 49, 50].

At high temperature, four-phonon and higher-order processes become important to thermal transport [17, 25, 49, 50]. All orders of phonon processes are present in a MD simulation as the positions and momenta of the atoms are evolved using the full anharmonicity of the interatomic interactions [25, 66]. Phonon properties can be predicted from a MD simulation using normal mode analysis in the time domain [17, 18, 65, 66, 71, 72]. In Section 2.2.1, we will describe how this approach can be performed in the frequency-domain using the phonon spectral energy

density (SED, referred to as  $\Phi$ ). An alternative expression for the phonon SED (referred to as  $\Phi'$ ), was recently proposed but has not been rigorously tested [73, 74, 75].  $\Phi'$  was first used to predict the phonon dispersion curves of carbon nanotubes (CNTs) [73]. Thomas et al. used  $\Phi'$  to predict the phonon lifetimes and thermal conductivity of isolated and water-filled CNTs, obtaining good agreement with other atomistic predictions [75]. The phonon lifetime reductions speculated for water-filled CNTs [75] and CNTs on  $\text{SiO}_2$  substrates [76] suggest that  $\Phi'$  captures phonon physics at least qualitatively. The phonon lifetimes and thermal conductivity for  $\text{PbTe}$  [77] and Half Heusler alloys [78] have also been predicted using  $\Phi'$ . De Koker predicted the phonon lifetimes and thermal conductivity for  $\text{MgO}$  using an expression similar to  $\Phi'$  (but different than  $\Phi$ ) [79]. Another recent atomistic study using Stillinger-Weber silicon predicted phonon lifetimes using both  $\Phi$  and  $\Phi'$ , but a detailed comparison of the predictions between the two was not performed [80].

The objective of this work is to assess the validity of  $\Phi'$  as a phonon SED by comparing the phonon properties it predicts to those predicted by  $\Phi$ . In Section 2.2.1, we present the correct phonon SED ( $\Phi$ ), which requires the phonon mode eigenvectors. The expression for  $\Phi$  is well-defined theoretically and has been tested and validated in previous studies in the time domain [17, 65]. In Section 2.2.3, we present the proposed alternative expression for the phonon SED,  $\Phi'$ , which does not require the phonon mode eigenvector [75]. Phonon frequencies, lifetimes, and thermal conductivities are then predicted and compared using  $\Phi$  and  $\Phi'$  for three test systems: Lennard-Jones (LJ) argon [81] in Section 2.4.1, Stillinger-Weber (SW) silicon [6] in Section 2.4.2, and an (8,8) CNT modeled with the reactive empirical bond order (REBO) potential [82] in Section 2.4.3. While  $\Phi'$  is found to accurately predict the phonon frequencies, we find that it does not correctly predict the phonon lifetimes because it does not capture the total phonon spectral energy density.

## 2.2 Phonon Spectral Energy Density

### 2.2.1 As Derived from Normal Mode Coordinates, $\Phi$

The correct expression for the phonon SED,  $\Phi$ , can be derived from the formulation of anharmonic lattice dynamics theory [49, 50, 51, 52]. As shown in Appendix A.1, the phonon SED at wavevector  $\kappa$  is a function of frequency,  $\omega$ , and is given by

$$\Phi(\kappa, \omega) = \sum_{\nu}^{3n} C_0(\nu) \frac{\Gamma(\nu) / \pi}{[\omega_0(\nu) - \omega]^2 + \Gamma^2(\nu)}, \quad (2.1)$$

which is a superposition of  $3n$  Lorentzian functions with centers at  $\omega_0(\nu)$  and linewidths  $\Gamma(\nu)$  (one for each polarization,  $\nu$ ). The  $C_0(\nu)$  terms are mode-dependent constants. For simplicity, we refer to  $\Phi(\kappa, \omega)$  as  $\Phi$ . The kinetic energy normal mode coordinate,  $\dot{q}(\nu; t)$ , is [52]

$$\dot{q}(\nu; t) = \sum_{\alpha, b, l}^{3n, N} \sqrt{\frac{m_b}{N}} \dot{u}_{\alpha}(b; t) e^*(\nu \alpha) \exp[i\kappa \cdot \mathbf{r}_0(l)], \quad (2.2)$$

where  $e(\nu \alpha)$  are the components of the time-independent phonon mode eigenvector (see Section 2.3.2),  $n$  is the number of atoms in the unit cell,  $m_b$  is the mass of the  $b^{\text{th}}$  atom in the unit cell and  $\mathbf{r}_0(l)$  is the equilibrium position vector of the  $l^{\text{th}}$  unit cell. There are  $N$  total unit cells and  $\dot{u}_{\alpha}(b; t)$  is the  $\alpha$ -component of the velocity of the  $b^{\text{th}}$  atom in the  $l^{\text{th}}$  unit cell at time  $t$ .

Given a set of atomic velocities from MD simulation and the phonon mode eigenvector,  $\Phi$  can be calculated using

$$\Phi(\kappa, \omega) = 2 \sum_{\nu}^{3n} T(\nu; \omega) = 2 \sum_{\nu}^{3n} \lim_{\tau_0 \rightarrow \infty} \frac{1}{2\tau_0} \left| \frac{1}{\sqrt{2\pi}} \int_0^{\tau_0} \dot{q}(\nu; t) \exp(-i\omega t) dt \right|^2, \quad (2.3)$$

and then fit using Equation (2.1) to extract the phonon properties  $\omega_0(\nu)$  and  $\Gamma(\nu)$ . The phonon lifetime,  $\tau(\nu)$ , is defined as  $1/[2\Gamma(\nu)]$ . In practice,  $\tau_0$  should be much larger than the longest phonon lifetime and the continuous fourier transform in Equation (2.3) is performed using a

discrete fast fourier transform (see Section 2.4.1, 2.4.2 and 2.4.3).

## 2.2.2 Formulation in the Time-Domain (WORK) (READ)

Previous work using normal mode analysis has represented the phonon energy in the time domain [17, 18, 65, 66, 71, 72], while  $\Phi$  is a representation of the phonon energy in the frequency domain. The time- and frequency-domain approaches are mathematically equivalent by use of the Wiener-Khinchin theorem [78, 83], which applied to Eq. (2.1) gives

$$\frac{T(\kappa; t) T(\kappa; 0)}{T(\kappa; 0) T(\kappa; 0)} = \cos^2[\omega_a(\kappa) t] \exp[-2\Gamma(\kappa) t]. \quad (2.4)$$

The frequency-domain approach using the normal mode kinetic energy has the advantage of predicting both the phonon lifetime and frequency by fitting a simpler function than is required in the time-domain approach.

The time-domain approach can be simplified by calculating the potential energy normal mode coordinate,  $q(\kappa; t)$ ,

$$q(\kappa; t) = \sum_{b,l} \left( \frac{m_b}{N} \right)^{1/2} \exp[i\kappa \cdot \mathbf{r}_0(l)] \mathbf{e}_b^*(\kappa) \cdot \mathbf{u}_b(l; t), \quad (2.5)$$

and using it to calculate the total normal mode energy,  $E(\kappa; t)$ . The autocorrelation of the total normal mode energy is  $E(\kappa; t)$  [Eq. (A.6)]

$$\frac{E(\kappa; t) E(\kappa; 0)}{E(\kappa; 0) E(\kappa; 0)} = \exp[-2\Gamma(\kappa) t], \quad (2.6)$$

where  $\omega_a$  is the anharmonic frequency (as opposed to that predicted from harmonic lattice dynamics) and  $\Gamma(\kappa)$  is the line width, equal to  $1/[2\tau(\kappa)]$ .<sup>\*</sup> Thus, one can find the lifetime by fitting the normalized autocorrelation of the mode total energy to an exponential decay. Instead of

<sup>\*</sup>The factor of two in the relationship between the line width and the lifetime arises because the analysis is performed on the normal mode energy and not on the normal mode coordinate.

fitting an exponential function, the lifetime can be approximated as

$$\tau(\boldsymbol{\nu}) = \int_0^\infty \frac{E(\boldsymbol{\nu}; t) E(\boldsymbol{\nu}; 0)}{E(\boldsymbol{\nu}; 0) E(\boldsymbol{\nu}; 0)} dt, \quad (2.7)$$

an expression that is beneficial when studying disordered systems (see Section 3.3.3.1 and Appendix A.4).

### 2.2.3 Alternative Formulation, $\Phi'$

We now seek to motivate the expression  $\Phi'$  that was proposed in previous studies and examined in Chapter 2, but has not been validated [73, 74, 75]. Thomas et al. [75] define

$$\Phi'(\boldsymbol{\kappa}, \omega) = \frac{1}{4\pi\tau_0} \sum_{\alpha}^3 \sum_b^n \frac{m_b}{N} \left| \sum_l^N \int_0^{\tau_0} \dot{u}_{\alpha}(l; t) \exp[\Theta] dt \right|^2, \quad (2.8)$$

where  $\Theta \equiv i[\boldsymbol{\kappa} \cdot \mathbf{r}_0(l) - \omega t]$ . Thomas et al. [75] claim that  $\Phi'$  represents the phonon SED. As seen in Eqs. (??) and (2.2), the phonon mode eigenvectors are necessary to properly map between the atomic velocities and the normal mode coordinates. This need for the eigenvectors is the essential difference between the expressions for  $\Phi$  and  $\Phi'$ . The potential advantage of  $\Phi'$  is that other than the wavevectors, which can be determined from the crystal structure, no phonon properties need to be known *a priori*. However, to identify the degenerate modes in  $\Phi'$ , the phonon frequencies are necessary (see Section 2.3.2). Since  $\Phi'$  does not require the phonon mode eigenvector, it can (in principle) be used to study disordered systems or perturbed crystalline systems (e.g. dilute alloys [78], water-filled CNTs [75], and CNTs on substrates [76]). Despite its use in previous studies,  $\Phi'$  has not been rigorously validated. The interpretation of Eq. (2.8) is investigated in Appendix A.2. For simplicity, we refer to  $\Phi'(\boldsymbol{\kappa}, \omega)$  as  $\Phi'$ . Given a set of atomic velocities, Thomas et al. extract the phonon properties  $\omega_0(\boldsymbol{\nu})$  and  $\tau(\boldsymbol{\nu})$  from Equation (2.8) by fitting  $\Phi'$  for a given wavevector to a superposition of Lorentzian functions.

## 2.3 Computational Details

### 2.3.1 Allowed Wavevectors

Now that we have presented the two expressions for the phonon SED, we will provide the computational details of how they can be evaluated and used to predict phonon properties. The SED is defined for the allowed wavevectors of a crystal, which can be specified from the crystal structure's Bravais lattice, its basis (i.e., unit cell), and the size of the computational domain. A  $D$ -dimensional Bravais lattice is a collection of points with positions

$$\mathbf{r}_0(l) = \sum_{\alpha}^D N_{\alpha} \mathbf{a}_{\alpha}, \quad (2.9)$$

where  $\mathbf{a}_{\alpha}$  are the lattice vectors and  $N_{\alpha}$  is an integer [52]. The unit cell is the building block of the crystal and is placed on the points defined by the Bravais lattice. The equilibrium position of any atom in the crystal can be described by

$$\mathbf{r}_0(b) = \mathbf{r}_0(0) + \mathbf{r}_0(b), \quad (2.10)$$

where  $\mathbf{r}_0(b)$  is the equilibrium position of the  $b^{\text{th}}$  atom in the unit cell relative to  $\mathbf{r}_0(0)$ . The allowed wavevectors for any crystal structure are defined by

$$\kappa = \sum_{\alpha} \mathbf{b}_{\alpha} \frac{n_{\alpha}}{N_{\alpha}}, \quad (2.11)$$

where  $\mathbf{b}_{\alpha}$  are the reciprocal lattice vectors and  $-N_{\alpha}/2 < n_{\alpha} \leq N_{\alpha}/2$ , where  $n_{\alpha}$  are integers and  $N_{\alpha}$  are now constant even integers. The wavevectors are taken to be in the first Brillouin zone [81].

For the LJ argon and SW silicon systems studied here, the cubic conventional cells are used with four (argon) and eight (silicon) atoms per unit cell. For the MD simulations of LJ argon and

SW silicon, cubic simulation domains are used (i.e.,  $N_1 = N_2 = N_3 = N_0$ ) [17, 66, 68]. For the CNT, the Brillouin zone is one-dimensional, so that  $N_1 = N_2 = 1$ , and we take  $N_3 = 50$  [75].

### 2.3.2 Phonon Lifetimes and Frequencies (WORK)

Once the allowed wavevectors are specified, the atomic velocities from an MD simulation can be used to calculate  $\Phi'$  using Equation (2.8). To calculate  $\Phi$  [Equation (2.1)], (WORK) require the phonon mode eigenvector, which can be obtained using harmonic lattice dynamics calculations and the finite temperature lattice constant (i.e., quasi-harmonic lattice dynamics calculations) [52]. The  $\Phi$  and  $\Phi'$  methods can be used for any material system where there are available interatomic potentials.

The phonon frequencies and lifetimes are found by fitting the spectral curves  $\Phi$  and  $\Phi'$  with Lorentzian functions using a non-linear least squares method. Both of these phonon properties are independent of the Lorentzian peak magnitude. For  $\Phi'$ , the different polarizations at a given wavevector are superimposed by definition of Equation (2.8). The different polarizations can be fit individually using single Lorentzian peaks or as a superposition of peaks. At high temperatures, the broadening of the peaks from different polarizations can make it difficult to uniquely locate the peaks in  $\Phi'$ . Knowledge of the quasi-harmonic frequencies is necessary to identify the unique peaks in  $\Phi'$  as well as degeneracies. [17, 84].

$\Phi$  has the advantage that degenerate and nearly degenerate polarizations can be isolated and fit individually. The uncertainty in the predicted phonon frequencies is on the order of the frequency resolution used to perform the fast Fourier transforms required to evaluate  $\Phi$  and  $\Phi'$ , which is  $10^2 - 10^4$  less than the phonon frequencies studied in this work (see Sections 2.4.1, 2.4.2, and 2.4.3). At the temperatures studied in this work, we find that fitting single or simultaneous peaks in either  $\Phi$  or  $\Phi'$  results in less than five percent difference in the predicted lifetimes. The uncertainty from fitting the Lorentzian functions is between five and ten percent of the predicted

lifetimes, with the error increasing with increasing temperature.<sup>†</sup>

To illustrate the procedure,  $\Phi$  was calculated for LJ argon (Section 2.4.1) with  $N_0 = 10$  and  $T = 20$  K, where  $T$  is temperature.  $\Phi$  for the two modes denoted by A and B [see Fig. A.1(b)] and wavevector  $[\pi/5a, \pi/5a, \pi/5a]$  is shown in Fig. 2.1(b). The lower-frequency peak corresponds to the longitudinal acoustic mode, [52] while the higher frequency peak corresponds to an acoustic mode which has been "zone-folded" (see Section A.3.3). As discussed in Section 2.2.2, the frequency and lifetime extraction in normal mode decomposition can also be performed in the time domain. The autocorrelation of the normal mode kinetic and total energies for the two modes (A and B) are plotted in Fig. 2.1(a). The fits to Eq. (2.6) for the total energy are also plotted and fall on top of the raw data. The inset to Fig. 2.1(a) shows the integration of the total energy according to Eq. (2.7) and the converged values of the lifetimes. The time-domain analysis on the total mode energy has the advantage that only one property needs to be fit – the lifetime. Extracting the frequency from the kinetic energy in the time domain is challenging, however, particularly for short lifetimes, where they will be only a few oscillations in the decay. The frequency is easily extracted from the frequency-domain analysis.

### 2.3.3 Thermal Conductivity

Once the frequencies and lifetimes of all phonon modes in the first Brillouin zone are obtained, the bulk thermal conductivity in direction  $\mathbf{n}$ ,  $k_{\mathbf{n}}$ , can be calculated from [19]

$$k_{\mathbf{n}} = \sum_{\boldsymbol{\kappa}} \sum_{\nu} c_{ph}(\boldsymbol{\kappa}) v_{g,\mathbf{n}}^2(\boldsymbol{\kappa}) \tau(\boldsymbol{\kappa}). \quad (2.12)$$

<sup>†</sup>The range of data must be selected when fitting the Lorentzian functions to  $\Phi$  or  $\Phi'$ . This range should be large enough for the Lorentzian functions to decrease significantly from their value at half-width at half-maximum, where the linewidth is specified, but not too large as to pick up noise. The error in predicting the lifetime is obtained by varying the range of data used to fit the Lorentzian function.

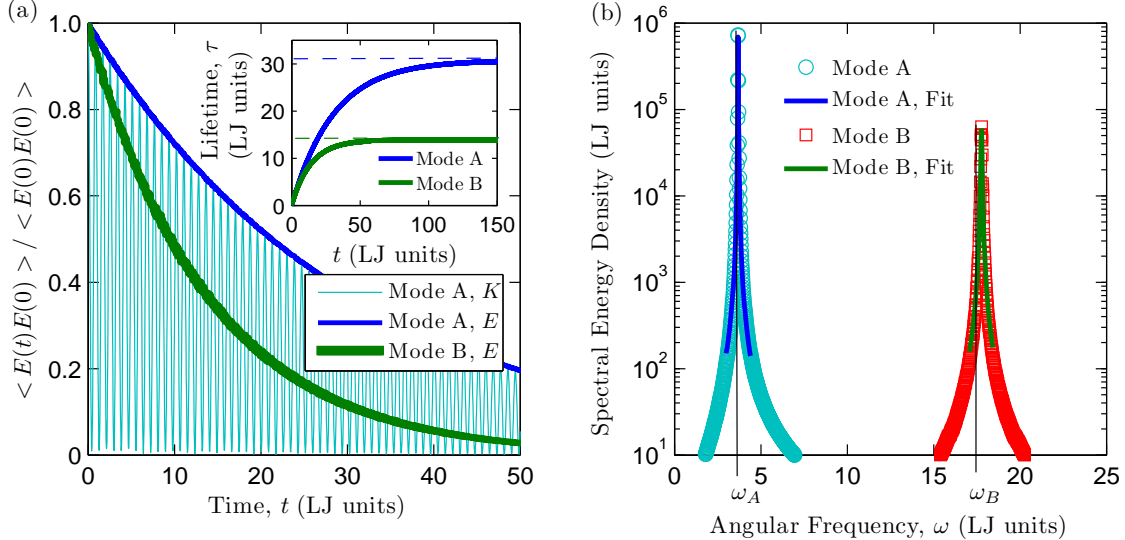


Figure 2.1: Raw data and fits for normal mode decomposition in (a) time-, and (b) frequency-domain analysis for two of the [100] phonon modes from the conventional unit cell for  $N_0 = 10$  [see Fig. A.1(b)] The inset in (a) shows the convergence of the lifetime according to Eq. (??). In (b), the vertical lines denote the frequency predicted from harmonic lattice dynamics calculations.

Here,  $c_{ph}$  is the phonon volumetric specific heat and  $v_{g,n}$  is the component of the group velocity vector in direction  $\mathbf{n}$ . Since the systems we consider are classical and obey Maxwell-Boltzmann statistics [85], the specific heat is  $k_B$  per mode in the harmonic limit, where  $k_B$  is the Boltzmann constant. As temperature increases, anharmonicity causes the mode specific heats to deviate from  $k_B$  [66]. The effect is small for the systems and temperatures studied here. For LJ argon, the mode-averaged specific heat has been predicted to be  $0.95k_B$  per mode at a temperature of 40 K and approaches  $k_B$  with decreasing temperature [66]. For SW silicon at a temperature of 300 K, the predicted mode-averaged specific heat is  $1.01k_B$  per mode [72]. For the CNT at  $T = 300$  K, we predict the mode-averaged specific heat to be  $1.03k_B$  per mode. Because we do not have mode-dependent specific heats, we take the specific heat to be  $k_B$  per mode for the three systems studied (argon, silicon, and CNT). The group velocity vector is the gradient of the dispersion curve (i.e.,  $\partial\omega/\partial\boldsymbol{\kappa}$ ) and can be calculated from the frequencies and wavevectors using finite differences. In this work, the group velocities are calculated using the frequencies from

quasi-harmonic lattice dynamics calculations because a smaller finite difference in wavevector can be used than what is available from the MD simulations (see Section 2.3.1). <sup>‡</sup>

### 2.3.4 Computational Cost and Work Flow Optimization (WORK)

The computational time required to perform normal mode decomposition depends on the number of atoms in the system,  $N_a$ , and the number of atoms in the unit cell,  $b$ . For the eigenvalue problem associated with harmonic lattice dynamics, the time required for each wave vector scales as  $n^3$  and the required memory scales as  $n^2$ . This poor scaling limits the study of systems with more than 10,000 atoms in the unit cell (as might be required for a nanostructure such as a thin films or nanowire), for which the calculations will take one to two days given current computational resources. The harmonic lattice dynamics calculations for different wave vectors are trivially parallelizable and can be performed using the open-source GULP package [86]. For efficiently parallel MD algorithms (e.g., the open-source LAMMPS package [87]), the simulation time and required memory scale as  $\sim N$ .

The computational time and memory required to project the atomic velocities and positions onto the normal mode coordinates scale as  $N$  and these calculations are trivially parallelizable over the normal modes. Reasonable computational times can be realized by using LAMMPS to perform the MD simulations, outputting the atomic trajectories, and writing programs to perform the normal mode decomposition using a scripting language like Python with the NumPy module [88]. Because normal mode decomposition is trivially parallelizable on multi-core architectures over the normal modes, massively parallel calculations can be achieved by using a PBS scheduler such as TORQUE. Ideally, however, to reduce memory requirements, the projection of the atomic positions and velocities onto the normal mode coordinates and calculations of the normal mode

<sup>‡</sup>The anharmonic frequency shift affects the group velocity. McGaughey and Kaviany find that anharmonic and quasi-harmonic predictions of the group velocity differ for LJ Argon by less than one percent at a temperature of 50 K and that the difference decreases with decreasing temperature [66]. The anharmonic frequency shifts are on average a few percent for LJ argon at a temperature of 40 K and are less for the other temperatures and systems studied here.

potential and kinetic energies would be directly built into the MD code. The energies would then be periodically output to perform the required autocorrelations and/or Fourier transforms.

In normal mode decomposition, the sampling rate must be high enough to capture the maximum frequency in the system. The sampling rate and total run time should be chosen in powers of two as a convenience in performing fast Fourier transforms. Obtaining the phonon properties from Eqs. (??), (??), (??), and (??) requires specification of a time or frequency range and initial guesses for the frequency and lifetime. These parameters can be obtained from observation of the raw data. An initial guess for the frequency can also be obtained from the harmonic lattice dynamics calculations. When investigating new systems, it is best to fit the phonon properties in a semi-automated way (i.e., each fit should be visualized so that the fitting parameters can be tuned). Once appropriate fitting parameters are chosen, the fitting can usually be fully automated for large data sets. For crystalline systems, only the properties of the modes of the irreducible wave vectors are needed, such that the autocorrelations or Fourier transforms for symmetric modes can be averaged before fitting. See Appendix A.3.2 for a discussion of symmetries.

For the  $\Phi$  and  $\Phi'$  methods, the computational cost of evaluating Equation (2.8) is less than that for Equation (2.1) by a factor of  $3b$ . For bulk crystals, the number of atoms in the unit cell is typically small ( $b < 10$ ). For the (8,8) CNT system,  $b = 32$  and evaluating  $\Phi'$  is two orders of magnitude less expensive than evaluating  $\Phi$ .

To calculate the phonon lifetimes, the MD simulation time should be an order of magnitude longer than the longest phonon lifetime [89]. If only the phonon frequencies are required, however, the location of the peaks in  $\Phi$  and  $\Phi'$  develop in a time on the order of the inverse of the phonon frequency,  $1/\omega_0(\kappa_\nu)$ . For the systems studied here, this time can be two to five orders of magnitude less than the time needed to develop the lifetimes.

Fitting  $\Phi'$  becomes challenging at higher temperatures, when the phonon linewidths broaden and become comparable to the spacing between mode frequencies. The cost of fitting  $\Phi'$  can be reduced by fitting the peaks from all allowed wavevectors in the system simultaneously, but the error associated with this procedure is unknown [78]. We find that a semi-automated procedure,

whereby the fits are visualized, is necessary to ensure that all peaks are fit correctly. While the computational cost of fitting  $\Phi'$  is much smaller than the computational cost of calculating  $\Phi'$ , the semi-automated fitting procedure can be of similar time cost to the user. The cost of fitting  $\Phi$  is much smaller because the different polarization peaks can be isolated and the fitting can be fully automated.

## 2.4 Case Studies

### 2.4.1 Lennard-Jones Argon

We now use MD simulation to compare the SED, phonon properties, and thermal conductivity calculated for LJ argon using  $\Phi$  and  $\Phi'$ . The MD simulations are performed using LAMMPS.[87] A truncated and shifted potential cutoff scheme is used with a cutoff radius of 8.5 Å. The quasi-harmonic phonon frequencies, eigenvectors, and group velocities are generated using GULP [86]. We consider temperatures of 5, 20, and 40 K at zero-pressure with lattice constants of 5.278, 5.315, and 5.371 Å. For LJ argon, Turney et al. found that lattice dynamics-based predictions of thermal conductivity (e.g., by anharmonic lattice dynamics or  $\Phi$ ) start to diverge from MD-based predictions (e.g., from the direct or Green-Kubo methods) above half the melting temperature ( $T_{\text{melt}} \approx 80$  K) [17]. Here, we limit the temperature to below half the melting temperature for the three systems studied (argon, silicon, and CNT).

The MD system consists of  $N_1 \times N_2 \times N_3 = 8^3 = 512$  conventional cubic unit cells for a total of 2048 atoms ( $b = 4$  atoms). Using a 4.285 fs time step, the system is equilibrated for  $2^{20}$  time steps before collecting data every  $2^5$  time steps for an additional  $2^{20}$  time steps in the  $NVE$  ensemble (constant number of atoms, system volume, and total system energy) [85]. The sampling rate must be high enough to capture the highest phonon frequency in the system. The sampling rate and total run time are chosen in powers of two as a convenience in performing the fast Fourier transforms required to efficiently evaluate  $\Phi$  and  $\Phi'$ . The same MD simulation data

are used to calculate  $\Phi$  and  $\Phi'$ . Five simulations with different initial conditions are performed and the  $\Phi$  and  $\Phi'$  values are averaged before the peak fitting.  $\Phi$  and  $\Phi'$  are further averaged over degenerate wavevectors in the Brillouin zone, reducing the wavevectors to the first octant [28].

The SED ( $\Phi$  and  $\Phi'$ ) for the wavevector  $[\pi/2a, 0, 0]$  is presented in Fig. 2.2 for all three temperatures (the edge of the Brillouin zone is at  $[\pi/a, 0, 0]$ ). For  $\Phi$ , the spectral curve is plotted as a superposition over the twelve phonon polarizations, with degeneracy reducing the number of peaks to seven. Overall,  $\Phi'$  does not equal the total phonon spectral energy density  $\Phi$ , but the major features are similar. At all temperatures there are linewidth variations between the two spectral curves. The peak magnitudes become comparable for  $\Phi$  and  $\Phi'$  as the temperature increases.

The phonon frequencies and lifetimes extracted for all allowed wavevectors in the first Brillouin zone using  $\Phi$  and  $\Phi'$  at each of the three temperatures are compared on a mode-by-mode basis in Figs. 2.3(a), 2.3(b), and 2.3(c). There,  $\omega_0$ ,  $\omega'_0$ ,  $\tau$ , and  $\tau'$  refer to the mode properties predicted using  $\Phi$  and  $\Phi'$ . The phonon frequencies agree well at all three temperatures, with increasing scatter at high temperatures and high frequencies. This scatter is due to the high-frequency peak broadening seen in Fig. 2.2 at  $T = 40$  K, which can force peaks close in frequency for  $\Phi'$  to be fit as a single Lorentzian function. The frequencies predicted by  $\Phi$  and  $\Phi'$  include the effects of anharmonicity, which increase the frequencies compared to the quasi-harmonic predictions [17, 84]. The agreement between the frequencies predicted from  $\Phi$  and  $\Phi'$  is explained in (REF) (WORK).

The lifetimes show large scatter between  $\Phi$  and  $\Phi'$  on a mode-by-mode basis, with increasing scatter at high temperature that shows no systematic difference. The scatter at high frequencies is in part due to the peak broadening seen in Fig. 2.2, which can force peaks close in frequency for  $\Phi'$  to be fit as a single Lorentzian function with a single lifetime. The broadening does not affect fitting at low frequencies, where the linewidths are much smaller than the peak spacings. There, any scatter comes solely from the difference between  $\Phi$  and  $\Phi'$ .

The phonon properties are then used to predict thermal conductivity using Equation (2.12).

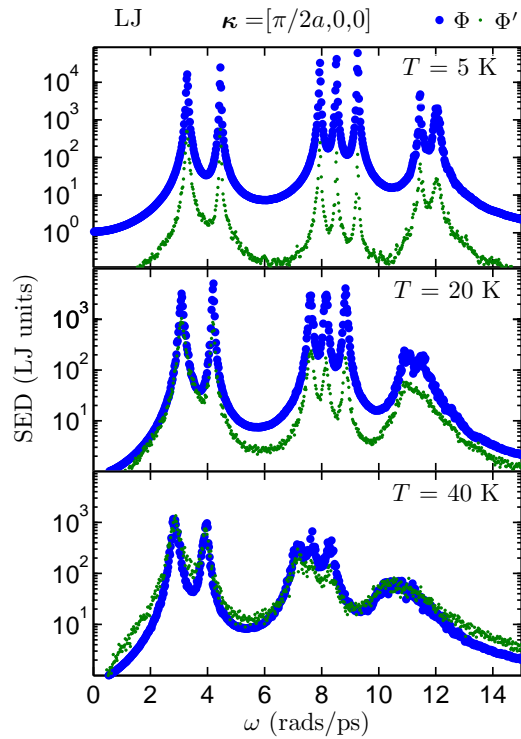


Figure 2.2: The phonon spectral energy density ( $\Phi$ ) is plotted as larger blue circles. The proposed alternative expression for the phonon spectral energy density ( $\Phi'$ ) is plotted as smaller green points. The wavevector is  $(\pi/2a, 0, 0)$ . Note that peak broadening at higher temperatures and frequencies above 10 rads/ps can force peaks close in frequency for  $\Phi'$  to be fit as a single Lorentzian function.  $\Phi$  does not suffer from this issue since the broadened peaks can be fit individually.

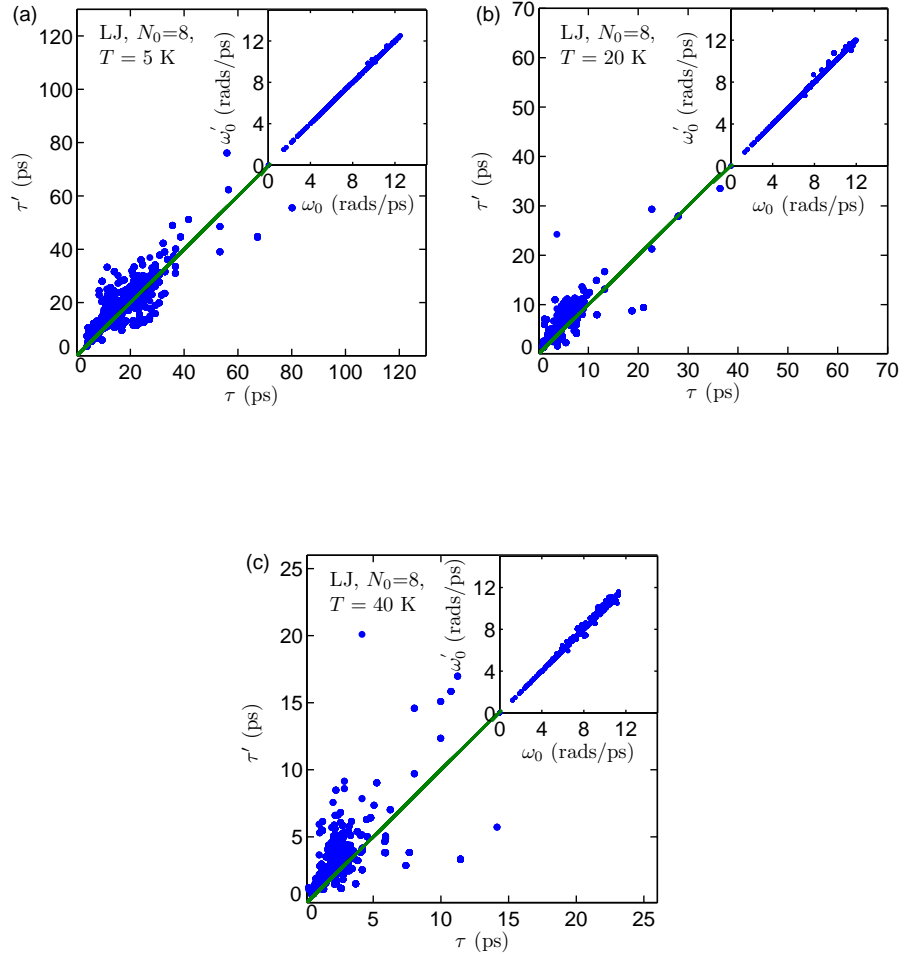


Figure 2.3: Comparison of the phonon frequencies and lifetimes predicted using  $\Phi$  ( $\omega$  and  $\tau$ ) and  $\Phi'$  ( $\omega'$  and  $\tau'$ ) for LJ argon at temperatures of (a) 5 K, (b) 20 K, and (c) 40 K. The phonon frequencies agree well at all three temperatures, while the phonon lifetimes show large scatter.

The results are presented in Table 3.1. The bulk thermal conductivities provided in Table 3.1 are predicted using the finite simulation-size scaling procedure discussed in [17]. The bulk thermal conductivities predicted from  $\Phi'$  are smaller and outside the uncertainty for those predicted from  $\Phi$  for temperatures of 5 and 20 K. While the bulk thermal conductivities at a temperature of 40 K agree within their uncertainties, the predicted mode-by-mode lifetimes show large scatter [Fig. 2.3(c)] and the agreement should be regarded as coincidental.

The disagreement between  $\Phi$  and  $\Phi'$  in thermal conductivity comes directly from the differences in the phonon lifetimes. All other properties (frequencies, group velocities, specific heats) are nearly or exactly the same for the two calculations. The bulk thermal conductivities predicted from  $\Phi$  and  $\Phi'$  are also compared to predictions from the Green-Kubo method[85] in Table 3.1. For  $N_1 = N_2 = N_3 = 8$ , the thermal conductivity predicted by the Green-Kubo method is converged with respect to the simulation size [66]. The same MD data used to calculate  $\Phi$  and  $\Phi'$  is used for the Green-Kubo predictions. For all three temperatures, there is good agreement between the thermal conductivity predictions using  $\Phi$  and Green-Kubo. For temperatures of 20 and 40 K, there is good agreement between the predictions from  $\Phi$ , Green-Kubo, and previous reports using non-equilibrium MD, anharmonic lattice dynamics, and time-domain  $\Phi$  [17].

#### 2.4.2 Stillinger-Weber Silicon

We next compare the phonon properties and thermal conductivity predicted from  $\Phi$  and  $\Phi'$  for SW silicon [6] at a temperature of 300 K and zero pressure with a lattice constant of 5.437 Å. The SW system is stiffer (larger phonon group velocities, frequencies, and lifetimes) than LJ argon and is an additional test to determine if there is a systematic error in the predictions from  $\Phi'$ . The MD simulations are performed using LAMMPS [87]. The MD system consists of  $N_1 \times N_2 \times N_3 = 6^3 = 216$  conventional unit cells for a total of 1728 atoms ( $b = 8$  atoms). The phonon frequencies, eigenvectors, and group velocities are generated using GULP [86].

Table 2.1: Thermal conductivity values in W/m-K predicted using the  $\Phi$ ,  $\Phi'$ , and Green-Kubo methods. The predictions for  $\Phi$  and Green-Kubo for the LJ system are in good agreement with those from other atomistic simulation methods [17] while those from  $\Phi'$  differ and show no consistent behavior. The uncertainties in the predicted thermal conductivities for  $\Phi$  and  $\Phi'$  come predominantly from the finite simulation-size scaling procedure (see Ref. [17, 18]), where the phonon properties and thermal conductivity are predicted for increasing system sizes ( $N_1 = N_2 = N_3$ ) to extrapolate a bulk thermal conductivity. For SW silicon and the CNT, the extrapolation procedure is not performed.

$T$ (K)	Green-Kubo	$\Phi$	$\Phi'$
LJ (bulk)			
5	$8.0 \pm 0.30$	$7.9 \pm 0.42$	$5.8 \pm 0.31$
20	$1.3 \pm 0.15$	$1.2 \pm 0.07$	$1.0 \pm 0.10$
40	$0.45 \pm 0.07$	$0.47 \pm 0.03$	$0.49 \pm 0.05$
SW ( $N_1 = N_2 = N_3 = 6$ )			
300		$322 \pm 16$	$396 \pm 38$
CNT ( $N_1 = N_2 = 1, N_3 = 50$ )			
300		$428 \pm 21$	$398 \pm 40$

Using a 0.5 fs timestep, the system is equilibrated for  $2^{20}$  time steps before collecting data every  $2^5$  time step for  $2^{22}$  time steps in the  $NVE$  ensemble [85]. As with the LJ system, the sampling rate is determined by the highest phonon frequency in the system. Five simulations with different initial conditions are performed and the  $\Phi$  and  $\Phi'$  values are averaged before the peak fitting.  $\Phi$  and  $\Phi'$  are further averaged over degenerate wavevectors in the Brillouin zone, reducing the wavevectors to the first octant [28].

The extracted phonon frequencies and lifetimes are plotted in Fig. 2.4. As with the LJ system, the phonon frequencies are predicted accurately by  $\Phi'$  but the lifetimes show large scatter on a mode-by-mode basis. For the system size studied,  $\Phi'$  predicts a larger thermal conductivity than  $\Phi$  outside the prediction uncertainties, in contrast to the LJ system (see Table 3.1). The disagreement in thermal conductivity comes directly from the phonon lifetimes.

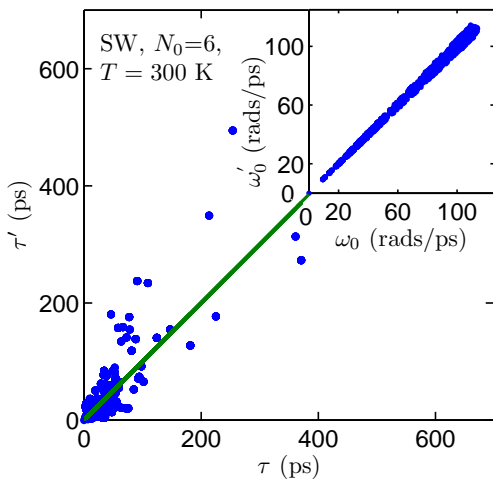


Figure 2.4: Comparison of the phonon frequencies and lifetimes predicted using  $\Phi(\omega$  and  $\tau)$  and  $\Phi'(\omega'$  and  $\tau')$  for SW silicon. The phonon frequencies agree well, while the phonon lifetimes show large scatter.

### 2.4.3 Carbon Nanotube

Finally, we compare the phonon properties and thermal conductivities predicted by  $\Phi$  and  $\Phi'$  for an (8,8) CNT (diameter of 1.10-nm and length of 12.3 nm) at a temperature of 300 K and zero pressure [75]. The interactions in the CNT system are modeled using the REBO potential without the four-body interaction term [82]. The MD simulations are performed using an in-house code. The MD system consists of 1600 atoms (32 atoms/unit cell). The phonon frequencies, eigenvectors, and group velocities are generated using an in-house code. The purpose of simulating this system is to check the results of Thomas et al. [75] (who used  $\Phi'$  and non-equilibrium MD), and to compare the predictions of  $\Phi'$  and  $\Phi$ .

Using a 1.0 fs timestep, the system is equilibrated for  $2^{20}$  time steps before collecting data every  $2^3$  time step for  $2^{22}$  time steps in the  $NVE$  ensemble [85]. As with the LJ and SW systems, the sampling rate is determined by the highest phonon frequency in the system. Five simulations with different initial conditions are performed and the  $\Phi$  and  $\Phi'$  values are averaged before the peak fitting. Since the Brillouin zone of the CNT is one-dimensional,  $\Phi$  and  $\Phi'$  are further averaged over directionally-degenerate wavevectors.

The phonon frequencies and lifetimes for the allowed wavevectors in the one-dimensional Brillouin zone are shown in Fig. 2.5. Like the LJ and SW silicon systems, the phonon frequencies can be predicted accurately by  $\Phi'$ , but the lifetimes show large scatter. The estimated thermal conductivity of the CNT predicted using  $\Phi'$  is in agreement with the results of Thomas et al. [75]. The thermal conductivity predicted by  $\Phi'$  is less than that predicted by  $\Phi$ , but not outside their uncertainties.

## 2.5 Summary

We presented the correct phonon SED,  $\Phi$ , and its relation to the phonon frequencies and lifetimes. We then presented an alternative formulation to the phonon spectral energy density,  $\Phi'$ ,

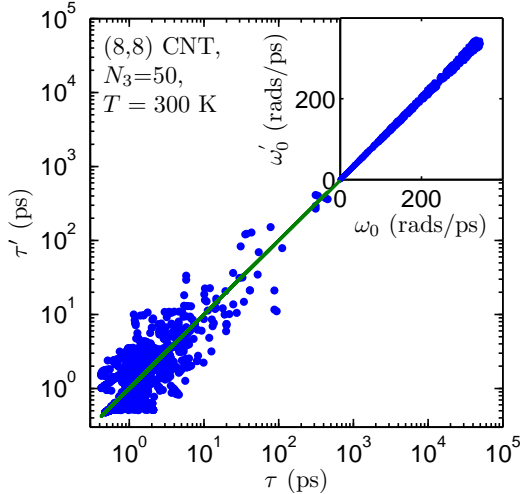


Figure 2.5: Comparison of the phonon frequencies and lifetimes predicted using  $\Phi(\omega, \tau)$  and  $\Phi'(\omega', \tau')$  for a (8,8) CNT modeled using the REBO potential. The phonon frequencies agree well, while the phonon lifetimes show large scatter.

which does not require the phonon mode eigenvectors. Because  $\Phi'$  does not contain the eigenvectors, this alternative formulation does not represent the phonon spectral energy density, but does contain information about the phonon dispersion as the temperature approaches 0 K (see Appendix A.2).

We then calculated the phonon SED for LJ argon, SW silicon, and a CNT modeled with the REBO potential using  $\Phi$  and  $\Phi'$ . The phonon frequencies and lifetimes predicted from  $\Phi$  and  $\Phi'$  are shown in Figs. 2.3, 2.4 and 2.5. The frequencies are in good agreement between the two SED methods, while the lifetimes show large scatter.

The phonon SED  $\Phi$  is well-defined theoretically, while  $\Phi'$  does not properly map to the phonon energies since it is missing the phonon mode eigenvector. We deduce that this is the reason  $\Phi'$  does not accurately predict the phonon lifetimes. It is surprising how close the predicted thermal conductivities can be using  $\Phi$  and  $\Phi'$  (LJ at  $T = 40$  K and the CNT results). The thermal conductivities predicted by  $\Phi$  and  $\Phi'$ , however, show no consistency for the three systems studied.

The most important predictions are the mode-by-mode phonon properties. Of particular im-

portance are the lifetimes, which are the key input for Boltzmann transport equation-based models [60]. Thus, we do not recommend  $\Phi'$  for predicting phonon lifetimes or thermal conductivity. Any agreement in thermal conductivity predictions between atomistic studies[75] and experiment [77, 79] should be regarded as coincidental, and the phonon lifetime reductions predicted for systems with additional scattering methods [75, 78] should only be interpreted qualitatively. The use of  $\Phi'$  in future work is discouraged and we reccomend the use of  $\Phi$ .

# Chapter 3

## Predicting alloy vibrational mode properties using lattice dynamics calculations, molecular dynamics simulations, and the virtualcrystal approximation

The virtual crystal (VC) approximation for mass disorder is evaluated by examining two model alloy systems: Lennard-Jones argon and Stillinger-Weber silicon. In both material systems, the perfect crystal is alloyed with a heavier mass species up to equal concentration. The analysis is performed using molecular dynamics simulations and lattice dynamics calculations. Mode frequencies and lifetimes are first calculated by treating the disorder explicitly and under the VC approximation, with differences found in the high-concentration alloys at high frequencies. Notably, the lifetimes of high-frequency modes are underpredicted using the VC approximation, a result we attribute to the neglect of higher-order terms in the model used to include point-defect scattering. The mode properties are then used to predict thermal conductivity under the VC ap-

proximation. For the Lennard-Jones alloys, where high-frequency modes make a significant contribution to thermal conductivity, the high-frequency lifetime underprediction leads to an underprediction of thermal conductivity compared to predictions from the Green-Kubo method, where no assumptions about the thermal transport are required. Based on observations of a minimum mode diffusivity, we propose a correction that brings the VC approximation thermal conductivities into better agreement with the Green-Kubo values. For the Stillinger-Weber alloys, where the thermal conductivity is dominated by low-frequency modes, the high-frequency lifetime underprediction does not affect the thermal conductivity prediction and reasonable agreement is found with the Green-Kubo values.

### 3.1 Introduction

Due to their potentially low thermal conductivities, disordered materials (e.g., alloys, amorphous solids, aerogels) are used in applications ranging from thermoelectric energy conversion to thermally insulating barriers. [40, 90, 91, 92, 93, 94, 95, 96, 97, 98] Disordered lattices are a subgroup of disordered materials where the atomic positions follow a lattice structure but the constituent species are spatially random. Examples include isotopic solids, where the species have the same electronic structure but small mass variations,[24, 33] and alloys, our focus here, where at least two distinct species are present.[37, 99]

We further restrict our focus to dielectric or semiconducting solids, where the heat is conducted by the atomic vibrational modes. Predicting the thermal conductivity of such materials requires the properties of the full spectrum of vibrational modes. [19, 45, 100] Accurate predictions of these properties for crystalline systems (i.e., perfect lattices) can be made with anharmonic lattice dynamics (ALD) theory using input from density functional theory (DFT) calculations.[20, 21, 22, 24, 25, 26, 35, 36, 41, 78] Computational costs limit DFT calculations to less than 100 atoms, however, making it challenging to explicitly incorporate the effects of disorder. [22, 23, 24, 26, 35, 101, 102]

Disorder is typically included in the ALD framework using Abeles' virtual crystal (VC) approximation, whereby the disordered solid is replaced with a perfect VC with properties equivalent to an averaging over the disorder (e.g., atomic mass, bond strength).[37] The ALD calculations are performed on a small unit cell with the averaged properties (i.e., all vibrational modes are phonons) and phonon-phonon and phonon-disorder scattering are included as perturbations. [22, 24, 26, 33, 37] Except for low-frequency (long-wavelength) acoustic modes, the general validity of this assumption is unclear. We will refer to this approach as VC-ALD. Recent work using DFT calculations and the VC-ALD approach has modeled disordered lattices with relatively large ( $\sim 10\text{-}100 \text{ W/m-K}$ ) [22, 24, 35] and small ( $\sim 1 \text{ W/m-K}$ )[26] thermal conductivities. No comprehensive study has been performed to assess the applicability of the VC-ALD approach for a range of disorder strength.

The objective of this study is to investigate the use of the VC approximation for predicting the vibrational mode properties and thermal conductivity of alloys by a detailed comparison of three predictive methods: (i) molecular dynamics (MD)-based normal mode decomposition (NMD), (ii) MD-based Green-Kubo (GK), and (iii) VC-ALD. By using computationally-inexpensive empirical potentials for argon [Lennard-Jones (LJ) at a temperature of 10 K] [81] and silicon [Stillinger-Weber (SW) at a temperature of 300 K], [6] we can self-consistently study the effects of disorder both explicitly and as a perturbation. For both materials, the perfect lattice is disordered with a heavier mass species up to equal concentration, spanning a range of small to large disorder. By spanning this range, the limits of the perturbative models are examined.

The remainder of the paper is organized as follows. In Section 3.2, the theoretical formulation of thermal transport in ordered and disordered solids and the computational framework are described. In Section 4.4, the frequencies, group velocities, lifetimes, and diffusivities of the vibrational modes of the LJ argon alloys are predicted when the disorder is explicitly modeled and when it is treated as a perturbation in the VC approximation. A breakdown of the VC-ALD method is identified by a comparison with the VC-NMD method in Section 3.3.3.2 and a correction is suggested in Section 4.4.5. The vibrational mode properties are then used to predict

thermal conductivities in Section 3.4, allowing for a comparison to the predictions of the top-down GK method, where no assumptions about the nature of the thermal transport are required. The vibrational mode properties and thermal conductivity of the SW silicon alloys, where low-frequency modes dominate the thermal conductivity, are predicted in Section 3.5 to provide a comparison and contrast to the LJ argon alloys.

## 3.2 Theoretical and Computational Framework

### 3.2.1 Thermal Conductivity Prediction

To predict the thermal conductivity of a disordered lattice, one begins with the theory for a perfect lattice. For a perfect lattice, all vibrational modes are phonon modes, which by definition are delocalized, propagating plane waves. [19] Using the single-mode relaxation time approximation [19] to solve the Boltzmann transport equation gives an expression for thermal conductivity in direction  $\mathbf{n}$ ,

$$k_{ph,\mathbf{n}} = \sum_{\boldsymbol{\kappa}} \sum_{\nu} c_{ph}(\boldsymbol{\kappa}_{\nu}) v_{g,\mathbf{n}}^2(\boldsymbol{\kappa}_{\nu}) \tau(\boldsymbol{\kappa}_{\nu}). \quad (3.1)$$

Here, the sum is over the phonon modes in the first Brillouin zone,  $\boldsymbol{\kappa}$  is the wave vector, and  $\nu$  labels the polarization branch. The phonon mode has frequency  $\omega(\boldsymbol{\kappa}_{\nu})$ , volumetric specific heat  $c_{ph}(\boldsymbol{\kappa}_{\nu})$ ,  $\mathbf{n}$ -component of the group velocity vector  $v_{g,\mathbf{n}}(\boldsymbol{\kappa}_{\nu})$ , and lifetime  $\tau(\boldsymbol{\kappa}_{\nu})$ .

The relaxation time approximation has been found to be valid for lower thermal conductivity materials (e.g., Si and SiGe alloys), [20, 21, 22] while larger thermal conductivity materials such as GaN and diamond require an iterative solution to the BTE for more accurate predictions using Eq. (3.1). [23, 24] For the crystalline LJ argon and SW silicon phases, the lattices and the components of their thermal conductivity tensors are cubically symmetric, so that we will refer to  $k_{ph}$  as an isotropic scalar thermal conductivity. This isotropy will hold for disordered lat-

tices in the infinite-size limit. Since MD simulations are classical and obey Maxwell-Boltzmann statistics,[85] the volumetric specific heat is  $k_B/V$  per mode in the harmonic limit, where  $V$  is the system volume and  $k_B$  is the Boltzmann constant. This harmonic approximation for specific heat has been shown to be valid for LJ argon and SW silicon at the temperatures of interest here [66, 72] and is used so that direct comparisons can be made between the MD- and lattice dynamics-based methods.

For disordered systems, the vibrational modes are no longer pure plane-waves (i.e., phonon modes), except in the low-frequency (long-wavelength) limit. When applied in the classical limit, the Allen-Feldman (AF) theory computes the contribution of diffusive, non-propagating modes (i.e., diffusons) to thermal conductivity from[44]

$$k_{AF} = \sum_{\text{diffusons}} \frac{k_B}{V} D_{AF,i}(\omega_i), \quad (3.2)$$

where  $D_{AF,i}$  is the mode diffusivity and  $\omega_i$  is the frequency of the  $i$ th diffuson. The diffusivity of diffusons can be calculated from harmonic lattice dynamics theory. [44, 45, 46]

Assuming that all vibrational modes travel with the sound speed,  $v_s$ , and scatter over a distance of the lattice constant,  $a$ , a high-scatter (HS) limit of thermal conductivity in the classical limit is[40]

$$k_{HS} = \frac{k_B}{V_b} b v_s a, \quad (3.3)$$

where  $V_b$  is the volume of the unit cell and  $b$  is the number of atoms in the unit cell. The HS limit will be used to discuss the differences between the LJ argon and SW silicon alloys.

### 3.2.2 Virtual Crystal Approximation

Under the VC approximation, the disordered solid is replaced with a perfect, single-species crystal with properties (e.g., density, cohesive energy) equivalent to an averaging over the disorder (e.g., atomic mass, bond strength).[37] The VC approximation is visualized for an alloy in Figs.

3.2(a) and 3.2(b), where a mass-disordered supercell is replaced by a perfect crystal with an averaged mass. Abeles first introduced the concept of a VC to predict the thermal conductivity of SiGe, GaAs/InAs, and InAs/InP alloys. [37] Klemens-Callaway theory, which is valid for low-frequency modes and small disorder, was used to model the phonon-phonon and phonon-defect scattering. [30, 31, 32, 34, 37, 63] The Abeles theory is conceptually simple, treating both disorder and anharmonicity as perturbations, and leads to a closed-form analytical function for the thermal conductivity. With the use of phenomenological fitting parameters, good agreement between the predictions and experimental measurements was found for SiGe and GaAs/InAs alloys. Deviations were observed for InAs/InP alloys at large concentrations of InP, which were attributed to the large mass ratio of 3.7 between indium and phosphorus.[37]

When considering alloys, it is important to note that the overall disorder strength is determined by the mass ratio, the stiffness ratio, and the alloy concentration. Cahill and co-workers found that as little as  $6.2 \times 10^{19} \text{ cm}^{-3}$  germanium reduces the thermal conductivity of epitaxial silicon layers by a factor of two. [38] Using the Abeles theory, they explained this result by mass perturbative disorder alone (the Ge/Si mass ratio is 2.6). [38, 39] The relative effects of bond and mass disorder were investigated computationally using MD simulations by Skye and Schelling for SiGe alloys up to equal concentration. [103] They also found that mass disorder is the dominant scattering mechanism. Subsequent studies have modeled the effect of differing species by only including atomic mass differences.[62, 104]

Unlike the phenomenological Abeles theory, the VC-ALD approach predicts thermal conductivity by directly summing over the modes of the full vibrational spectrum, with phonon-phonon and phonon-defect scattering treated as perturbations. [22, 24, 26] In the VC-ALD method, the phonon-phonon scattering is predicted using ALD.[17, 25] The phonon-defect scattering is treated using perturbative methods that can handle mass and/or bond disorder. [30, 31, 32, 33] In  $\text{Ni}_{0.55}\text{Pd}_{0.45}$ , which has a large mass ratio (1.8) and concentration of each species, experimental measurements of vibrational frequencies and linewidths agree well with predictions from the perturbative mass-disorder theory. [32, 33, 34]

Using DFT methods to predict the mode-specific phonon properties of the VC, Lindsay and Broido found good agreement between VC-ALD and experimental measurements of thermal conductivity for isotopically defected GaN (the gallium isotopes have concentrations of 0.6 and 0.4 and a mass ratio of 1.03).[24] Garg et al. used DFT calculations with VC-ALD to predict the thermal conductivity of SiGe alloys for all concentrations at a temperature of 300 K, obtaining good agreement with experiment.[22] By including disorder explicitly in their ALD calculations, the predicted thermal conductivity decreased by 15%. Isotopically-defected GaN and low concentration SiGe alloys have relatively large thermal conductivities at a temperature of 300 K ( $\sim$  100 W/m-K). Li et al. used DFT calculations with VC-ALD to predict the thermal conductivity of  $Mg_2Si_xSn_{1-x}$  ( $\sim$  10 W/m-K) in good agreement with experimental measurements for all concentrations.[35] The VC-ALD approach has also been used to predict the effect of interfacial mixing in GaAs/AlAs superlattices, but the thermal conductivity predictions were not compared with experimental measurements.[36] In our survey of experimental measurements and numerical modeling, we find that VC predictions tend to be accurate when the disordered lattice thermal conductivity is significantly above the high-scatter limit [Eq. (3.3)], which tends to be around 1 W/m-K. [22, 24, 34, 37, 38, 39, 40]

An ALD study using phonon properties from DFT calculations for crystalline PbTe[41] predicted thermal conductivities of 2 W/m-K at a temperature of 300 K in fair agreement with experiment. For PbTeSe alloys, a VC-ALD study predicted a small thermal conductivity reduction compared to the perfect crystals.[26] Experimental results are limited for these alloys,[42, 43] making it difficult to assess the validity of the VC-ALD approach for materials whose thermal conductivities approach the high-scatter limit.

Given all these results, it is unclear what limitations exist for using the VC approach. In this study, we will consider a low thermal conductivity alloy using the LJ potential and a high thermal conductivity alloy using the SW potential. The computational studies discussed above were limited to VC-ALD because of DFT calculation costs. Our use of computationally inexpensive empirical potentials allows us to include the disorder explicitly and as a perturbation and to

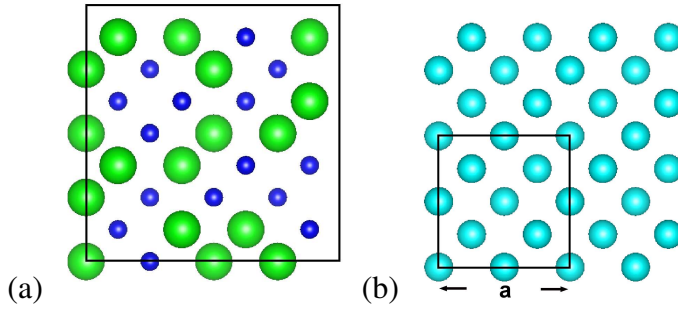


Figure 3.1: (a) Explicitly disordered supercell of Si and “heavy” Si ([100] direction into the paper). [1] (b) Equivalent VC supercell with one averaged mass. The sphere size represents increasing mass only, no bond disorder is considered. The 8-atom conventional cubic unit cell is shown in (b).

compare the predictions.

### 3.2.3 Calculation and Simulation Details

The key to explicitly incorporating the effects of disorder is to use large disordered supercells. Perfect and disordered lattice supercells are generated using the conventional unit cells for LJ argon ( $n = 4$ ) and SW silicon ( $n = 8$ ), where  $n$  is the number of atoms in the unit cell. Supercells are built cubically with size  $N_0$ , where  $N_0$  is the number of unit cell repetitions in the three spatial directions. Supercells up to  $N_0 = 12$  (6,096 atoms) are used for the LJ argon calculations. For SW silicon,  $N_0 = 8$  (4,096 atoms) is used for the MD-based NMD calculations and  $N_0 \leq 42$  (592,704 atoms) is used for the MD-based GK and VC-ALD.

Disorder is created by randomly specifying the masses of the atoms on the lattice. The composition of each lattice is labeled by  $m_{1-c}^i m_c^j$ , where (i)  $m^i = 1$  and  $m^j = 3$  in LJ units for argon, and (ii)  $m^i = m_{Si}$  and  $m^j = 2.6m_{Si}$  for SW silicon and “heavy silicon”, which has the mass of germanium. Concentrations,  $c$ , of 0, 0.05, 0.15 and 0.5 are considered.

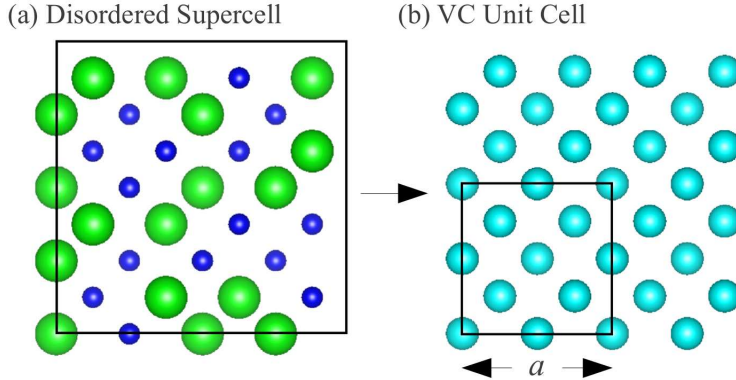


Figure 3.2: (a) Explicitly disordered alloy supercell of silicon and “heavy” silicon ([100] direction into the page). [1] (b) Equivalent VC supercell with one averaged mass. The sphere size represents increasing mass only, no bond disorder is considered. The 8-atom conventional cubic unit cell is shown in (b).

For LJ argon, the lattice constant at a temperature of 10 K is 5.290 Å.[28] The MD simulations were performed using LAMMPS.[87] Efficient MD codes like LAMMPS scale linearly with the number of atoms in the system,  $N_a$ , which makes the GK method (see Section 3.4) computationally-inexpensive when used with empirical potentials. An amorphous LJ phase, discussed in Section 4.4.5, was created by liquefying the crystal and instantly quenching by removing all kinetic energy. The energy of the resulting structure was minimized and then annealed in an  $NPT$  (constant number of atoms  $N$ , pressure  $P$ , and temperature  $T$ ) ensemble at zero pressure and a temperature of 10 K. The effective zero-pressure lattice constant of the amorphous phase at this temperature, based on the atomic density, is 5.389 Å. For SW silicon, we use a lattice constant of 5.43 Å for all calculations, which brings the perfect crystal GK thermal conductivity predictions at a temperature of 300 K [72, 105] into better agreement with ALD predictions[106] compared to using the zero-pressure lattice constant.

All MD simulations are first equilibrated in a  $NVT$  (constant number of atoms, volume, and temperature) ensemble for  $10^6$  time steps. Data is then collected from simulations in the  $NVE$  (constant number of atoms, volume, and total energy) ensemble. For LJ argon, the potential energy is cutoff and shifted at 8.5 Å (the force is not adjusted). Time steps of 4.285 and 0.5 fs

were used for the LJ argon and SW silicon simulations. The same atomic trajectories are used for the NMD and GK methods.

## 3.3 Vibrational Mode Properties in Alloys

### 3.3.1 Density of States

In this section, we begin to examine the effects of explicitly including disorder by computing the frequencies and density of states (DOS) for the vibrational modes of disordered LJ lattice supercells and their equivalent VCs. The frequencies are computed using harmonic lattice dynamics calculations with GULP.[86] For the VC, the allowed wave vectors are set by  $N_0$  and, due to the use of the conventional unit cell, there are 12 polarization branches per wave vector. For the disordered supercells (referred to herein as Gamma), the only allowed wave vector is the gamma-point (i.e.,  $\kappa = 0$ ), where there are  $12N_0^3$  polarization branches. Calculation of the Gamma modes require the eigenvalue solution of a dynamical matrix of size  $(3N_a)^2$  that scales as  $[(3N_a)^2]^3$ , limiting the system sizes that can be considered. This eigenvalue solution is also required to perform the Gamma-NMD (see Section 3.3.3.1) and AF calculations (see Section 4.4.5).

The DOS for the VC and Gamma modes are plotted in Figs. 3.3(a), 3.3(b), and 3.3(c) for concentrations of 0.05, 0.15, and 0.5 for  $N_0 = 12$  (6,912 atoms). The VC and Gamma DOS agree at low frequencies for all concentrations, where they follow the prediction of the Debye approximation that the DOS will scale as  $\omega^2$ .[81] Similar agreement between VC and Gamma DOS at low frequencies was found in DFT predictions for  $\text{Si}_c\text{Ge}_{1-c}$ [22] and classical models of amorphous  $\text{Si}_c\text{Ge}_{1-c}$ . [107] The Debye approximation underpredicts the DOS at moderate frequency, which is due to non-linearities in the dispersion,[81] but the VC and Gamma predictions remain in good agreement.

The increasing average atomic mass with increasing concentration for the VC shifts all fre-

quencies downward by a factor  $1/[(1 - c)m^i + cm^j]^{1/2}$ . The increasing average atomic mass for the Gamma modes also reduces the frequencies, but not in a systematic manner. The effect of the disorder is seen at frequencies greater than ten by a broadening and shift of the Gamma DOS to higher frequencies because of the explicit use of light atoms in the supercell. This effect becomes more pronounced as the concentration increases. Duda et al. observed similar high-frequency broadening effects in model LJ alloys. [108] The high-frequency broadening is an indication of phonon localization, which is known to first occur at the Brillouin zone edge.[109] Based on the DOS, the vibrational modes of the explicitly disordered supercells at low frequencies are propagating, while the broadening of the DOS at high-frequency indicates that the Gamma vibrational modes may differ from the VC phonon modes in this regime. This behavior is further investigated in the next three sections.

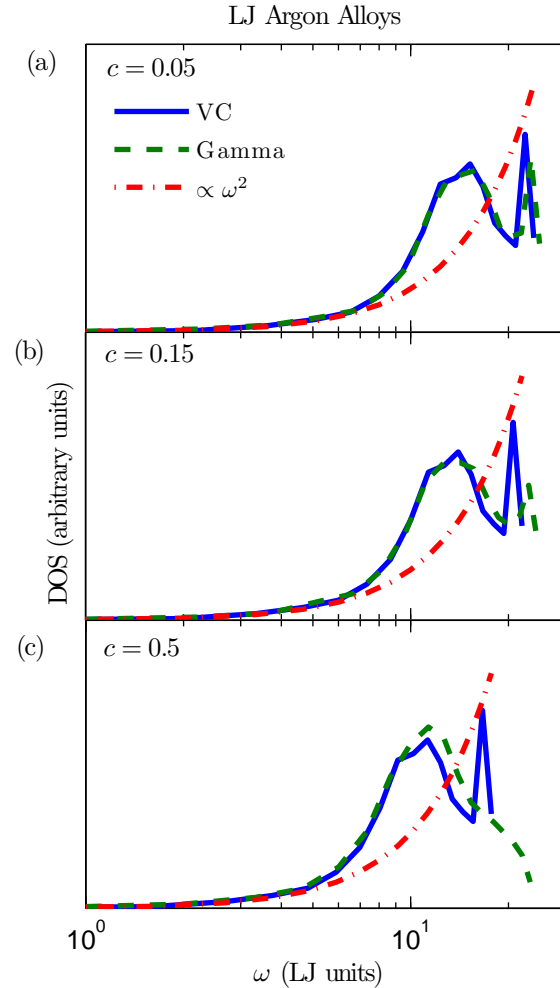


Figure 3.3: Vibrational DOS for LJ alloys calculated using the VC approximation and an explicitly disordered supercell (labeled Gamma) for concentrations of (a) 0.05, (b) 0.15, and (c) 0.5. VC and Gamma show similar low-frequency behavior for all concentrations. For increasing concentrations, the frequencies of both VC and Gamma decrease, while the high frequency DOS for Gamma spreads and reaches to a higher maximum frequency because of the explicit disorder. The supercells are of size  $N_0 = 12$  (6,912 atoms).

### 3.3.2 Dispersion and Group Velocity

The group velocity vector in a VC is defined as the gradient of the dispersion curve,

$$\mathbf{v}_{g,n}(\boldsymbol{\kappa}) = \frac{\partial \omega(\boldsymbol{\kappa}_\nu)}{\partial \boldsymbol{\kappa}}. \quad (3.4)$$

We calculate the group velocities for the VC using finite differences on the frequencies calculated from harmonic lattice dynamics.[84]

For a disordered solid, the three acoustic group velocities (two transverse and one longitudinal) can be predicted using the elastic constants [86] or by finite differencing of the three lowest frequency branches of the dispersion relation of the supercell. [18, 110] Except for this low-frequency behavior, there is not an accepted method to predict the group velocity of a vibrational mode in a disordered system, although there have been attempts. [18, 40, 108, 110, 111, 112] In the Cahill-Pohl model, for example, the group velocity of all disordered modes is the sound speed,  $v_s$ , which is also assumed for the high-scatter model, Eq. (3.3). [40] This assumption is not generally valid for any material.[18, 46, 108, 110, 111, 112, 113]

Calculating the structure factors of the supercell Gamma modes is a method to test for their plane-wave character at a particular wave vector and polarization corresponding to the VC. [46, 100] Feldman et al. used the structure factor to predict an effective dispersion for a model of amorphous silicon, but did not predict group velocities.[46] Volz and Chen used the dynamic structure factor to predict the dispersion of crystalline SW silicon using MD simulation. [114] Recently, the effective dispersion of a model disordered lattice was predicted using the structure factor. [113]

The structure factor at a VC wave vector  $\boldsymbol{\kappa}_{VC}$  is defined as[100]

$$S^{L,T}(\boldsymbol{\kappa}_{VC}) = \sum_\nu E^{L,T}(\boldsymbol{\kappa}_\nu) \delta[\omega - \omega(\boldsymbol{\kappa}=\mathbf{0})], \quad (3.5)$$

where the summation is over the Gamma modes,  $E^T$  refers to the transverse polarization and is

defined as

$$E^L(\kappa_{\nu}^{VC}) = \left| \sum_b \hat{\kappa}_{VC} \cdot e(\kappa_{\nu}^{=0} b) \exp[i\kappa_{VC} \cdot \mathbf{r}_0(l=0)] \right|^2 \quad (3.6)$$

and  $E^L$  refers to the longitudinal polarization and is defined as

$$E^T(\kappa_{\nu}^{VC}) = \left| \sum_b \hat{\kappa}_{VC} \times e(\kappa_{\nu}^{=0} b) \exp[i\kappa_{VC} \cdot \mathbf{r}_0(l=0)] \right|^2 . \quad (3.7)$$

In Eqs. (4.13) and (4.14), the  $b$  summations are over the atoms in the disordered supercell,  $\mathbf{r}_0(l=0)$  refers to the equilibrium atomic position of atom  $b$  in the supercell,  $l$  labels the unit cells ( $l = 0$  for the supercell),  $\alpha$  labels the Cartesian coordinates, and  $\hat{\kappa}_{VC}$  is a unit vector. Explicit disorder is included in the Gamma frequencies  $\omega(\kappa_{\nu}^{=0})$  and the  $3N_a$  components of the eigenvectors,  $e(\kappa_{\nu}^{=0} b)$ .

Physically,  $S^{L,T}(\omega)$  represents the frequency spectrum required to create a wavepacket with a well-defined wave vector and polarization. [46, 100, 115] For a perfect lattice, the structure factor peaks are delta functions centered at the mode frequencies, indicating that the modes are pure plane-waves (i.e., phonons). A sampling of the structure factors for the LJ argon alloys are plotted in Fig. 3.4 for wave vectors along the [100] and [111] directions in the  $N_0 = 10$  systems.

\* Well-defined peaks at all wave vectors are due to the lattice structure of the disordered systems. Typically, the structure factor for amorphous materials has well-defined peaks only for small wave vector.[46, 100] With increasing disorder, the structure factor spreads in width, particularly at high frequencies, which is an indication that the modes are not pure plane waves.

From Fig. 3.4, an effective dispersion curve (middle panels) can be extracted by locating the peaks in the structure factors at neighboring VC wave vectors. The peaks in the structure factor are larger than the VC predicted frequencies (plotted as solid lines in Fig. 3.4) by at most 5%. Similar agreement is found with the disordered SW silicon lattice supercells.

Even though there is good agreement between the VC-predicted dispersion curves and the peaks in the structure factors from Fig. 3.4, the effect of the width of the peaks is not clear. We

\*Due to the finite-size system, the delta function in Eq. (4.12) is broadened using a Lorentzian function with a full-width at half maximum set to  $20\delta_{\omega,avg}$ , where  $\delta_{\omega,avg}$  is the average frequency spacing. [45].

will use the group velocities predicted by the VC dispersion for both LJ argon and SW silicon in the VC-NMD and VC-ALD calculations for consistency and simplicity. The validity of this group velocity choice will be discussed in Section 3.3.5.

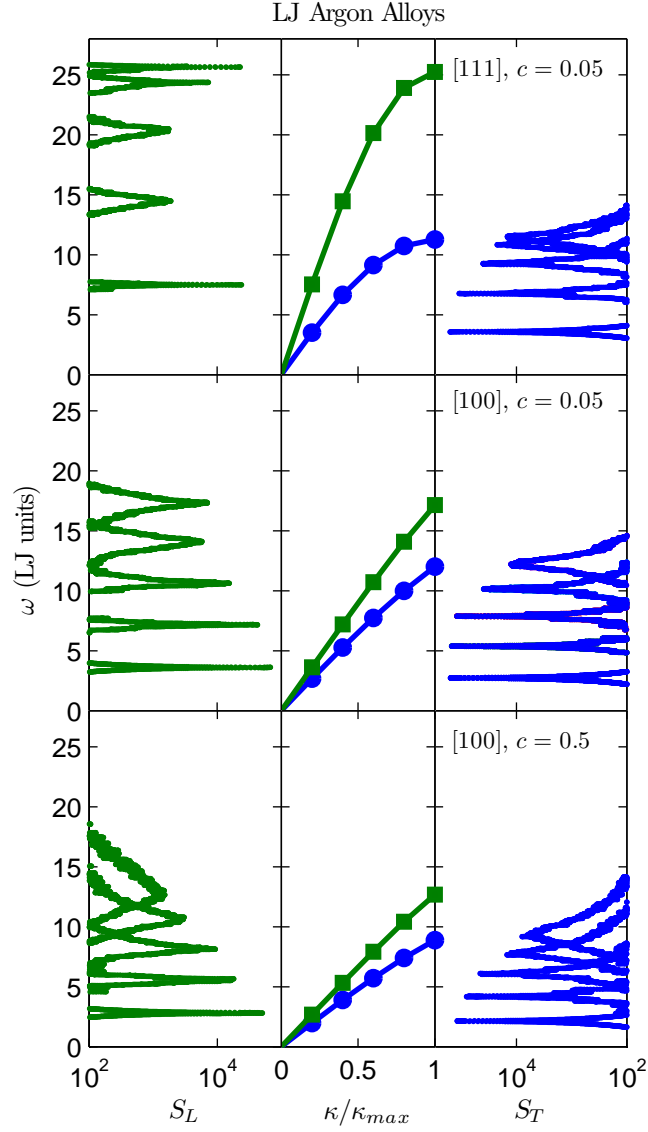


Figure 3.4: Left and right panels: The structure factor for longitudinal ( $S_L$ ) and transverse ( $S_T$ ) polarizations along high-symmetry directions of the mass disordered LJ argon supercells ( $N_0 = 10$ ,  $c = 0.05, 0.5$ ). Center panels: The VC predicted dispersion curves (solid lines) agree well with the locations of the peaks in  $S_L$  and  $S_T$  (data points). The wavenumber axis in the center panel is normalized by the maximum value of the wavenumber in the given direction.

### 3.3.3 Lifetimes

#### 3.3.3.1 From VC-NMD and Gamma-NMD

Once the group velocities are predicted using the VC dispersion, the mode lifetimes are required to predict the thermal conductivity using Eq. (3.1). As an alternative to the VC-ALD approach for predicting lifetimes, which is discussed in the next section, we first use the MD simulation-based NMD method.[27, 65, 66, 116] In NMD, the atomic trajectories are first mapped onto the vibrational mode coordinate  $q(\kappa; t)$  and its time derivative  $\dot{q}(\kappa; t)$  by [52]

$$q(\kappa; t) = \sum_{\alpha, b, l}^{3, n, N} \sqrt{\frac{m_b}{N}} u_\alpha(l_b; t) e^*(\kappa_b^\alpha) \exp[i\kappa \cdot \mathbf{r}_0(l_0)] \quad (3.8)$$

and

$$\dot{q}(\kappa; t) = \sum_{\alpha, b, l}^{3, n, N} \sqrt{\frac{m_b}{N}} \dot{u}_\alpha(l_b; t) e^*(\kappa_b^\alpha) \exp[i\kappa \cdot \mathbf{r}_0(l_0)]. \quad (3.9)$$

Here,  $m_b$  is the mass of the  $b_{th}$  atom in the unit cell,  $u_\alpha$  is the  $\alpha$ -component of the atomic displacement from equilibrium,  $\dot{u}_\alpha$  is the  $\alpha$ -component of the atomic velocity, and  $t$  is time. The total energy of each vibrational mode,  $E(\kappa; t)$ , is calculated from

$$E(\kappa; t) = \frac{\omega(\kappa)^2}{2} q(\kappa; t)^* q(\kappa; t) + \frac{1}{2} \dot{q}(\kappa; t)^* \dot{q}(\kappa; t). \quad (3.10)$$

The vibrational mode lifetime is predicted using

$$\tau(\kappa) = \int_0^{t^*} \frac{\langle E(\kappa; t) E(\kappa; 0) \rangle}{\langle E(\kappa; 0) E(\kappa; 0) \rangle} dt, \quad (3.11)$$

where the upper integration limit  $t^*$  is set to be much larger than the mode lifetime and the brackets indicate an ensemble average.[116] The NMD calculations scale as  $(N_a)^2$ .[17]

We perform the MD simulations using the fully disordered supercells and project onto the

frequencies and eigenvectors from both the VC unit cell [ $\omega(\kappa_\nu)$ ,  $e(\kappa_\nu^b)$ ] and the Gamma supercell [ $\omega(\kappa=0)$ ,  $e(\kappa=0^b)$ ]. Previous studies of disordered supercells with the NMD method have used the Gamma modes only to perform the projections. [105, 110, 111, 112, 117] The trajectories from the MD simulations are also used in the GK method calculations (Section 3.4). The MD simulations were ten times longer than the longest lifetime in the system, which was estimated from the VC-ALD predicted lifetimes. For LJ argon and SW silicon, data was collected for  $2^{20}$  and  $2^{22}$  time steps and the atomic trajectories were sampled every  $2^8$  and  $2^4$  time steps. Ensemble averaging of the energy autocorrelations was performed using ten independent, initially-randomized velocity distributions.

For the normal modes of the lattice supercell, where the energy autocorrelation follows an exponential decay,[27, 65] Eq. (3.11) is exact, but this expression becomes an approximation when using the VC normal modes to perform the mappings in Eqs. (3.8) and (4.19). Even for larger disorder ( $c = 0.5$ ), where the energy autocorrelations deviate from an exponential decay, an effective lifetime can still be predicted using Eq. (3.11) (see Appendix A.4). The lifetimes predicted using VC-NMD and Gamma-NMD are shown in Figs. 3.5(a)-3.5(d) for the LJ argon crystal and all alloys at a temperature of 10 K. The range of frequencies for VC-NMD and Gamma-NMD differ slightly due to differences in the DOS (see Fig. 3.3). For a small interval of frequency, there is a wider range of predicted lifetimes for Gamma-NMD. This spread is because there is no symmetry-averaging of the mode properties, which is possible for the VC by considering the crystal lattice's irreducible Brillouin zone.[81]

The lifetimes predicted by both VC-NMD and Gamma-NMD show a  $\omega^{-2}$  scaling at low frequency and a  $\omega^{-4}$  scaling (for the alloys) and even faster for mid-range frequencies. The  $\omega^{-2}$  scaling is due to three-phonon scattering processes [63, 69]. The  $\omega^{-4}$  scaling is due to phonon-mass point defect scattering.[30, 31, 32, 33] A constant lifetime is observed at the highest frequencies for both VC-NMD and Gamma-NMD except at  $c = 0.5$  for VC-NMD. We are not aware of any theoretical prediction of this high-frequency behavior.

The majority of the lifetimes predicted by both VC-NMD and Gamma-NMD are larger than

the Ioffe-Regel (IR) limit, [2]

$$\tau_{IR} = \frac{2\pi}{\omega}. \quad (3.12)$$

The physical interpretation of the IR limit is a mode that scatters in a time equal to its oscillation period. Our results suggest that the IR limit is a good lower-limit for the lifetimes predicted by VC-NMD and Gamma-NMD for LJ argon (Fig. 3.5) and VC-NMD for SW silicon [see Fig. 3.9(a) in Section 3.5].

Overall, good agreement is seen in the predicted lifetimes from VC-NMD and Gamma-NMD in both magnitude and trends. The use of the VC normal modes is an approximation that becomes worse as the concentration is increased (see Appendix A.4), but our results suggest that the effect is only pronounced at the highest frequencies and at high alloy concentrations. The only approximation associated with Gamma-NMD is the use of the harmonic lattice dynamics-predicted frequencies and eigenvectors to map the atomic trajectories from the fully anharmonic MD simulations. This assumption has been shown to be valid for LJ argon below temperatures of 40 K.[27] Based on the good agreement with Gamma-NMD, the VC-NMD lifetimes are used along with the VC group velocities to predict thermal conductivity in Section 3.4. For Gamma-NMD, there is no accepted way to predict the mode group velocities, so that the thermal conductivity cannot be predicted using Eq. (3.1).

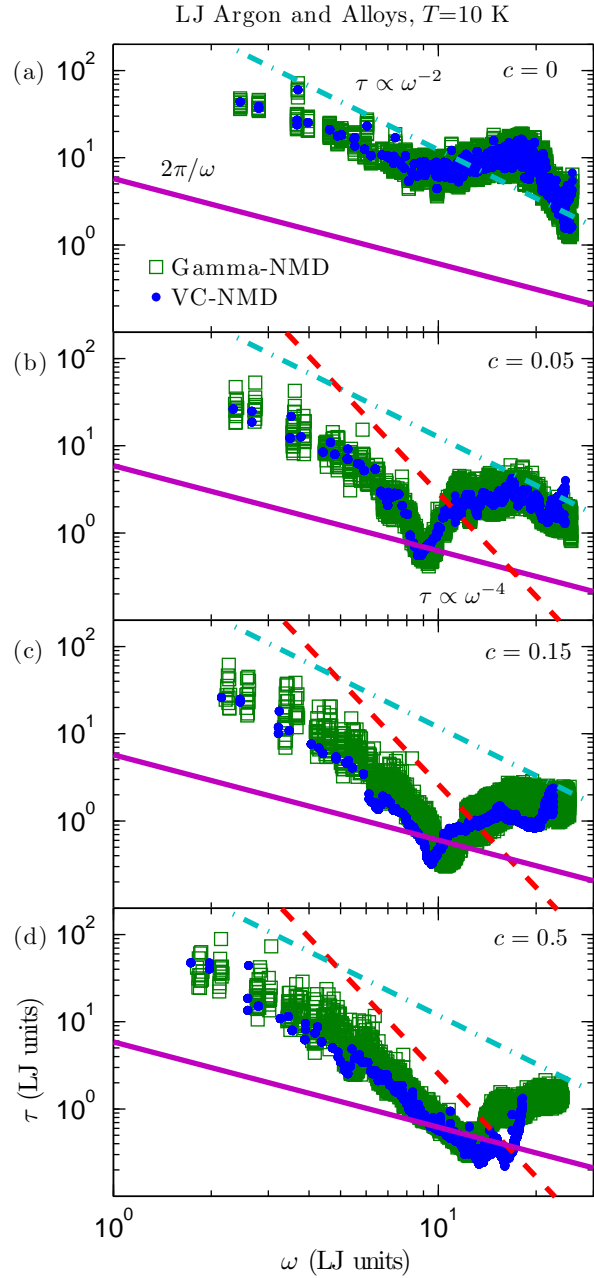


Figure 3.5: Lifetimes predicted using VC-NMD and Gamma-NMD from MD simulations of (a) perfect LJ argon and (b),(c),(d) mass-disordered LJ alloys for  $N_0 = 10$ .  $\omega^{-2}$  and  $\omega^{-4}$  scalings are observed at low to mid frequencies. For both VC-NMD and Gamma-NMD, most mode lifetimes are greater than the Ioffe-Regel limit of  $2\pi/\omega$ . [2] While there is more scatter in the Gamma-NMD data (see Section 3.3.3.1), the lifetime magnitudes and trends agree well, an important consideration when comparing the VC-NMD and VC-ALD lifetimes in Fig. 3.6(a).

### 3.3.3.2 From VC-ALD

Under the VC approximation, the ALD calculations[27] are performed on the conventional unit cells of LJ argon and SW silicon with a single atomic mass based on the alloy concentration. The ALD calculations scale as  $b^4(N_0)^2$ .[17] Disorder is not included explicitly but is treated using perturbation theory. Assuming phonon scattering mechanisms to operate independently, the effective phonon lifetime can be found using the Matthiessen rule, [19]

$$\frac{1}{\tau(\nu)} = \frac{1}{\tau_{p-p}(\nu)} + \frac{1}{\tau_{p-d}(\nu)}, \quad (3.13)$$

where  $\tau_{p-p}(\nu)$  accounts for intrinsic phonon-phonon scattering and  $\tau_{p-d}(\nu)$  accounts for phonon-defect scattering.

Phonon-phonon scattering in ALD is modeled by including three-phonon processes.[22, 26, 27] The present study is concerned with temperatures much less than the melting temperature of either LJ argon [28] or SW silicon[6] so that we believe the effects of higher-order phonon processes are negligible.[27, 29] We predict the phonon-phonon lifetimes using the method described in Ref. 27, with all classical expressions for the populations to remain consistent with the classical MD-based methods from Section 3.3.3.1.

Using perturbation theory, Tamura derived a general expression for phonon scattering by mass point defects to second order that was applied to study isotopic germanium.[33] By considering the symmetry properties of the FCC lattices considered in this work, his expression reduces to

$$\frac{1}{\tau_{p-d}(\nu)} = \frac{\pi}{2} g_2 \omega^2(\nu) DOS[\omega(\nu)], \quad (3.14)$$

where

$$g_n = \sum_{\mu} c^{\mu} (1 - m^{\mu}/\bar{m}^{\mu})^n. \quad (3.15)$$

Here,  $c^\mu$  and  $m^\mu$  are the concentration and mass of the  $\mu$ -th species and  $\bar{m}^\mu$  is the average mass. Bond disorder can be accounted for using a similar expression with an average atomic radius or suitable scattering cross-section. [30, 31] For the binary LJ argon and SW silicon alloys considered here, there is one atom type in the unit cell with  $\mu = i, j$ , so that the alloying atom labeled by  $m_c^j$  can be considered to be an “isotope” of the atom labeled  $m_{1-c}^i$ .

The lifetimes predicted by VC-ALD for LJ argon at a concentration of 0.05 are plotted in Fig. 3.6(a). <sup>†</sup> Also plotted are the lifetimes for the perfect system and from the VC-NMD predictions [Fig. 3.5(b)] at this concentration. At low frequencies, where the DOS is Debye-like [ $D(\omega) \propto \omega^2$ , Fig. 3.3],  $\tau_{p-p}(\kappa)$  scales as  $\omega^{-2}$ , a scaling also observed in the VC-NMD and Gamma-NMD lifetimes. Under the Debye-approximation, the phonon scattering due to mass point-defects is predicted to scale as  $\omega^{-4}$  from Eq. (3.14). [32, 33] This scaling is observed in the VC-NMD, Gamma-NMD, and VC-ALD predicted lifetimes in the mid-frequency range. VC-ALD does not predict the frequency-independent lifetimes at high frequency for LJ argon observed in VC-NMD and Gamma-NMD, and a significant number fall below the IR limit. The lifetimes predicted by NMD and ALD for the perfect LJ argon crystal agree within 20% on a mode-by-mode basis, and the resulting thermal conductivities agree within their uncertainties (see Table 3.1).

Tamura applied his theory to predict the reduction of lifetimes in isotopic germanium, which is weakly disordered ( $\sim 5\%$  variation in the atomic masses). In the LJ alloys, the masses differ by a factor of three. Large mass ratios were also considered in DFT VC-ALD studies of SiGe (mass ratio of 2.6)[22], PbTeSe (2.6)[26], and MgSiSn (4.9)[35]. The importance of higher-order interactions in the Tamura theory can be estimated by the disorder strength (i.e.,  $g_n$  for  $n > 2$ ).[33] For isotopically-disordered germanium, Tamura estimated that the higher-order contributions were negligible ( $g_2 = 5.87 \times 10^{-4}$ ,  $g_3 \sim 10^{-7}$ , and  $g_4 \sim 10^{-7}$ ).[33] For LJ argon at a concentration of 0.15,  $g_2 = 0.3018$ ,  $g_3 = -0.3250$  and  $g_4 = 0.4411$ . It is possible that the

<sup>†</sup>To perform the calculation of Eq. (3.14), it is necessary to broaden the DOS using a Lorentzian function. [33] We use a value of  $100\delta_{\omega,avg}$ .

neglect of the higher-order interactions in the Tamura theory is responsible for the discrepancy of the lifetimes predicted by VC-NMD and Gamma-NMD versus VC-ALD at high frequencies. Full evaluation of the higher-order interactions in the Tamura theory is of similar complexity to anharmonic phonon interaction, [27, 29, 69] and is beyond the scope of this work.

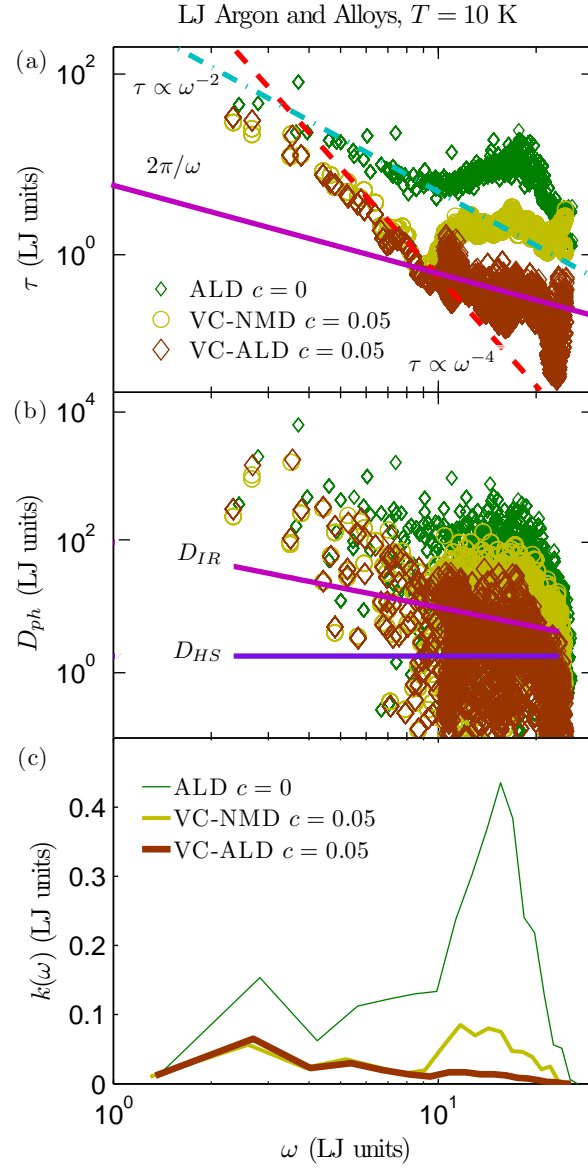


Figure 3.6: (a) Predicted lifetimes using VC-NMD and VC-ALD for LJ argon ( $T = 10$  K,  $N_0 = 10$ , and  $c = 0.05$ ). (b) Mode diffusivities compared to the high-scatter limit,  $D_{HS}$  [Eq. (3.18)], and IR limit,  $D_{IR}$  [Eq. (3.19)]. VC-NMD and VC-ALD predict a large number of high-frequency modes with  $D_{ph} < D_{HS}$ . (c) Thermal conductivity frequency spectrum, which peaks at high frequency, in contrast to SW silicon [(Fig. 3.9(c)].

### 3.3.4 Diffusivities

We now use the AF theory to provide a lower limit for the contribution of a given vibrational mode to thermal conductivity. While studies have been performed on alloying the amorphous phase, [45] the AF theory has not been previously applied to disordered lattices. In the classical, harmonic limit for specific heat, a mode's contribution to the thermal conductivity of is determined by its diffusivity,

$$D_{ph,\mathbf{n}}(\boldsymbol{\nu}) = v_{g,\mathbf{n}}^2(\boldsymbol{\nu}) \tau(\boldsymbol{\nu}), \quad (3.16)$$

such that from Eq. (3.1)

$$k_{ph,\mathbf{n}} = \sum_{\boldsymbol{\kappa}} \sum_{\nu} \frac{k_B}{V} D_{ph,\mathbf{n}}(\boldsymbol{\nu}). \quad (3.17)$$

The lower limit for phonon diffusivity is zero since the group velocities can be zero (e.g., optical modes at the Brillouin zone center).

In the high-scatter limit,[40] the diffusivity of each mode is

$$D_{HS} = \frac{1}{3} v_s a, \quad (3.18)$$

which leads to Eq. (3.3). The physical interpretation of Eq. (3.18) is that all vibrational modes transport heat at the sound speed and have a mean free path of the lattice spacing. Based on the IR limit, another possible lower-bound of diffusivity is

$$D_{IR} = \frac{2\pi}{3} \frac{v_s^2}{\omega}. \quad (3.19)$$

To evaluate Eqs. (3.18) and (3.19), the sound speed is estimated by

$$v_s = \frac{1}{3} v_{s,L} + \frac{2}{3} v_{s,T}, \quad (3.20)$$

where  $v_{s,L}$  and  $v_{s,T}$  are the longitudinal and transverse sound speeds calculated from the elas-

tic constants, [86] which agree within 20% with the branch-averaged sound speeds along the high-symmetry dispersion directions [100],[110], and [111]. For LJ argon and SW silicon,  $v_s = 6.93$  (LJ units) and 5,790 m/s. The Cahill-Pohl model assumes Eq. (3.19) for the mode diffusivities.[40] As seen in Fig. 3.6(b) for the LJ argon alloy at a concentration of 0.05, VC-NMD and VC-ALD predict [from Eq. (3.16), using the  $x$ -component of group velocity], a significant number of modes with  $D_{ph}(\kappa)$  less than  $D_{HS}$ , and  $D_{IR}$  approaches  $D_{HS}$  at high frequencies. For both VC-NMD and VC-ALD, we approximate  $\mathbf{v}_{g,n}(\kappa)$  from the VC dispersion (Section 3.3.2) so that any differences in diffusivity  $D_{ph}$  will come from the predicted lifetimes.

In a disordered system, modes can transport heat by harmonic coupling in the AF theory of diffusons.[44] While the high-scatter model assumes a mode-independent diffusivity, the AF theory is capable of predicting mode-specific thermal diffusivities  $D_{AF}$ . [45, 46, 118] Since the AF theory is harmonic, the diffusivities typically diverge as the frequency approaches zero because these vibrations are long-wavelength plane waves that are weakly scattered by the disorder. [119, 120] The mode-specific diffusivities,  $D_{AF}$ , of an LJ argon amorphous phase (see Section 4.3)<sup>‡</sup> are plotted in Fig. 3.7 along with  $D_{HS}$  and  $D_{IR}$ . Except at the highest frequencies, the diffusivity of all amorphous modes can be approximated using the mode-independent diffusivity  $D_{HS}$ . The lower-limit  $D_{IR}$  is clearly an overprediction for the amorphous mode diffusivities. Also plotted in Fig. 3.7 are diffusivities predicted from the AF theory for the explicitly-disordered LJ argon lattice supercell alloy at a concentration of 0.5. As expected, the AF theory predictions diverge at low frequency.<sup>§</sup> The diffusivity of all modes are larger than  $D_{HS}$  except at the highest frequencies, where they tend to zero as with the amorphous phase. This result supports the hypothesis that the lower-bound of the VC predicted phonon diffusivity should be  $D_{HS}$  (and not zero as for a crystal), which is further explored in Sections 3.4 and 3.5.

<sup>‡</sup>For a finite system, the AF theory requires a frequency broadening to predict the mode-specific thermal diffusivities. [44] We broaden using a Lorentzian function with a width  $\delta_{\omega,avg}$ .

<sup>§</sup>For the LJ alloys with  $c \leq 0.15$ , the predicted  $k_{AF}$  is strongly system-size dependent, indicating this diverging behavior. For LJ argon alloys at  $c = 0.5$ , the divergence with system size is small for the range of system size studied ( $N_0 = 4$  to  $N_0 = 12$ ). For  $N_0 = 12$ ,  $k_{AF}/k_{GK} = 0.93$  because the finite system-size limits the diffusivities of the lowest frequencies.

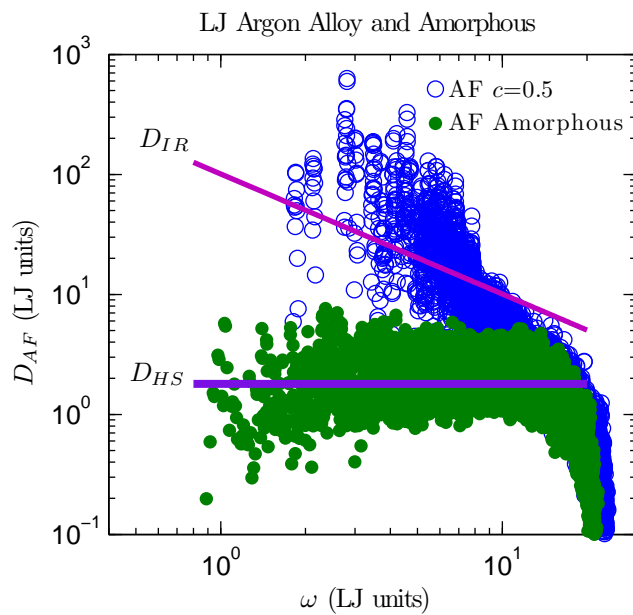


Figure 3.7: AF theory predictions of disordered mode diffusivities for LJ argon alloy and amorphous phases. The amorphous phase is well-described by a mode-independent diffusivity  $D_{HS}$  [Eq. (3.18)]. The system size for the alloy is  $N_0 = 10$  (6,912 atoms), and the amorphous phase has 6,912 atoms.

### 3.3.5 Discussion

In this section, in anticipation of the thermal conductivity predictions in Section 3.4, we discuss two possible sources of error in the VC-predicted mode properties. To start, we note that for disordered systems, it is generally only possible to assign a unique lifetime and group velocity to vibrational modes in the low-frequency, propagating limit. [46, 121] The mode diffusivity is the fundamental transport property. [44, 45, 46]

We believe that the VC-predicted group velocities, particularly for  $v_{g,n}(\kappa) \approx 0$ , are an underprediction of the velocity scale required to evaluate Eq. (3.16). This statement is supported by the AF-theory diffusivities plotted in Fig. 3.7, which are finite for the majority of the frequency range the LJ alloy at a concentration of 0.5. While the diffusivity from Eq. (3.16) can be zero because of the VC predicted group velocities, this result is not consistent with the AF theory predictions.

The VC-NMD and Gamma-NMD predicted lifetimes are generally larger than the IR limit for LJ argon and its alloys (see Fig. 3.5). The constant lifetime observed at the highest frequencies for both VC-NMD (except at  $c = 0.5$ ) and Gamma-NMD is consistent with the plateau of mode diffusivity at high frequency predicted for a model disordered lattice, which was explained by a plateau in the vibrational mode lifetimes. [122] Recently, a study of model disordered lattices predicted the mid-frequency minimum and the high-frequency plateau of the mode diffusivities.[113] Similar behavior of the mode diffusivities has been observed in model jammed systems.[120, 121] VC-ALD predicts essentially monotonically decreasing lifetimes with increasing frequency for the LJ argon alloys [Fig. 3.6(a)] with many falling below the IR limit. Because VC-NMD and VC-ALD use the same values for  $v_{g,n}(\kappa)$ , the mode diffusivities will therefore be underpredicted for VC-ALD compared to VC-NMD for the LJ argon alloys because of the lifetime underprediction.

### 3.4 Thermal Conductivity Prediction

The thermal conductivities of the LJ systems can now be predicted from Eq. (3.1) using the vibrational mode properties from VC-NMD and VC-ALD. Given the discussion regarding the VC-predicted mode properties in Section 3.3.5, we also predict thermal conductivity using the equilibrium MD-based GK method, which is a top-down method that does not make any approximations about the nature of the vibrational modes. Thermal conductivities predicted by the GK method naturally capture all scattering mechanisms. [18, 59, 105] The heat current was computed every ten time steps from the same atomic trajectories (positions and velocities) used for the VC-NMD and Gamma-NMD calculations. The thermal conductivity is determined from the maximum of the integral of the heat current autocorrelation function.

The thermal conductivities predicted by VC-NMD, VC-ALD, and GK are system size-dependent [i.e.,  $k = k(N_0)$ ] for all lattices and methods except perfect LJ argon from GK.[66] To predict a bulk thermal conductivity,  $k_{bulk}$ , a linear extrapolation procedure is used, whereby

$$\frac{k(N_0)}{k_{bulk}} = 1 - \frac{c_0}{N_0}, \quad (3.21)$$

where  $c_0$  is a constant.[17, 25, 78] The thermal conductivity is predicted for varying system sizes and the bulk thermal conductivity is obtained by fitting Eq. (3.21) to the data. For VC-NMD and VC-ALD, the validity of Eq. (3.21) requires that the low-frequency modes be dominated by phonon-phonon scattering (i.e.,  $\tau \propto \omega^{-2}$ ) and follow the Debye approximation with respect to the group velocity and DOS. [25, 78] For the LJ argon alloys, this requirement is satisfied for modest system sizes (for  $N_0 = 6$  to 12) so that both VC-NMD and VC-ALD thermal conductivity predictions can be extrapolated to a bulk value.

Bulk thermal conductivity predictions for the LJ argon alloys using VC-NMD, VC-ALD, and GK are tabulated in Table 3.1 and plotted in Fig. 3.8. Also plotted in Fig. 3.8 is the high-scatter thermal conductivity prediction  $k_{HS}$  [Eq. (3.3)]. The thermal conductivity predicted for the LJ

amorphous phase by GK is 0.17 W/m-K, which is in good agreement with  $k_{HS}$  (0.16 W/m-K) for the perfect crystal. The predicted thermal conductivities of the LJ argon alloys at high concentration are a factor of two to three larger than  $k_{HS}$ . While agreement between the three methods is found for the perfect crystal, VC-NMD and VC-ALD underpredict the alloy thermal conductivities compared to GK. The underprediction is modest for VC-NMD, where  $k_{NMD}$  is 80% of  $k_{GK}$  or greater for all concentrations. The VC-ALD method significantly underpredicts the thermal conductivity of the LJ argon alloys. The largest deviation is at a concentration of 0.05, where  $k_{VC-ALD}$  is 56% of  $k_{GK}$ .

In Section 4.4.5, we argued for the existence of a minimum mode diffusivity,  $D_{HS}$  [Eq. (3.18)]. As shown in Fig. 3.6(b), the diffusivities of many high-frequency modes in the LJ alloys, predicted by both VC-NMD and VC-ALD, fall below this limit. Based on this observation, we propose that any diffusivity below the limit be set to  $D_{HS}$  for thermal conductivity prediction. The results of this adjustment, referred to as VC-NMD\* and VC-ALD\*, are plotted in Fig. 3.8 and included in Table 3.1. The adjusted thermal conductivities predicted by VC-NMD\* are now within 10% of the GK value for all concentrations, which is within the prediction uncertainties. Combined with  $D_{HS}$ , we believe that the VC-NMD predicted diffusivities are good representations for the explicitly-disordered modes present in the MD simulations. Another possible adjustment,  $D_{IR}$  [Eq. (3.19)], results in a thermal conductivity of  $0.94 \pm 0.09$  W/m-K for the LJ argon alloy at a concentration of 0.05, well above the value predicted by GK. We also note that the thermal conductivity of the amorphous phase is well-modeled by a mode-independent diffusivity  $D_{HS}$ , while  $D_{IR}$  overpredicts for all modes in the amorphous phase (see Fig. 3.7). Thus, we believe that  $D_{HS}$  is the more appropriate high-scatter limit.

By applying the high-scatter limit adjustment VC-ALD\*, the thermal conductivities are brought into marginally better agreement with the GK values, worst for a concentration of 0.05, where  $k_{VC-ALD^*}$  is 65% of  $k_{GK}$ . As seen in Fig. 3.6(b), the VC-ALD method fails to accurately predict the high-frequency mode diffusivities for LJ argon alloys. Since the group velocities are the same for VC-NMD and VC-ALD, the underprediction of the high-frequency diffusivities is due to the

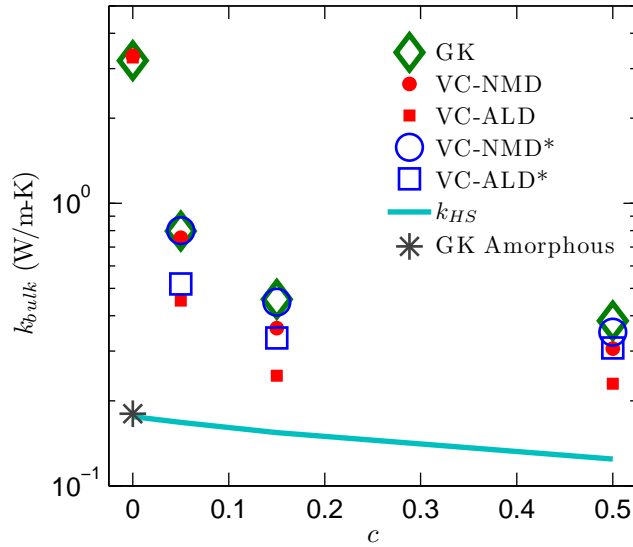
LJ Argon and Alloys,  $T=10$  K

Figure 3.8: Thermal conductivity predictions for LJ argon and alloys at  $T=10$  K using the VC-NMD, VC-ALD, and GK methods. The high-scatter thermal conductivity prediction  $k_{HS}$  [Eq. (3.3)] and the high-scatter adjusted VC-NMD\* and VC-ALD\* are also plotted.

underprediction of the high-frequency mode lifetimes from VC-ALD compared to VC-NMD. We know that the VC-NMD predicted lifetimes are more accurate values due to their agreement with Gamma-NMD [Fig. 3.5].

The thermal conductivity spectrum, defined as the contribution to thermal conductivity of modes at a given frequency, is plotted in Fig. 3.6(c) for VC-NMD and VC-ALD for the perfect crystal and the alloy with a concentration of 0.05. The thermal conductivity of LJ argon and its alloys has important contributions from high-frequency modes. VC-ALD underpredicts the high-frequency diffusivities compared to VC-NMD, which leads to an underprediction of the high-frequency thermal conductivity spectrum compared to VC-NMD. This result can be traced back to an underprediction of the high-frequency lifetimes compared to VC-NMD and Gamma-NMD [Fig. 3.6(a)].

Table 3.1: Thermal conductivity predictions using the VC-NMD, VC-ALD, and GK methods. For LJ argon alloys, the bulk extrapolation is used for all three methods. For SW silicon alloys, only VC-ALD and GK can be used to extrapolate a bulk thermal conductivity (see Section 3.4). For VC-NMD and GK, the uncertainties are estimated by omitting independent simulations from the ensemble averaging (see Section 4.3). For VC-ALD, the uncertainties are estimated by omitting extrapolation points used for Eq. (3.21).

$c$	GK	VC-NMD	VC-ALD	VC-NMD*	VC-ALD*
<b>LJ</b>					
0.00	$3.3 \pm 0.1$	$3.3 \pm 0.1$	$3.4 \pm 0.1$		
0.05	$0.80 \pm 0.07$	$0.76 \pm 0.07$	$0.45 \pm 0.02$	$0.80 \pm 0.1$	$0.52 \pm 0.05$
0.15	$0.46 \pm 0.07$	$0.36 \pm 0.04$	$0.24 \pm 0.01$	$0.45 \pm 0.05$	$0.33 \pm 0.07$
0.50	$0.38 \pm 0.07$	$0.31 \pm 0.04$	$0.23 \pm 0.01$	$0.35 \pm 0.05$	$0.31 \pm 0.07$
<b>SW</b>					
0.00	$520 \pm 30$		$480 \pm 20$		
0.05	$20 \pm 2$		$24 \pm 2$		$24 \pm 2$
0.15	$9.9 \pm 0.9$		$12 \pm 1$		$12 \pm 1$
0.50	$9.3 \pm 0.9$		$11 \pm 1$		$11 \pm 1$

### 3.5 SW silicon

The failure of VC-ALD to predict the thermal conductivities of the LJ alloys is due to an under-prediction of the high-frequency mode lifetimes, which make an important contribution to the thermal conductivity [see Sections 4.4.5 and 3.4, Figs. 3.6(a) and 3.6(c)]. To provide a contrast, we now predict the vibrational mode properties and thermal conductivity for bulk and alloyed SW silicon, where it is known that low-frequency modes dominate the thermal conductivity. [68, 106] The lifetimes for the perfect crystal and an alloy with a concentration of 0.5 predicted by VC-NMD and VC-ALD are plotted in Fig. 3.9(a). The VC-NMD predicted lifetimes are generally larger than the IR limit for SW silicon alloys, similar to the VC-NMD predictions for the LJ argon alloys (Fig. 3.5). Unlike the LJ argon alloys, the VC-NMD and VC-ALD predicted lifetimes agree over most of the frequency spectrum, except at the highest frequencies, where VC-ALD underpredicts VC-NMD and falls below the IR limit. The high-frequency plateau of the VC-NMD predicted lifetimes for LJ argon (Fig. 3.5) is not seen for SW silicon. As seen in Figs. 3.6(b) and 3.9(b), VC-NMD and VC-ALD both predict a significant number of modes with  $D_{ph}(\kappa)$  less than  $D_{HS}$  for both the LJ argon and SW silicon alloys.

The thermal conductivity spectra for bulk SW silicon and an alloy with a concentration of 0.5 are plotted in Fig. 3.9(c). For bulk and the alloy, the thermal conductivity is dominated by low-frequency modes, so that large system-sizes are needed to satisfy the extrapolation requirements and only GK and VC-ALD can be used to predict a bulk value from Eq. (3.21). While a previous study found that it was necessary to use cell sizes of  $N_0 = 60$  for Tersoff silicon alloys,[117] we find that Eq. (3.21) is valid for SW silicon and  $38 \leq N_0 \leq 42$ . This system-size requirement highlights the efficiency of the VC-ALD method compared to VC-NMD, which is necessary when computationally-expensive DFT calculations are used. [22, 24, 25, 26, 123, 124] The bulk thermal conductivity predictions for VC-ALD and GK are shown in Table 3.1 and plotted in Fig. 3.10. The alloy thermal conductivities predicted by VC-ALD are 20% larger than those from GK, in contrast to VC-ALD underpredicting for LJ argon alloys. This overprediction by VC-

ALD compared to GK is close to the overprediction (15%) of VC-ALD using DFT calculations of SiGe alloys compared to experiment without including disorder explicitly.[22]

The predicted thermal conductivities for the SW silicon alloys at all concentrations are over an order of magnitude larger than the high-scatter prediction,  $k_{HS}$ . Because the thermal transport in SW silicon is dominated by low-frequency modes, the high-scatter adjustment VC-ALD\* is within one percent compared to the unadjusted VC-ALD. While higher-order interactions in the Tamura theory may be responsible for the discrepancy of the lifetimes predicted by VC-NMD and VC-ALD in SW silicon at the highest frequencies [Fig. 3.9(a)], this effect is not important to the overall thermal transport. VC-ALD predicts accurate alloy thermal conductivities for SW silicon because it is a low-frequency dominated material, which is the frequency range where the standard application of the Tamura theory is valid.[33]

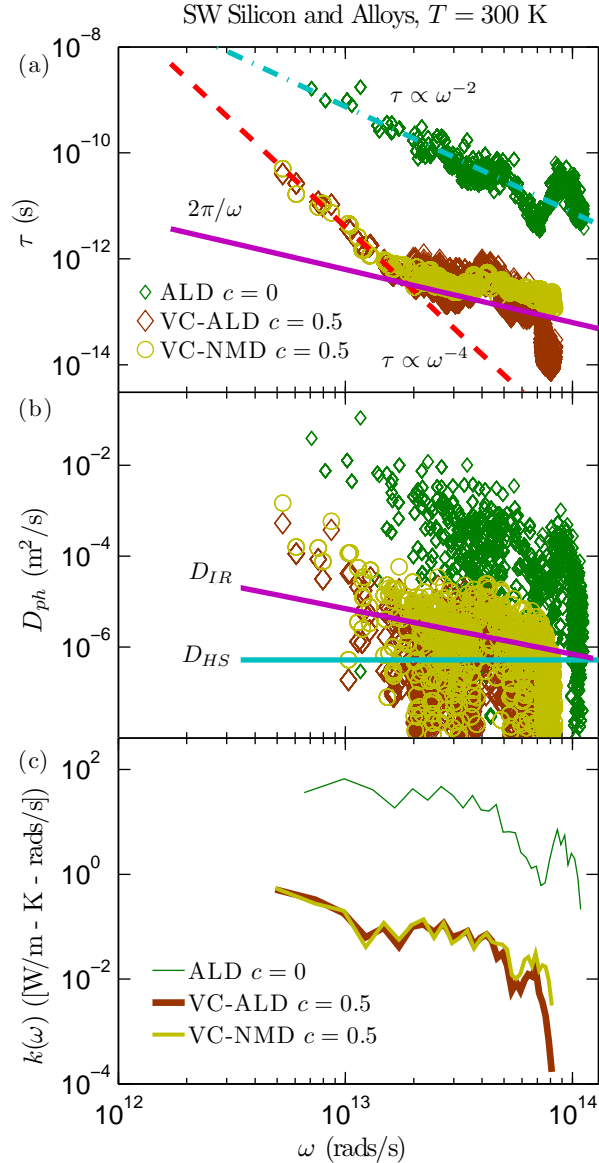


Figure 3.9: (a) Predicted lifetimes using VC-NMD and VC-ALD for SW silicon ( $T = 300$  K,  $N_0 = 8$ , and  $c = 0.05$ ). (b) Mode diffusivities compared to the high-scatter limit,  $D_{HS}$  [Eq. (3.18)], and the IR limit,  $D_{IR}$  [Eq. (3.19)]. VC-NMD and VC-ALD predict a large number of high-frequency modes with  $D_{ph} < D_{HS}$ , as seen in the LJ argon alloys [Fig. 3.6(b)]. (c) Thermal conductivity frequency spectra, which peak at low frequency, in contrast to LJ argon [Fig. 3.6(c)].

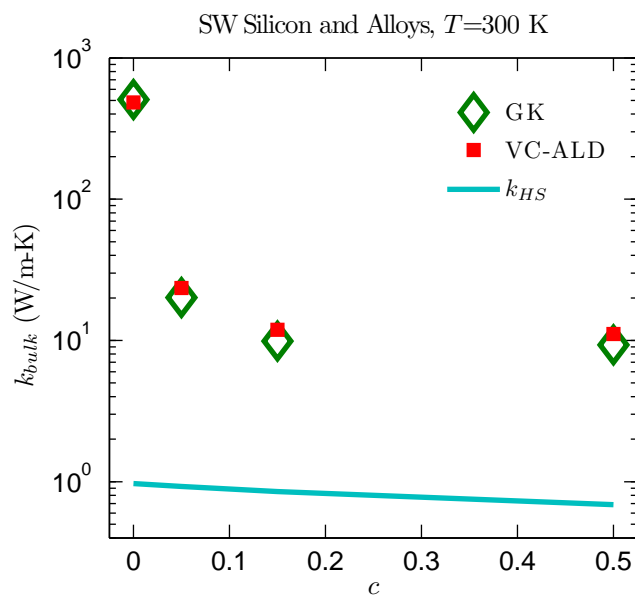


Figure 3.10: Thermal conductivity predictions for SW silicon and alloys at a temperature of 300 K using the VC-ALD and GK methods. The high-scatter thermal conductivity prediction  $k_{HS}$  is also plotted. The adjusted VC-ALD\* is not shown since it differs by less than one percent compared to VC-ALD.

## 3.6 Summary

In this study, we investigated the use of the VC approximation for predicting the vibrational mode properties and thermal conductivity of LJ argon and SW silicon alloys by a detailed comparison of the VC-NMD, VC-ALD, and GK methods. By using computationally-inexpensive empirical potentials we self-consistently studied the effects of disorder both explicitly (Sections 3.3.1, 3.3.2, 3.3.3.1, 4.4.5, and 3.5) and as a perturbation (Sections 3.3.3.2 and 3.5). By spanning a range of disorder, the limits of the perturbative models were examined. A breakdown of the VC-ALD method was identified for LJ argon alloys by a comparison with the VC-NMD method in Section 3.3.3.2 and a correction was suggested in Section 3.4. The mode properties and thermal conductivity of the SW silicon alloys were predicted in Section 3.5 and provided a contrast to the LJ argon alloys, which have a different thermal conductivity spectrum.

The results for the SW silicon and LJ argon alloys suggest that modeling of thermal transport in ordered and disordered lattices can be separated into two broad groups: low-frequency dominated and full-spectrum materials. Materials dominated by low-frequency modes tend to have high thermal conductivities that are significantly larger than the high-scatter limit [Eq. (3.3)], which is due to the large group velocities and long lifetimes of low-frequency modes.[22, 24, 34, 37, 38, 39, 99, 125] These low-frequency modes closely follow the scalings predicted by the perturbative VC-ALD models, which are valid at low-frequencies.

LJ argon is a material whose thermal transport has significant contribution from high-frequency modes, even for the bulk [see Fig. 3.6 (c)]. This high-frequency range is where we predict that the perturbative Tamura theory will have non-negligible contributions from higher-order interactions (see Section 3.3.3.2). While the higher-order interactions in the Tamura theory are also predicted to be non-negligible for SW silicon, this does not affect the thermal conductivity predictions significantly because high-frequency modes are not important to thermal transport. The negligible contributions of high-frequency modes is demonstrated by experimental measurements of the thermal conductivity of SiGe alloys, which exceed the high-scatter limit by more than an

order of magnitude at room temperature for all compositions. [38, 39, 40, 125] Experimentally-accurate theoretical predictions[22] also demonstrate that high-frequency modes are unimportant to thermal transport, although they do serve as important scattering channels. [21]

The VC-ALD method provides a computationally inexpensive framework, which is essential when using *ab initio* methods for predicting thermal conductivity. [21, 22, 24, 25, 26, 35, 36, 41, 78] Based on our results, we believe that the Tamura theory breaks down for mode diffusivities predicted to be below the high-scatter limit,  $D_{HS}$  [Eq. (3.18)]. This breakdown may be true for the high-frequency modes of any disordered lattice[122] and the high-scatter limit  $D_{HS}$  should be considered whenever the perturbative VC-ALD method is used. Although the high-scatter limit of diffusivity is usually interpreted as a minimum mean free path, [40, 90, 122, 126] we find that this concept is not necessary for interpreting the results of this work. In a disordered lattice, the fundamental quantities are the mode lifetime and diffusivity[2, 44, 100, 113, 120, 121, 122] and the VC predicted group velocity is an approximation.

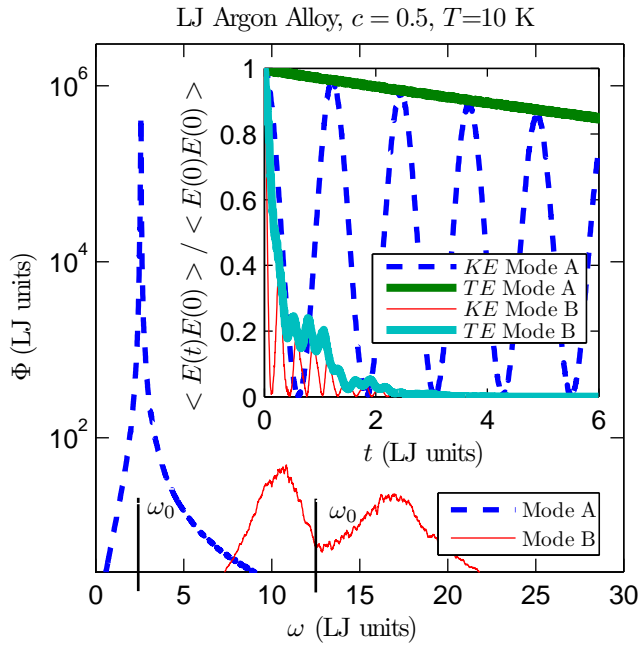


Figure 3.11: The normal mode kinetic energy,  $\Phi$ , of two modes (A and B) at wavevector [0.25 0 0] calculated using VC-NMD for a mass disordered LJ FCC supercell ( $N_0 = 8$  and  $c = 0.5$ ) is shown in the main figure. The VC dispersion-predicted peaks are labeled by  $\omega_0$ . The inset shows the same mode's energy [kinetic (KE) and total (TE)] autocorrelation functions. Note the additional oscillation effects in the KE and TE autocorrelation functions for Mode B which are due to the two peaks in  $\Phi$ . A mode lifetime can be extracted unambiguously using the integral of the TE autocorrelation function [Eq. (3.11) in Section 3.3.3.1].

August 16, 2013  
DRAFT

# Chapter 4

## Vibrational Mean Free Paths and Thermal Conductivity Accumulation Functions for Amorphous Materials

### 4.1 Introduction

The vibrational modes in disordered solids (e.g., alloys, amorphous materials) can be classified as propagons (propagating and de-localized, i.e., phonon-like), diffusons (non-propagating and de-localized), and locons (non-propagating and localized). [44, 100] Diffusons contribute to thermal conductivity by harmonic coupling with other modes due to the disorder. Locons do not contribute significantly to thermal transport in three-dimensional systems. [127]

Experimental measurements, estimates based on experiments, and modeling predictions have demonstrated that propagating modes contribute significantly to the thermal conductivity of amorphous silicon (a-Si) [7, 12, 15, 16, 45, 46, 110] and amorphous silicon nitride, [128] but not to that of amorphous silica (a-SiO<sub>2</sub>). [7, 8, 129, 130] Notably, using broadband frequency domain thermoreflectance, Regner et al. measured how the thermal conductivity of a-SiO<sub>2</sub> and a-Si thin films at a temperature of 300 K change with the penetration depth associated with the

heating laser pulse.[7] Following the suggestion of Koh and Cahill,[131] they interpret the measured thermal conductivity at a given penetration depth to be representative of the phonons with mean free path (MFP) less than that value, allowing for the construction of the thermal conductivity accumulation function.[132, 133, 134] For a-SiO<sub>2</sub>, the thermal conductivity of a 1000 nm thick film did not vary for penetration depths between 57 and 960 nm, suggesting that any propagating modes that contribute to thermal conductivity have MFPs below 57 nm. For a-Si, they find that the thermal conductivities of films with thicknesses of 500 and 2000 nm vary by 40% between penetration depths of 44 and 968 nm, suggesting that propagating modes with MFPs in this range contribute significantly to thermal conductivity.

To understand the results of Regner et al. requires knowledge of the MFPs of the propagating modes and the contribution to thermal conductivity from the non-propagating modes. Experimentally, inelastic neutron scattering can be used to measure phonon lifetimes (and from these, MFPs), but this technique is suited to single-crystal samples. [135] Traditionally, empirical expressions and simple models have been the only means to estimate MFPs in amorphous materials, [40, 90, 136, 137, 138] while the Allen Feldman (AF) theory can be used to model the non-propagating modes.[44, 45]

Predicting the vibrational MFPs in an amorphous solid requires the group velocities and lifetimes of the low-frequency propagating modes. [12, 15, 16, 45, 46, 90, 129, 130, 137] It is typically assumed that the group velocity of these modes is equal to the sound speed.[12, 40, 45, 46, 90, 129, 136, 137, 138] To evaluate the expressions and models for the low-frequency mode lifetimes requires knowledge of how the lifetimes scale with frequency. [12, 15, 16, 45, 46, 90, 129, 130, 137, 139, 140] The scaling for a-SiO<sub>2</sub> has only recently been measured, with evidence of  $\omega^{-2}$ ,  $\omega^{-4}$ , and a second  $\omega^{-2}$  regime as the mode frequency,  $\omega$ , increases from 3.14 to  $6.28 \times 10^{12}$  rads/s. [141, 142, 143, 144] For a-Si, the scaling is not well understood, [12, 15, 16, 45, 46, 110, 139, 140] with temperature-dependent[15, 139, 145] and film thickness-varying measurements [10, 11, 12, 13, 14, 15, 16, 139, 146] suggesting both  $\omega^{-2}$  and  $\omega^{-4}$  scalings. [45, 46]

The objective of this work is to investigate the propagating and non-propagating contributions to the thermal conductivity of a-SiO<sub>2</sub> and a-Si by predicting the MFPs and thermal conductivity accumulation functions for realistic models and compare to experimental measurements. [7, 8, 9, 12, 15, 16, 40, 90, 129, 130, 137, 147] The paper is organized as follows. The theoretical formulation and modeling framework are discussed in Section 4.2. The sample preparation for the a-SiO<sub>2</sub> and a-Si bulk models and the computational details are discussed in Section 4.3. In Sections 4.4.1, 4.4.2, and 4.4.3, harmonic lattice dynamics calculations are performed to predict the vibrational density of states, the plane-wave character of the vibrational modes, and the group velocity of the low-frequency propagating modes (i.e., the sound speed). The vibrational mode lifetimes are predicted using the molecular dynamics-based normal mode decomposition (NMD) method in Section 4.4.4. Using the sound speeds and lifetimes, the vibrational mode diffusivities (i.e., the product of the square of the group velocity and the lifetime) are calculated and compared with predictions from the AF theory in Section 4.4.5. Using this comparison, a cutoff frequency between propagating and non-propagating modes is specified.

The properties of the propagating and non-propagating modes are then used to predict the total thermal conductivity in Section 4.5.1. We also predict the total thermal conductivity using the Green-Kubo method and molecular dynamics simulations (a top-down approach). The thermal conductivity accumulation functions are predicted in Section 4.5.2 where the results are compared with the measurements of Regner et al.[7] and thermal conductivity experiments on thin films.[8, 9, 12, 15, 16, 40, 90, 129, 130, 137, 147]

## 4.2 Theoretical Formulation of Vibrational Thermal Conductivity

We calculate the total vibrational thermal conductivity,  $k_{vib}$ , of an amorphous solid from

$$k_{vib} = k_{pr} + k_{AF}, \quad (4.1)$$

where  $k_{pr}$  is the contribution from propagating modes [19, 52, 81] and  $k_{AF}$  is the contribution from non-propagating modes predicted by the AF theory.[45] Mode-level properties obtained from molecular dynamics (MD) simulations and lattice dynamics calculations will be used as inputs. Equation (4.1) has been used in previous studies of amorphous materials, [12, 15, 16, 45, 46, 90, 129, 130, 137] leading to predictions that while  $k_{pr}$  is a negligible fraction of  $k_{vib}$  for a-SiO<sub>2</sub> (< 10%), [90, 129, 130, 137] it is non-negligible for a-Si (20 – 80%). [12, 15, 16, 45, 46, 110]

The propagating contribution is modeled as [45, 46]

$$k_{pr} = \frac{1}{V} \int_0^{\omega_{cut}} DOS(\omega) C(\omega) D_{pr}(\omega) d\omega, \quad (4.2)$$

where  $V$  is the system volume,  $\omega_{cut}$  is the maximum frequency of propagating modes,  $DOS(\omega)$  is the vibrational density of states (DOS),  $C(\omega)$  is the mode specific heat, and  $D_{pr}(\omega)$  is the mode diffusivity. When using mode properties obtained from calculations on finite-sized systems, it is common to write Eq. (4.2) as a summation over the available modes. [45, 46] We choose the integral form because the required use of finite-sized simulation cells limits the lowest frequency modes that can be accessed. An extrapolation must be made to the zero frequency limit that is more easily handled with the integral. [12, 15, 16, 45, 46, 129, 130] Equation (4.2) is obtained by using the single-mode relaxation time approximation to solve the Boltzmann transport equation for a phonon gas. [19] In the derivation of Eq. (4.2), the system is assumed to be isotropic (valid

for an amorphous material) and have a single polarization, making the mode properties only a function of frequency. The choice of a single polarization (i.e., an averaging of the transverse and longitudinal branches) does not significantly change the results predicted in this work or that of others. [12, 15, 16, 45, 46, 130] We will evaluate Eq. (4.2) under the Debye approximation, which assumes isotropic and linear dispersion such that the DOS is

$$DOS(\omega) = \frac{3\pi\omega^2}{2v_s^3}, \quad (4.3)$$

where  $v_s$  is an appropriate sound speed.[81]

The specific heat in the classical, harmonic limit is  $k_B$ , where  $k_B$  is the Boltzmann constant. [85] Taking this classical limit allows for a direct comparison between the lattice dynamics-based predictions and those from the classical MD simulations. The harmonic approximation has been found to be valid for systems ranging from Lennard-Jones (LJ) argon,[66] to crystalline Stillinger-Weber silicon and carbon nanotubes[116] at temperatures below half the melting temperature. The full quantum expression for the specific heat is [19]

$$C(\omega) = k_B \left[ \frac{\hbar\omega/2k_B T}{\sinh(\hbar\omega/2k_B T)} \right]^2, \quad (4.4)$$

where  $\hbar$  is the Planck constant.[81] The quantum specific heat will be used for the non-propagating modes to compare the  $k_{AF}$  predictions to experimental measurements in Sections 4.5.1 and 4.5.2.

The diffusivity of the propagating modes is

$$D_{pr}(\omega) = \frac{1}{3}v_s^2\tau(\omega), \quad (4.5)$$

where  $\tau(\omega)$  is the frequency-dependent mode lifetime.[19] An equivalent physical picture in

terms of a scattering length is

$$D_{pr}(\omega) = \frac{1}{3}v_s\Lambda(\omega), \quad (4.6)$$

where  $\Lambda(\omega)$  is the MFP, defined as

$$\Lambda(\omega) = v_s\tau(\omega). \quad (4.7)$$

The lifetimes will be modeled using

$$\tau(\omega) = B\omega^{-n}. \quad (4.8)$$

By using a constant sound speed, the lifetime and diffusivity frequency scalings will be the same. For amorphous materials, the scaling exponent  $n$  has been found experimentally and numerically to be between two and four. [2, 15, 16, 45, 46, 110, 120, 121, 141, 142, 143, 144, 148, 149, 150, 151, 152, 153, 154, 155, 156, 157, 158, 159, 160, 161, 162, 163] A value of two corresponds to Umklapp scattering,[63] while a value of four corresponds to Rayleigh scattering from point defects.[30] Combined with Eq. (4.3), choosing  $n \leq 2$  ensures that the thermal conductivity evaluated from Eq. (4.2) is finite. Choosing  $n > 2$  causes the thermal conductivity to diverge, which can be fixed using additional anharmonic [45, 46] or boundary scattering terms. [12, 15, 16]

The AF diffuson contribution to thermal conductivity is [45, 46]

$$k_{AF} = \frac{1}{V} \sum_{i, \omega_i > \omega_{cut}} C(\omega_i) D_{AF}(\omega_i), \quad (4.9)$$

where  $\omega_i$  is the frequency of the  $i$ th diffuson mode,  $C(\omega_i)$  is the diffuson specific heat, and  $D_{AF}(\omega_i)$  is the diffuson diffusivity. Equation (4.9) is written as a sum because there are enough

high-frequency diffusons in the finite-size systems studied here to ensure a converged value.[45, 46] The AF diffusivities are calculated from[44]

$$D_{AF}(\omega_i) = \frac{\pi V^2}{\hbar^2 \omega_i^2} \sum_{j \neq i} |S_{ij}|^2 \delta(\omega_i - \omega_j), \quad (4.10)$$

where  $\delta$  is the Dirac delta function.[164] The heat current operator  $S_{ij}$ , which measures the thermal coupling between vibrational modes  $i$  and  $j$  based on their frequencies and spatial overlap of eigenvectors, can be calculated from harmonic lattice dynamics theory. [44, 45, 46] For Eq. (4.10),  $S_{ij}$  is directionally averaged because amorphous materials are isotropic.

## 4.3 Calculation Details

### 4.3.1 Sample Preparation

The three smallest a-SiO<sub>2</sub> samples are the same as those used in Ref. 4 and contain 288, 576, and 972 atoms at a density of 2350 kg/m<sup>3</sup>. The atomic interactions are modeled using the modified Beest-Kramer-van Santen (BKS) potential [165, 166] from Ref. 4, except that the 24-6 LJ potential[167] is changed to a 12-6, which has a negligible effect on the predictions. The LJ potentials use a cutoff of 8.5 Å and the Buckingham potentials use a cutoff of 10 Å. The electrostatic interactions are handled using the Wolf direct summation method with a damping parameter of 0.223 Å<sup>-1</sup> and a cutoff of 12 Å.[168] Larger systems of 2880, 4608, and 34562 atoms were created by tiling the smaller samples, melting at a temperature of 10000 K, and quenching instantaneously to a temperature of 300 K at constant volume. The melt-quench procedure and subsequent MD simulations were performed using the MD package LAMMPS and a time step of 0.905 fs.[87] The resulting a-SiO<sub>2</sub> structure is built from a network of rigidly-bonded SiO<sub>4</sub> tetrahedral sub-units that are weakly bonded via shared oxygen atoms, as shown in Fig. 4.1 (a). The 34562 atom sample has a supercell side length of 8.05 nm.

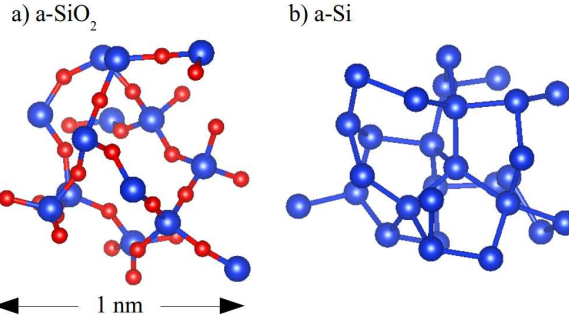


Figure 4.1: (a) Small sample of a-SiO<sub>2</sub> created from a melt-quench technique showing the Si-O tetrahedral bond network. Bond lengths range between 1.6 and 1.8 Å. (b) Small sample of a-Si created by the modified WWW algorithm. Bond lengths range between 2.3 and 2.7 Å. Visualizations using the VESTA package.[1]

For a-Si, we use samples with 216, 1000, 4096, and 100000 atoms generated from the modified Wooten-Winer-Weaire (WWW) algorithm from Ref. 169. The resulting a-Si structure is a rigid, predominantly tetrahedrally-bonded network[169] and is shown in Fig. 4.1 (b). A larger sample was created from the 100,000 atom sample, which is the largest to our knowledge, by tiling it twice in all directions to create an 800,000 atom sample with a side length of 24.81 nm. All a-Si structures have a density of 2330 kg/m<sup>3</sup>, equivalent to the perfect crystal with a lattice constant of 5.43 Å. The Stillinger-Weber (SW) potential is used to model the atomic interactions.[6] The MD simulations are performed using LAMMPS with a time step of 0.5 fs.

Amorphous materials may have many different atomic configurations with nearly equivalent potential energies, leading to potential metastability during MD simulations. [46, 110, 170, 171, 172] This meta-stability can cause errors when predicting vibrational lifetimes using NMD (see Section 4.4.4). To remove metastability, all a-SiO<sub>2</sub> and a-Si samples were annealed at a temperature of 1100 K for 10 ns.[46, 110] The removal of meta-stability is demonstrated by a decrease and plateau of the sample's potential energy during the annealing.

### 4.3.2 Simulation Details

Before data collection, all MD simulations are first equilibrated in an *NVT* (constant number of atoms, volume, and temperature) ensemble for  $10^6$  time steps at a temperature of 300 K. Data are then collected from simulations in the *NVE* (constant number of atoms, volume, and total energy) ensemble for  $2^{21}$  time steps, where the atomic trajectories are sampled every  $2^8$  time steps. Ten MD simulations with different initial conditions are run and the predictions are ensemble-averaged.

The Green-Kubo (GK) method is used to predict a top-down thermal conductivity  $k_{GK}$  [i.e., without using Eq. (4.1)] [85] using the first-avalanche method to specify the converged value of the integral of the heat current autocorrelation function (Section 4.5.1). [173] For system sizes of 4,608 (a-SiO<sub>2</sub>, supercell side length of 4.026 nm) and 4,096 (a-Si, supercell side length of 4.344 nm) atoms, the trajectories from the MD simulations are also used to predict the vibrational mode lifetimes using the NMD method (Section 4.4.4).

For an amorphous supercell, the only allowed wave vector is the Gamma point (i.e.,  $\kappa = 0$ ), where  $\kappa$  is the wavevector and there are  $3N_a$  polarization branches labeled by  $\nu$ , where  $N_a$  is the number of atoms. Calculation of the vibrational modes at the Gamma point requires the eigenvalue solution of a dynamical matrix of size  $(3N_a)^2$  that scales as  $[(3N_a)^2]^3$ , limiting the system sizes that can be considered to 4,608 (a-SiO<sub>2</sub>) and 4,096 (a-Si) atoms. The eigenvalue solution is also required to predict the vibrational DOS (Section 4.4.1) and structure factors (Section 4.4.2), and to perform the NMD calculations (Section 4.4.4) and the AF calculations (Section 4.4.5). The frequencies and eigenvectors were computed using harmonic lattice dynamics calculations with GULP.[86] The calculation of the AF thermal diffusivities [Eq. (4.10)] is performed using GULP and a Lorentzian broadening of  $14\delta\omega_{avg}$  for a-SiO<sub>2</sub> and  $5\delta\omega_{avg}$  for a-Si, where  $\delta\omega_{avg}$  is the average mode frequency spacing [ $\delta\omega_{avg} = 1.8 \times 10^{10}$  rads/s (a-SiO<sub>2</sub>) and  $1.0 \times 10^{10}$  rads/s (a-Si)]. [45, 46] Varying the broadening by 10% around these values does not change  $k_{AF}$  within its uncertainty (see Section 4.5.1).

## 4.4 Vibrational Mode Properties

### 4.4.1 Density of States

The vibrational DOS is computed from

$$DOS(\omega) = \sum_i \delta(\omega_i - \omega), \quad (4.11)$$

where a unit step function of width  $100\delta\omega_{avg}$  is used to broaden  $\delta(\omega_i - \omega)$ . The results for a-SiO<sub>2</sub> and a-Si are plotted in Fig. 4.2. The DOS for a-Si is similar to that of crystalline silicon, [100, 111] with peaks at mid- and high-frequencies. The DOS for a-SiO<sub>2</sub> is constant over most of the frequency-range, with a gap that separates the high-frequency Si-O interactions.[4] There is a clear  $\omega^{-2}$  scaling for both a-Si and a-SiO<sub>2</sub> at the lowest frequencies. The onset of this scaling occurs at a higher frequency for a-Si ( $\sim 1.5 \times 10^{13}$  rads/s) than a-SiO<sub>2</sub> ( $\sim 4.5 \times 10^{12}$  rads/s). This low-frequency scaling is predicted by the Debye model [Eq. (4.3)] and suggests that these modes may be propagating (i.e., phonon-like).

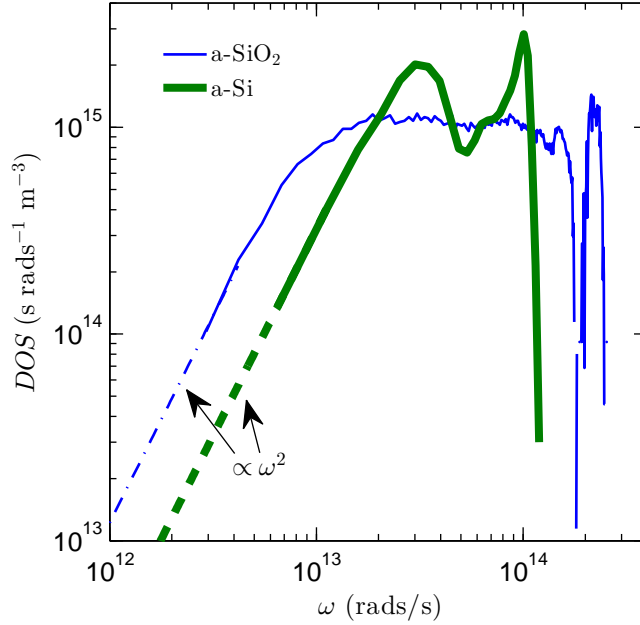


Figure 4.2: Vibrational DOS of a-SiO<sub>2</sub> and a-Si plotted on a log-log scale. Both models show an  $\omega^{-2}$  scaling at low frequency. The DOS for a-Si has two peaks similar to the DOS of the crystalline phase.[3] The DOS for a-SiO<sub>2</sub> is flat over most of the spectrum, with a high frequency gap that separates the Si-O interactions.[4]

#### 4.4.2 Structure Factor

Calculating the structure factors of the supercell Gamma modes is a method to test for their propagating (i.e., plane-wave) character at a particular wavevector and polarization. This approach has been previously used to predict effective dispersion curves of disordered and amorphous materials experimentally [115, 130, 142, 144, 149, 152, 153, 174, 175, 176] and numerically. [2, 45, 46, 100, 113, 114, 150, 151, 154, 156, 159, 160, 162, 177, 178, 179, 180, 181] The structure factor at a wavevector  $\kappa$  is defined as[100]

$$S^{L,T}(\kappa) = \sum_{\nu} E^{L,T}(\kappa_{\nu}) \delta(\omega - \omega(\kappa_{\nu}=\mathbf{0})), \quad (4.12)$$

where the summation is over the Gamma modes,  $E^T$  refers to the transverse polarization and is defined as

$$E^L(\kappa_\nu) = \left| \sum_b \hat{\kappa} \cdot e(\kappa_\nu^0 \alpha^b) \exp[i\kappa \cdot \mathbf{r}_0(l=0)] \right|^2 \quad (4.13)$$

and  $E^L$  refers to the longitudinal polarization and is defined as

$$E^T(\kappa_\nu) = \left| \sum_b \hat{\kappa} \times e(\kappa_\nu^0 \alpha^b) \exp[i\kappa \cdot \mathbf{r}_0(l=0)] \right|^2. \quad (4.14)$$

In Eqs. (4.13) and (4.14), the  $b$  summations are over the atoms in the disordered supercell,  $\mathbf{r}_0(l=0)$  refers to the equilibrium atomic position of atom  $b$ ,  $l$  labels the unit cells ( $l = 0$  for the supercell),  $\alpha$  labels the Cartesian coordinates, and  $\hat{\kappa}$  is a unit vector. The vibrational mode shape is contained in the  $3N_a$  components of its eigenvector,  $e(\kappa_\nu^0 \alpha^b)$ . [52]

The transverse and longitudinal structure factors are plotted in Figs. 4.3(a) and 4.3(b) for a-SiO<sub>2</sub> and a-Si for wavevectors along the [100] direction of the supercells. Because amorphous structures are isotropic, the structure factors are direction-independent. Mode frequencies [ $\omega_0(\kappa)$ ] and linewidths [ $\Gamma(\kappa)$ ] can be predicted by fitting each structure factor peak to a Lorentzian function of the form

$$S^{L,T}(\omega) = \frac{C_0(\kappa)}{[\omega_0(\kappa) - \omega]^2 + \Gamma^2(\kappa)}, \quad (4.15)$$

where  $C_0(\kappa)$  is a constant related to the DOS. [113] A dispersion relation is identified by plotting the  $\omega_0(\kappa)$  values in the middle panels of Figs. 4.3(a) and 4.3(b), where the error bars indicate the linewidths. For a-Si, Lorentzian fits to the structure factor peaks have coefficients of determination[182] greater than 0.8 for  $|\kappa|/\kappa_{max} \leq 0.75$  and less than 0.7 for  $|\kappa|/\kappa_{max} > 0.75$ , where  $\kappa_{max} = 2\pi/a$  and  $a$  is the lattice constant of crystalline silicon (5.43 Å).[6] For a-SiO<sub>2</sub>, the coefficients of determination are greater than 0.8 for  $|\kappa|/\kappa_{max} \leq 0.2$  and less than 0.7 for larger wavevectors, where the structure factors peaks are less than an order of magnitude larger

than the background. To evaluate  $\kappa_{max}$  for a-SiO<sub>2</sub>, we use a lattice constant of 4.8 Å, which corresponds to the *a*-direction of quartz.[5]

For a-Si, the extracted dispersion is nearly linear at small wavevectors with a slight decrease in slope at the largest values. [45, 46] For a-SiO<sub>2</sub>, the dispersion is concave-down for the smallest wavevectors considered, transitioning to a strong concave-up dispersion at intermediate wavevectors. For the intermediate wavevectors, the longitudinal dispersion for a-SiO<sub>2</sub> is well-described by the so-called “dispersion law for diffusons,” where  $\omega \propto \kappa^2$ . [113] This large concave-up dispersion has been observed in experimental measurements and numerical models of amorphous materials [2, 130, 154, 156, 175] including a-SiO<sub>2</sub>.[2, 130, 154, 175] We note that at frequencies lower than 10<sup>12</sup> rads/s, experimental measurements of a-SiO<sub>2</sub> recover a linear dispersion. [130, 142, 144, 153, 175] This frequency range is not accessible with the models studied in this work.

The atomic structures of a-SiO<sub>2</sub> and a-Si play an important role in determining the differences in the low-frequency mode properties. The weakly-bonded network of tetrahedra in a-SiO<sub>2</sub> [4, 165, 166, 167] results in a Debye scaling of the DOS that occurs at a lower frequency than in a-Si (Fig. 4.2), which is a network of strongly-bonded tetrahedra. [6, 100, 169, 177] The lower-frequency onset of the Debye-scaling of the DOS for a-SiO<sub>2</sub> leads to the strong non-linear dispersion seen in Fig. 4.3(a). The behavior of the DOS and structure factors demonstrate a clear difference in the properties of the low-frequency modes for our models of a-SiO<sub>2</sub> and a-Si, which is investigated in the following sections.

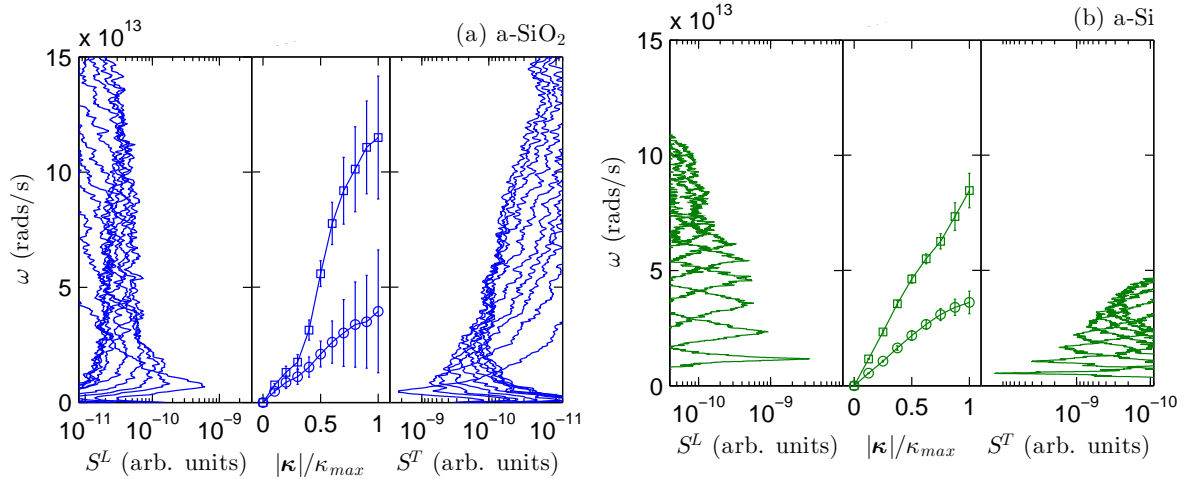


Figure 4.3: Longitudinal (left panel) and transverse (right panel) structure factors [Eq. (4.12)] for (a) a-SiO<sub>2</sub> and (b) a-Si. The wavevectors are normalized by  $\kappa_{max} = 2\pi/a$ , where  $a$  is 4.8 (a-SiO<sub>2</sub>) and 5.43 Å, based on the lattice constants of the crystalline phases. [5, 6]

#### 4.4.3 Sound Speed

For a disordered solid, except for the transverse and longitudinal sound speeds, there is not an accepted method to predict the group velocity of individual vibrational modes. While the structure factor gives the frequency spectrum needed to construct a propagating state with pure wavevector  $\kappa$ , the individual mode spectra  $E^T(\kappa)$  and  $E^L(\kappa)$  predict the plane-wave character of each mode. [100, 177] It is not generally possible to assign a unique wavevector to individual modes, even at low frequency, [100, 177] which makes predicting their group velocities challenging. While attempts have been made to predict individual mode group velocities, [18, 108, 110, 111, 112, 117] there is no theoretical basis for the proposed methods.

We now use the DOS and structure factors predicted in Sections 4.4.1 and 4.4.2 to predict the group velocities of the low-frequency modes for a-SiO<sub>2</sub> and a-Si (i.e., the sound speeds). By fitting the DOS from Fig. 4.2 to Eq. (4.3), a sound speed is obtained and is reported in Table 4.1. Because the DOS is a mixture of transverse and longitudinal modes, only a single sound speed can be predicted. Both longitudinal and transverse sound speeds can be predicted from the

structure factor peaks by forward differencing the dispersion relation as

$$v_s = \frac{\omega_0(\kappa_{min})}{\kappa_{min}}, \quad (4.16)$$

where  $\kappa_{min}$  is  $0.1\kappa_{max}$  for a-SiO<sub>2</sub> and  $0.125\kappa_{max}$  for a-Si. The results are provided in Table 4.1.

The transverse and longitudinal sound speeds of a material can also be predicted from the material's bulk ( $G$ ) and shear ( $K$ ) moduli from[86]

$$v_{s,T} = \left( \frac{G}{\rho} \right)^{1/2} \quad (4.17)$$

and

$$v_{s,L} = \left[ \frac{4G + 3K}{3\rho} \right]^{1/2}. \quad (4.18)$$

Using the bulk and shear moduli defined in terms of the elastic constants according to the Voight convention,[86] the corresponding sound speeds are reported in Table 4.1.

The longitudinal and transverse sound speeds for a-SiO<sub>2</sub> predicted using the moduli are 10-20% lower than predictions made using a linear fit to the peaks of the current correlation function for a model with 8016 atoms using the BKS potential [3568 m/s (transverse) and 5937 m/s (longitudinal)]. [154] The smaller values predicted by the structure factors and DOS result from the concave-down dispersion seen at low wavevector (i.e., we are not able to reach the linear portion of the dispersion curve).[154] Experimental measurements of the sound speeds of a-SiO<sub>2</sub> using Brillouin light and inelastic x-ray scattering range between 3800 to 4000 m/s (transverse) and 6000 to 6400 m/s (longitudinal). [149, 153, 175, 183, 184] Differences between our predictions and experimental measurements may be related to limitations of the BKS potential.

The effect of the concave-down dispersion is less pronounced for a-Si than for a-SiO<sub>2</sub>, where the sound speeds predicted by all three methods are within five percent of each other. Our sound speed predictions for a-Si using all three methods are within 10% of predictions made using the elastic moduli [185, 186] and structure factor[156] from models created by the original

WWW algorithm. [187] The 4096 atom model created by the modified WWW algorithm [169] predicted a longitudinal sounds speed of 7670 m/s from the structure factor, [159] within 5% of our prediction. In an attempt to explain the anomalously high longitudinal sound speed (8300 m/s) and thermal conductivity measurements in Ref. 15, three 1000 atom a-Si models relaxed using a tight-binding electron structure method predicted an average of 4740 m/s (transverse) and 7830 m/s (longitudinal).[15] By annealing our structures to remove metastability, the sound speeds predicted by the elastic moduli are increased, but not by the amount reported in Ref. 15. Experimental transverse sound speeds measurements using Rayleigh wave scattering are 3420 and 4290 m/s for sputtered and ion-bombarded a-Si thin films,[188] which is within 15% of the predictions from our models. It is clear that the experimentally-measured sound speeds for a-Si show a wide range.

The sound speed  $v_{s,DOS}$  will be used for both a-SiO<sub>2</sub> and a-Si for the rest of this work, allowing for the use of a single polarization for the propagating contribution [Eq. (4.2)]. By comparing the sound speeds in Table 4.1, it is clear that the low-frequency DOS of our models for a-Si and a-SiO<sub>2</sub> are dominated by transverse modes, which is expected due to their degeneracy and lower frequencies compared to the longitudinal modes. The transverse sound speed predicted for our model of a-SiO<sub>2</sub> is 85% of that predicted by the other methods (Table 4.1) and that measured by experiment. [149, 153, 175, 183, 184] While using a smaller transverse sound speed leads to an underprediction of the mode diffusivities [Eq. (4.5)], it leads to an overprediction of the DOS [Eq. (4.3)]. Holding all other input parameters in Eq. (4.1) constant, a smaller sound speed leads to a larger  $k_{pr}$  because the DOS scales as  $1/v_s^3$ . We can thus regard our  $k_{pr}$  prediction as an upper bound.

Table 4.1: Longitudinal and transverse sound speeds in m/s estimated from the elastic moduli [Eqs. (4.17) and (4.18)], structure factors [Eq. (4.16)], and DOS [Eq. (4.3)]. The pre-annealed group velocities predicted by the elastic constants are labeled as Moduli\*.

Method	Moduli*	Moduli	$S^T, S^L$	DOS
<hr/>				
a-SiO <sub>2</sub>				
Transverse	2,541	3,161	2,732	2,528
Longitudinal	4,761	5,100	4,779	
<hr/>				
a-Si				
Transverse	3,670	3,886	3,699	3,615
Longitudinal	7,840	8,271	8,047	

#### 4.4.4 Lifetimes

We now predict the lifetimes of all vibrational modes in our models of a-SiO<sub>2</sub> and a-Si using the MD simulation-based NMD method, [17, 65, 66, 71, 110, 112, 116] which explicitly includes the disorder in the supercell. [18, 105, 110, 117, 180] In NMD, the atomic trajectories from an MD simulation are first mapped onto the vibrational mode coordinate time derivatives, [52]

$$\dot{q}(\kappa=0; t) = \sum_{\alpha, b, l}^{3, n, N} \sqrt{\frac{m_b}{N}} \dot{u}_\alpha(b; t) e^*(\kappa=0)_\alpha^b \exp[i(\mathbf{0} \cdot \mathbf{r}_0(l)]. \quad (4.19)$$

Here,  $m_b$  is the mass of the  $b_{th}$  atom in the supercell,  $\dot{u}_\alpha$  is the  $\alpha$ -component of the atomic velocity, and  $t$  is time. Because the supercells of a-SiO<sub>2</sub> and a-Si are disordered, the NMD method can only be performed at the Gamma point ( $\kappa = 0$ ). The spectral energy of each vibrational mode,  $\Phi(\nu, \omega)$ , is calculated from

$$\Phi(\nu, \omega) = \lim_{\tau_0 \rightarrow \infty} \frac{1}{2\tau_0} \left| \frac{1}{\sqrt{2\pi}} \int_0^{\tau_0} \dot{q}(\kappa=0; t) \exp(-i\omega t) dt \right|^2. \quad (4.20)$$

We choose the frequency-domain representation of the normal mode energy because we find it to be less sensitive to metastability of the amorphous structure than the time-domain representation.

The vibrational mode frequency and lifetime are predicted by fitting each mode's spectral

energy to a Lorentzian function,

$$\Phi(\nu, \omega) = \frac{C_0(\nu)}{[\omega_0(\nu) - \omega]^2 + \Gamma^2(\nu)}, \quad (4.21)$$

where the constant  $C_0(\nu)$  is related to the average energy of each mode. This expression is valid when the linewidth  $\Gamma(\nu) \ll \omega_0(\nu)$ .[116] The mode lifetime is[17, 65]

$$\tau(\nu) = \frac{1}{2\Gamma(\nu)}. \quad (4.22)$$

The NMD-predicted lifetimes are plotted in Figs. 4.4(a) and 4.4(b) for a-SiO<sub>2</sub> and a-Si. Also plotted are the timescales extracted from the structure factor linewidths,  $1/[2\Gamma(\kappa)]$  (Section 4.4.2). For a-SiO<sub>2</sub>, the NMD lifetimes are larger than the Ioffe-Regel (IR) limit  $\tau = 2\pi/\omega$ , [2] and are bounded by this limit at low frequencies. There is no clear evidence for an  $\omega^{-2}$  scaling, which would correspond to propagating modes. At mid-frequencies, the NMD lifetimes are approximately constant and there is a peak near  $2 \times 10^{14}$  rads/s, which corresponds to the peak in the DOS (see Fig. 4.2). The lifetimes predicted from the structure factor fall below the NMD-predicted lifetimes and the IR limit. These low values result because the structure factor for a-SiO<sub>2</sub> is evaluated for wavevectors where the resulting wavepackets are formed by non-propagating modes. [45, 46, 100]

For a-Si, the NMD lifetimes show a clear  $\omega^{-2}$  scaling at low frequency. The lifetimes plateau at higher frequencies, over a wider range of frequencies than for a-SiO<sub>2</sub>, with two peaks corresponding to the peaks in the DOS (see Fig. 4.2). A similar plateau of lifetimes at high frequencies has been reported for disordered lattices [105, 122, 180] and other studies of a-Si.[110] The transition from the low-frequency scaling to the plateau region occurs near  $10^{13}$  rads/s, which corresponds to where the DOS first peaks in Fig. 4.2. Similar behavior has been observed for models of disordered lattices. [180] The lifetimes predicted by the structure factors are in good agreement with those predicted by NMD at low frequencies. Similar agreement has been re-

ported in other models of amorphous materials. [46, 189, 190, 191] The agreement between the NMD-predicted lifetimes and the structure factor timescales for a-Si at low frequencies indicates that these modes are plane-wave-like and that the wavepackets formed by these modes are propagating. [45, 46, 100]

The NMD-predicted lifetimes for a-Si range from 0.5 to 10 ps and are similar in magnitude to those predicted for previous WWW-generated models of a-Si. [190, 191, 192, 193] We note that one previous study of a-Si modeled using the Tersoff potential predicted vibrational lifetimes on the order of 100 ps, an order of magnitude larger than the values reported here and in previous studies. [190, 191, 192, 193] It is unclear what the source of this discrepancy is, although in Ref. 110 the NMD analysis was performed in the time domain, where the effects of metastability can be more strongly pronounced. Using the Tersoff potential on the WWW a-Si models in this work, we predict similar lifetimes to those from the SW potential.

#### 4.4.5 Diffusivities

Using the sound speeds predicted from the DOS (Table 4.1), the NMD-predicted lifetimes for a-SiO<sub>2</sub> and a-Si are used to predict the mode diffusivities with Eq. (4.5). The results are plotted in Figs. 4.5(a) and 4.5(b). We note that the sound speed is most appropriate for the lowest-frequency modes, where the DOS scales as  $\omega^2$  (Fig. 4.2). The AF theory is also used to predict the mode diffusivities and the results are also plotted in Figs. 4.5(a) and 4.5(b).

For a-SiO<sub>2</sub>, the mode diffusivities predicted by NMD and AF agree well over the majority of the frequency range. The AF diffusivities at the highest frequencies show a sharp decrease, which is an indication that these modes are localized.[45] The low- and mid-frequency diffusivities and are above the high-scatter limit,

$$D_{HS} = \frac{1}{3}v_s a, \quad (4.23)$$

which assumes that all vibrational modes travel with the sound speed and scatter over a distance of the lattice constant. [40] In evaluating Eq. (4.23), we use the lattice constant of the crystalline

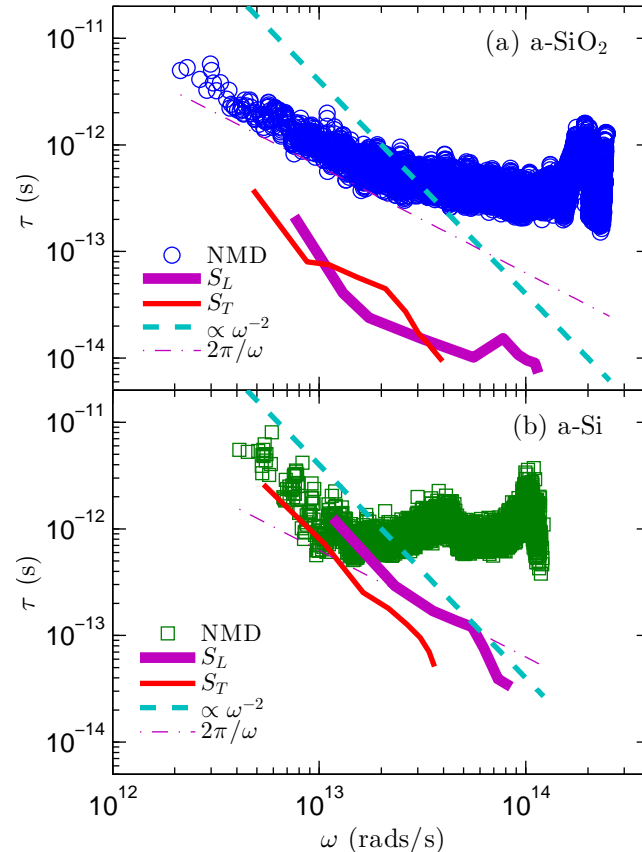


Figure 4.4: Vibrational mode lifetimes predicted by NMD [Eq. (4.22)] and the structure factors [Eq. (4.15)] for (a) a-SiO<sub>2</sub> and (b) a-Si. The NMD-predicted lifetimes are larger than the IR limit. The lifetimes predicted from the structure factors fall below the IR limit at high-frequency for a-Si and for all frequencies for a-SiO<sub>2</sub>. For a-Si, a clear  $\omega^{-2}$  scaling is observed at low frequencies, while the lifetimes plateau at higher frequencies, over a wider range of frequencies than for a-SiO<sub>2</sub>, with two peaks corresponding to the peaks in the DOS (Fig. 4.2). The transition from the low-frequency scaling to the plateau region for a-Si occurs near  $10^{13}$  rads/s, which corresponds to where the DOS first peaks in Fig. 4.2.

phases (see Section 4.4.2). The low-frequency NMD diffusivities do not show a definitive scaling. Based on the results in Ref. 130, we choose a propagating/non-propagating cutoff frequency of  $4.55 \times 10^{12}$  rads/s, which is at the onset of the Debye scaling of the DOS (Fig. 4.2). The constant  $B$  in Eq. (4.8) for  $n = 2$  is then fit to the AF-predicted diffusivities for frequencies below the cutoff by dividing the diffusivities by  $v_{s,DOS}$ . The fit value is  $B = 2.95 \times 10^{13} \text{ s}^{-2}$ .

For a-Si, the mode diffusivities predicted by NMD at low frequencies show a clear  $\omega^{-2}$  scaling. The NMD-predicted diffusivities are larger and show less scatter than those predicted by the AF theory, which is due to the finite-size system and the broadening that is required to evaluate Eq. (4.10).[45] By using a larger broadening ( $100\delta\omega_{avg}$ ), the scatter in the AF-predicted diffusivities at low frequency can be smoothed, but at the cost of decreasing the diffusivities at intermediate and high frequencies, which affects the predicted diffuson contribution to thermal conductivity (see Section 4.5.1). It is possible that a frequency-dependent broadening may be necessary for a-Si and the AF theory, but determining this dependence is not necessary for interpreting our results. For a-Si, the NMD- and AF-predicted diffusivities diverge near a frequency of  $10^{13}$  rads/s. The NMD-predicted diffusivities are relatively constant above this frequency, indicating that the sound speed is no longer an applicable scaling. The AF diffusivities are larger than the high-scatter limit [Eq. (4.23)], except for the highest frequency modes, which are localized. [45]

For a-Si, we choose  $\omega_{cut}$  and  $B$  so that Eq. (4.5) is equal to the average AF-predicted diffusivity at the cutoff frequency. The resulting values are  $\omega_{cut} = 1.16 \times 10^{13}$  rads/s (which is at the onset of the Debye scaling of the DOS, Fig. 4.2) and  $B = 2.76 \times 10^{14} \text{ s}^{-2}$ . This choice allows Eq. (4.5) to pass reasonably well through both the AF- and NMD-predicted diffusivities.

While experiments on a-SiO<sub>2</sub> show that there is a cross-over region for the low-frequency lifetime scaling from  $\omega^{-2}$  to  $\omega^{-4}$ ,[141] and back to  $\omega^{-2}$ , [141, 142, 143, 144] our present model is not large enough to investigate the mode properties in this cross-over region. Because experiments are limited for a-Si thin films, [140] we also consider a  $\omega^{-4}$  scaling for Eq. (4.8). Because this scaling is not clear from the data in Fig. 4.5(b), we use a cutoff frequency of  $1.52 \times 10^{13}$

rads/s (which is at the onset of the Debye scaling of the DOS, Fig. 4.2) based on Refs. 45 and 12 and choose  $B = 2.07 \times 10^{40} \text{ s}^{-4}$  so that Eq. (4.5) is equal to the average AF-predicted diffusivity at the cutoff frequency.

Both a-SiO<sub>2</sub> and a-Si have a region at higher frequencies where the AF-predicted mode diffusivities are relatively constant. This behavior has been reported for model disordered systems such as disordered lattices[113, 122, 180] and jammed systems. [120, 121] While diffusons are non-propagating modes whose MFPs are not well-defined,[45] a diffuson MFP can be calculated from

$$\Lambda_{AF}(\omega_i) = [3D_{AF}(\omega_i)\tau(\omega_i)]^{1/2}, \quad (4.24)$$

where  $\tau(\omega_i)$  is the NMD-predicted lifetime for that mode. Using this definition,  $\Lambda_{AF}(\omega_i)$  for both a-SiO<sub>2</sub> and a-Si is found to vary between the crystal lattice constant ( $\sim 0.5 \text{ nm}$ ) and the supercell size ( $\sim 5 \text{ nm}$ ) for modes with frequency above the cutoff. Similar MFPs have been estimated for diffusons in a-Si in previous studies.[45, 46] For modes with frequency below the cutoff, the NMD-predicted MFPs from Eq. (4.7) range up to 16 nm (a-SiO<sub>2</sub>) and 43 nm (a-Si). This result is in contrast to the MFPs estimated in Ref. 110 for a-Si, which ranged up to 500 nm. We believe that the origin of the large MFPs in Ref. 110 is a combination of the predicted lifetimes (see Section 4.4.4) and the method used to estimate the mode group velocities.

## 4.5 Thermal Conductivity

### 4.5.1 Bulk

To predict the bulk thermal conductivity for our models of a-SiO<sub>2</sub> and a-Si, we use both Eq. (4.1) and the GK method. The GK method is computationally inexpensive compared to the NMD and AF methods so that larger system sizes can be accessed. The GK-predicted thermal

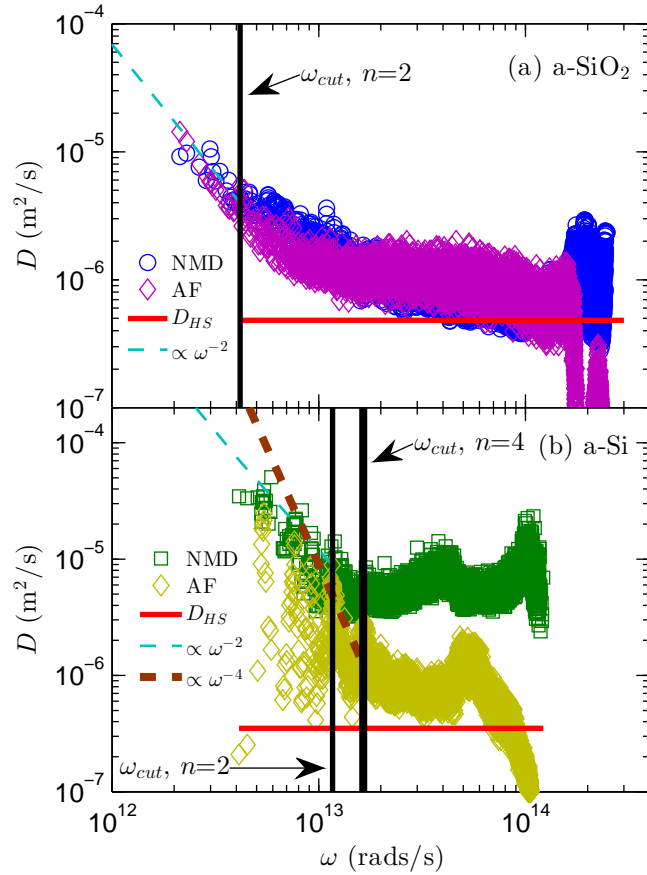


Figure 4.5: Vibrational mode diffusivities predicted from NMD [using Eqs. (4.5) and (4.22) with the DOS sound speed from Table 4.1] and the AF theory [Eq. (4.10)]. Also shown are extrapolations based on an  $\omega^{-2}$  scaling with Eqs. (4.5) and (4.8) for a-SiO<sub>2</sub> and a-Si, and an additional  $\omega^{-4}$  scaling for a-Si. For both systems, the diffusivities are larger than the high-scatter limit [Eq. (4.23)] except at high frequencies, where the modes are localized.

conductivities for a-SiO<sub>2</sub> and a-Si are plotted in Fig. 4.6 versus the inverse of the system size. For a-SiO<sub>2</sub>, there is no system-size dependence. The bulk thermal conductivity is estimated to be  $2.1 \pm 0.2$  W/m-K by averaging over all the samples. This prediction is in agreement with the GK predictions in Ref. 4 within the uncertainties, but larger than the MD-based direct-method predictions in Ref. 194. Shenogin et al. predicted the total thermal conductivity of a-SiO<sub>2</sub> using non-equilibrium MD simulations of the same small structures used in this work, finding 2.0 W/m-K for their largest system which was based on a 972 atom model tiled in one direction six times.[118] Our GK-predicted value is larger than experimental measurements, which range between 1.3 and 1.5 W/m-K, [7, 8, 9, 40] which may be due to the classical nature of the MD simulation and/or the suitability of the BKS interatomic potential for modeling thermal transport in a-SiO<sub>2</sub>. [4, 194] Quantum statistical effects are considered later in this section.

For a-Si, there is a clear system-size dependence of thermal conductivity. Because the low-frequency DOS has the form of Eq. (4.3) and the diffusivities scale as  $\omega^{-2}$ , the thermal conductivity will scale as the inverse of the system size. The bulk value can be found by extrapolating to an infinite system size. [25, 78, 116] The extrapolation is performed using the three largest system sizes,[195] leading to a bulk value of  $2.0 \pm 0.2$  W/m-K, where the uncertainty is estimated from the ensemble averaging for each system size. While it is difficult to create bulk a-Si experimentally,[188] our extrapolated bulk value is in reasonable agreement with experimental values for a wide range of thin film thicknesses (see Fig. 4.7 in Section 4.5.2).

To predict thermal conductivity from Eq. (4.1), we use the parameters  $B$  and  $\omega_{cut}$  specified in Section 4.4.5 assuming an  $\omega^{-2}$  scaling below  $\omega_{cut}$  and the AF-predicted diffusivities. For a-SiO<sub>2</sub>, the propagating, non-propagating, and total thermal conductivities are  $0.10 \pm 0.05$ ,  $1.9 \pm 0.1$ , and  $2.0 \pm 0.1$  W/m-K (see Table 4.2). The uncertainties are estimated by varying  $\omega_{cut}$  and the AF broadening by 10%. The total value agrees with the GK value within the uncertainties. For the propagating contribution using an expression similar to Eq. (4.2), Baldi et al.[130] estimated 0.1 W/m-K and Love and Anderson[129] estimated 0.03 W/m-K.

By using the  $\omega^{-2}$  diffusivity scaling for a-Si, the propagating, non-propagating, and total

thermal conductivities are  $0.6 \pm 0.2$ ,  $1.2 \pm 0.2$ , and  $1.8 \pm 0.2$  W/m-K. This value for total thermal conductivity is in agreement with the GK-predicted bulk value within the uncertainties. Earlier studies using similar models of a-Si found that  $k_{pr}$  is less than half of  $k_{vib}$ ,[45, 46] in agreement with our results. A recent study of a-Si modeled using the Tersoff potential found  $k_{pr} \approx k_{AF}$ .[110] Estimates based on experimental measurements have found  $k_{pr}$  to be as low as 20%[12, 46] and as high as 80% of  $k_{vib}$ . [15, 16]

If an  $\omega^{-4}$  lifetime scaling is assumed for a-Si, the thermal conductivity diverges at low frequency. We bound the thermal conductivity by assuming the sample to be a thin film of thickness  $t_f$  and modify the lifetimes using the Matthiessen rule,[19]

$$\frac{1}{\tau_{eff}} = \frac{1}{\tau_{bulk}} + \frac{2v_s}{t_f}. \quad (4.25)$$

Using the largest film thickness from the experimental literature ( $80 \mu\text{m}$ )[15] gives a propagating contribution to thermal conductivity of  $3.0 \pm 0.4$  W/m-K. Using the  $\omega^{-2}$  scaling and this film thickness gives a propagating contribution of 0.6 W/m-K (i.e., there is no change from the bulk value). While predictions for  $k_{pr}$  for a-Si vary based on the assumed scaling of the low-frequency vibrational lifetimes [12, 15, 16, 45, 46, 110] all evidence supports that  $k_{pr}$  is a significant fraction of the total thermal conductivity. [7, 12, 15, 16, 45, 46, 110]

In Section 4.2, we approximated the specific heat of the propagating and non-propagating modes by the classical, harmonic-limit value of  $k_B$ . At a temperature of 300 K, the quantum heat capacity [Eq. (4.4)] at the largest cutoff frequency for either a-SiO<sub>2</sub> or a-Si is  $0.98k_B$ , justifying the use of the classical specific heat in the propagating term in Eq. (4.2). For the AF contribution, however, the effect of the quantum specific heat is important. At the highest frequencies in a-SiO<sub>2</sub> and a-Si, the specific heat is  $0.073k_B$  and  $0.47k_B$ . Using Eq. (4.4) in Eq. (4.9) gives AF thermal conductivities of  $1.4 \pm 0.1$  and  $1.0 \pm 0.1$  W/m-K for a-SiO<sub>2</sub> and a-Si (Table 4.2). This correction brings the estimate of  $k_{vib}$  for a-SiO<sub>2</sub> into good agreement with experimental measurements. [7, 8, 9, 40] For a-Si, the modified  $k_{AF}$  is 20% lower than the classical-limit

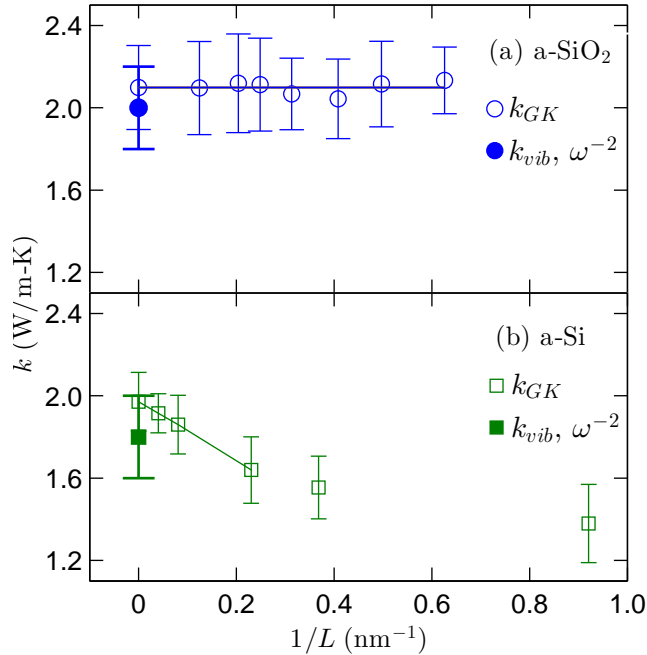


Figure 4.6: Thermal conductivities of a-SiO<sub>2</sub> and a-Si predicted using the GK method and Eq. (4.1). For a-SiO<sub>2</sub>, the GK-predicted thermal conductivity is size-independent, indicating that there is not an important contribution from propagating modes. For a-Si, there is a clear size dependence, indicating the importance of propagating modes.

value.

Table 4.2: Thermal conductivities for bulk a-SiO<sub>2</sub> and a-Si predicted by the GK method ( $k_{GK}$ ) and Eqs. (4.1) ( $k_{vib}$ ), (4.2) ( $k_{pr}$ ), and (4.9) ( $k_{AF}$ ). For the non-propagating contribution, classical and quantum specific heats are considered.

Thermal Conductivity (W/m-K)	a-SiO <sub>2</sub>	a-Si
$k_{GK}$	$2.1 \pm 0.2$	$2.0 \pm 0.2$
$k_{vib}$ (classical)	$2.0 \pm 0.1$	$1.8 \pm 0.2$
$k_{pr}$	$0.10 \pm 0.05$	$0.6 \pm 0.2$
$k_{AF}$ (classical)	$1.9 \pm 0.1$	$1.2 \pm 0.1$
$k_{AF}$ (quantum)	$1.4 \pm 0.1$	$1.0 \pm 0.1$
$k_{vib}$ (quantum)	$1.5 \pm 0.1$	$1.6 \pm 0.2$

### 4.5.2 Accumulation Function

In their broadband frequency domain thermoreflectance measurements, Regner et al.,[7] following the suggestion of Koh and Cahill,[131] interpret the measured thermal conductivity at a given penetration depth to be representative of the thermal conductivity accumulation function at a MFP equal to the penetration depth. [132, 134] Their results are plotted in Fig. 4.7(a) for a 1000 nm thick film of a-SiO<sub>2</sub> and in Fig. 4.7(b) for 500 nm and 2000 nm thick films of a-Si. The vertical coordinate of any point on the accumulation function represents the thermal conductivity that comes from phonons with MFPs less than the horizontal coordinate at that point. Also plotted in Figs. 4.7(a) and 4.7(b) are experimental measurements of thin film thermal conductivities. For a-Si, the experimental measurements are grouped broadly by sample preparation technique: (A) chemical vapor deposition [14, 15, 16] and (B) sputtering. [10, 11, 12] Application of Eq. (4.25) ignores modes that propagate in a direction that is not perpendicular to the cross-plane film direction and may have MFPs larger than the film thickness that are not included in the accumulation function. Since we consider infinite (a-SiO<sub>2</sub>) and 80  $\mu\text{m}$  (a-Si) film thickness, the effect is not important for the range of  $t_f$  and MFP shown in Figs. 4.7(a) and 4.7(b).

Based on the results in Section 4.4.5, we build thermal conductivity accumulation functions for a-SiO<sub>2</sub> and a-Si from

$$k(\Lambda^*) = k_{AF} + \frac{1}{V} \int_{\Lambda_{cut}}^{\Lambda^*} k(\Lambda) d\Lambda, \quad (4.26)$$

where  $\Lambda_{cut}$  is the MFP at the cut-off frequency,  $\Lambda^*$  is the maximum MFP considered in the thermal conductivity accumulation,  $k(\Lambda)$  is the thermal conductivity as a function of MFP, and the propagating mode MFPs are calculated using lifetimes from Eq. (4.25). The non-propagating contribution  $k_{AF}$  is evaluated using the quantum specific heat (see Section 4.5.1). The results are plotted for a-SiO<sub>2</sub> in Fig. 4.7(a) using an infinite film thickness and for a-Si in Fig. 4.7(b) using a film thickness of 80  $\mu\text{m}$ .

The predicted thermal conductivity accumulation function for a-SiO<sub>2</sub> saturates at a MFP of 10 nm, which is on the order of the finite size of our model. This result is in good quan-

titative agreement with the penetration depth-independent thermal conductivity measurements using broadband FDTR [7] and experimental measurements that show minimal film thickness dependance. [8, 9]

For a-Si, the low-MFP plateau of thermal conductivity in the measurements of Regner et al. is consistent with our predicted  $k_{AF}$ . The propagating contribution to the accumulation is predicted using  $\omega^{-2}$  and  $\omega^{-4}$  lifetime scalings, which have both been inferred from thin film experiments. [12, 15, 16, 45, 46, 139, 146] Predictions for both the  $\omega^{-2}$  and  $\omega^{-4}$  scalings pass reasonably through the experimental measurements, particularly for thermal conductivity measurements in the 50-2000 nm range. For the  $\omega^{-2}$  scaling, which best matches our model, the thermal conductivity accumulation saturates at  $1 \mu\text{m}$ , in good agreement with where the measurements of Regner et al. saturate for a 500 nm thick film, while the 2000 nm measurements show no sign of saturation. The measurements of Regner et al. show much sharper accumulations than either the  $\omega^{-2}$  or  $\omega^{-4}$  scalings, particularly for the 2000 nm measurements.

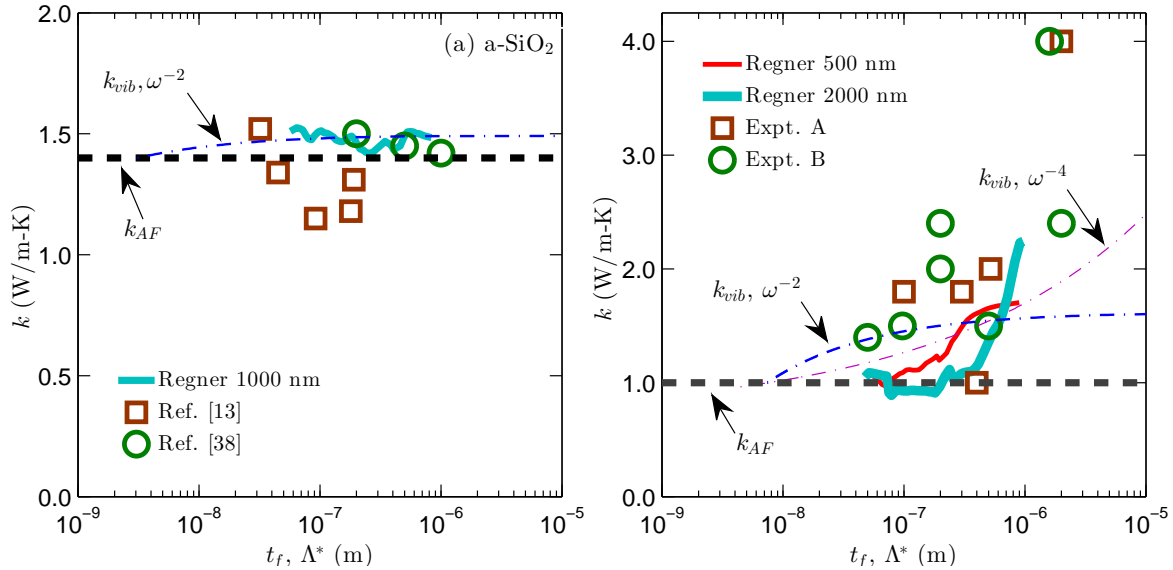


Figure 4.7: (a) Predicted thermal conductivity accumulation function [Eq. (4.26)] for a-SiO<sub>2</sub> compared with experimental broadband frequency domain reflectance measurements by Regner et al.[7] and thin film measurements from Refs. 8 and 9. The predicted thermal conductivity accumulation demonstrates that the propagating contribution is negligible in our model, which is in accord with the experimental measurements. (b) Predicted thermal conductivity accumulation function for a-Si compared with experimental measurements by Regner et al. and thin film measurements fabricated by sputtering (Expt. A) [10, 11, 12] and chemical vapor deposition (Expt. B) [13, 14, 15, 16] for a range of film thicknesses. The predicted thermal conductivity accumulation demonstrates that the propagating contribution is significant for a-Si. We note that thermal conductivities as high as 6 W/m-K (not plotted) have been measured for a-Si thin films deposited using hot-wire chemical vapor deposition.[16]

## 4.6 Summary

We investigated the contributions of propagating ( $k_{pr}$ ) and non-propagating ( $k_{AF}$ ) modes to the total vibrational thermal conductivity ( $k_{vib}$ ) of a-SiO<sub>2</sub> and a-Si using the NMD method (Section 4.4.4), AF theory (Section 4.4.5), and the GK method (Section 4.5.1). The atomic structures of a-SiO<sub>2</sub> and a-Si play an important role in determining the mode-by-mode needed to predict the propagating and non-propagating contributions. The propagating regime ends at a lower frequency for a-SiO<sub>2</sub>, which is evident from the DOS (Fig. 4.2) and the effective dispersion extracted from the structure factors [Fig. 4.3(a)]. This smaller maximum frequency of propagating modes is due, in part, to the weak bonding that exists between the SiO<sub>4</sub> tetrahedra in a-SiO<sub>2</sub>, [4, 165, 166, 167] while a-Si is formed by a network of strongly-bonded tetrahedra. [6, 100, 169, 177] The structural differences are also apparent in the low-frequency scalings of the mode lifetimes (Fig. 4.4) which show a clear  $\omega^{-2}$  dependance for a-Si, but not for a-SiO<sub>2</sub>. The combined differences of all the mode-by-mode properties results in a significant difference in the propagating ( $k_{pr}$ ) and non-propagating ( $k_{AF}$ ) contributions to thermal conductivity for a-SiO<sub>2</sub> and a-Si (Table 4.2).

For our model of a-SiO<sub>2</sub>, the contribution from propagating modes is negligible ( $\sim 6\%$ ). Our predictions align with experimental measurements of the film thickness-independence of thermal conductivity [8, 9] and penetration depth-independence in the measurements by Regner et al.[7] While the finite size of our model makes it difficult to identify a clear scaling of the low-frequency lifetime scaling, experiments show that both  $\omega^{-2}$  and  $\omega^{-4}$  scalings exist in a-SiO<sub>2</sub>.[141, 142, 144] In all cases, the propagating contribution to thermal conductivity is negligible.[8, 9, 129, 130]

For our model of bulk a-Si, the thermal conductivity has a significant ( $\sim 35\%$ ) contribution from propagating modes that are best described by a lifetime scaling of  $\omega^{-2}$ . Our predicted non-propagating thermal conductivity contribution is in good agreement with the plateau at low-MFP for all measurements of Regner et al. Our predicted thermal conductivity accumulation saturates at a value which is in agreement with the saturation for the smallest thin film measurements

by Regner et al. For all film thicknesses studied by Regner et al. the thermal conductivities accumulate much faster than our accumulations. Our bulk and thin-film thermal conductivity predictions agree with a subset of the widely-varying experimental measurements. The large range of thermal conductivity measurements on a-Si thin films suggest that a comprehensive experimental study using the recently developed thermoreflectance techniques[7, 131, 133, 196] on varying film thicknesses and preparation techniques is necessary. It may be particularly helpful to perform the experiments at temperatures less than 10 K, where the propagating contribution dominates for both a-SiO<sub>2</sub> and a-Si and the low-frequency lifetime scaling is still under debate. [12, 15, 16, 40, 45, 46, 129, 130, 137, 147]

# Chapter 5

## Conclusion (WORK)

There are two sections to this introductory chapter.

### 5.1 Contributions

#### 5.1.1 Molecular Dynamics-based Methods for Predicting Vibrational Lifetimes

Clarified the proposed spectral method.

Related it to the properly-defined dynamic structure factor.

#### 5.1.2 Thermal Transport in Alloys and High-scatter Limits

New Understanding of Physics Our manuscript provides original insight into the physics of thermal transport in disordered lattices (i.e., isotopic solids and alloys). Notably: 1. The first rigorous test of the virtual crystal (VC) approximation when used in anharmonic lattice dynamics (ALD) calculations. The VC-ALD technique has been used in a number of recent papers published in PRB and PRL (REFS), but its limits have not been assessed. In VC-ALD, the disorder in the alloy is treated as a perturbation. The perturbative disorder model was originally

developed to model isotropic solids where the disorder is weak [11]. We determined the limits of the VC-ALD approach using computationally-inexpensive empirical potentials and self-consistently treating the disorder explicitly and as a perturbation. We are not aware of any such previous study. Our results indicate that while VC-ALD is generally an accurate method for materials whose thermal conductivity is dominated by low-frequency vibrational modes, care must be taken when modeling alloys with low thermal conductivities, where significant underprediction of thermal conductivity is likely.

1. 2. The identification of important connections between the modeling of disordered lattices and amorphous materials [1,2,11,35,86]. We demonstrate that the high-scatter limit of thermal diffusivity typically used in modeling amorphous materials is directly relevant to the modeling of disordered lattices. Application of the VC approximation leads to vibrational mode diffusivities that are non-physical and the high-scatter limit provides a simple, physically-sound approach for correcting these predictions.

Scientific Interest The breakdown of the VC-ALD method has gone unnoticed in previous computational work because these studies: (i) were limited to the VC-ALD method because of computationally-expensive DFT calculations, so that validation was not possible [12,18-27], (ii) focused on materials where the thermal conductivity is dominated by low-frequency vibration modes [12,18-27], and/or (iii) did not always compare their predictions with experimental measurements [21,22,26]. In our work, we provide a self-consistent study of thermal transport in disordered lattices using a set of complementary computational tools based in molecular dynamics simulations and lattice dynamics calculations. The use of empirical potentials versus computationally-expensive DFT calculations allowed us to perform the molecular dynamics simulations that were necessary to observe the breakdown of the VC-ALD method. Our study includes two test materials that demonstrate the applicability and breakdown of the VC-ALD method. The conclusions are of general use for the study of any disordered lattice. The following calculations that we performed are novel additions to the literature: 1) Virtual Crystal + Normal Mode Decomposition. To model disordered lattices explicitly, we (and others) used normal mode decomposition (NMD) on the fully disordered supercell. This approach is limited in that the group velocity cannot be extracted so

that thermal conductivity cannot be predicted. The novel contribution of our work is the use of NMD to predict the lifetimes of a disordered lattice using VC-NMD, where the normal modes of the Virtual Crystal (VC) are used as an approximation. 2) Allen-Feldman Theory on Disordered Lattice. To model the disorder explicitly, we also use the Allen-Feldman (AF) theory of diffusons. This theory has only previously been applied to amorphous phases [16,17,35,36,74]. We use the AF theory to show that the lower-limit of diffusivity of high-frequency modes in a disordered lattice is the high-scatter limit, in contrast to the VC-ALD method, which incorrectly predicts that the limiting value is zero. Identification of this high-scatter limit of mode diffusivity was essential for identifying the breakdown in the VC-ALD method. The high-scatter limit of diffusivity is usually assumed, without theoretical justification, in models for disordered and amorphous materials [1,2,80,83]. Our study gives self-consistent justification for its use.

3) Structure Factor of Disordered Lattice to Predict Group Velocities. We calculated the structure factor for modes in a disordered lattice, which has previously only been done for modes in amorphous materials. (cite PRB articles) The structure factor predictions help us to understand that the VC-predicted group velocities are an underprediction of the representative velocity scale for mode diffusivities in the disordered lattice. While previous studies have attempted to predict the group velocity of modes in disordered systems, there is no theoretical justification for the methods used [60-62]. The structure factor provides a rigorous manner to estimate group velocities and is a significant contribution to understanding how to predict the correct velocity scale for mode diffusivities in disordered systems.[] Work Quality We present a self-consistent study of the VC approximation using five different method (VC-ALD, VC-NMD, Gamma-NMD, AF theory, and Green-Kubo). We study the thermal transport of Lennard-Jones argon in three solid phases of the materials: perfect crystal, disordered lattice, and amorphous phase. By using three phases, we demonstrate the applicability of the different methods for predicting the thermal conductivity and mode-properties: 1) Molecular Dynamics-based Green-Kubo: suitable for modeling all three phases, but does not predict the mode properties. 2) Phonon based VC-ALD and VC-NMD: suitable for the perfect crystal and disordered lattices with the high-scatter limit

correction. 3) The AF theory of diffusons: suitable for the high-frequency modes of the disordered lattice and all modes of the amorphous phase. We are unaware of any other study that uses all five of these methods self-consistently on the same material system. Our work provides clear guidelines for others on what tools are appropriate for different solid state systems. Contribution to the Literature Due to their low thermal conductivities, alloys are currently an active area of research, notably in the thermoelectric energy conversion field. The ability to predict alloy thermal conductivity is critical in narrowing down a large materials design space. Recent papers [e.g., PRL 106, 045901 (2011), PRL 109, 095901 (2012), PRB 85, 184303 (2012)] have used the VC-ALD method to make such predictions. We believe this work will make an important contribution to the literature because the high-scatter limit adjustment is of interest to the study of low-thermal conductivity alloys. Thermoelectric energy generation materials, such as PbTe/Se alloys [21,22,49], maximize their efficiency by minimizing their thermal conductivity. The search for lower thermal conductivity alloys will require the modeling of even lower-thermal conductivity alloys, where the high-scatter limit we have proposed should be considered.

### **5.1.3 Mean Free Paths of Propagating Modes in Amorphous Materials**

Draw on results and theory from the amorphous literature, which is extensive.

Present a clear modeling framework for amorphous materials, which can be used for studying a

## **5.2 Future Work**

### **5.2.1 Large Unit Cell Crystals and Disordered Materials**

ALD expensive

eigsoln as well?

MD only option?

### 5.2.2 Computing Exact Normal Modes of Large Finite Systems

Standard routines for eigenvalue solutions of the dynamical matrix can calculate the vibrational normal modes for systems with less than 8000 atoms in less than 24 hours using current computational resources.(cite) These eigenvalue solution routines typically perform on single cpus. An opportunity exists to extend the solution into the parallel cpu dimension. This can be accomplished using the Portable, Extensible Toolkit for Scientific Computation, which has routines for performing eigenvalue solutions. The PETSc pacakge has Python bindings contained in the petsc4py pacakage, which allows for easy interface with existing packages. Here is a tutorial on using the f2py package, and a general tutorial on using Python as “glue”.

The controlling Python script would work as follows... In particular, the GULP package could be compiled as a Python module using the f2py package. The dynamical matrix could then be transferred to the parallel eigenvalue solution routines contained in PETSc using petsc4py.

A previous studied investigated the vibrational normal modes which has been used in a previous study on LJ argon to compute a (cite) small subset of the normal modes for a system of 32,000 atoms [189] using the Lanczos algorithm.[197] The same 32,000 system was subsquently studied using MD simulations and the dynamic structure factor,[152] which was discussed in Section .

### 5.2.3 Predicting Timescales from very Large-Scale Molecular Dynamics Simulations

MD simulations are computationally efficient. Systems sizes of nearly  $10^6$  atoms have been studied in this work, and these were bulk systems with equal simulation side lengths in all three spatial dimensions. The spectral techniques described in Section benefit from not needing the eigenvectors of the normal modes of the simulation supercell to perform the mapping of the atomic trajectories. These methods, combined with appropriately shaped supercells, could probe the timescales of vibrational modes up to wavelengths between 24 and 100 nm using similar computational resources to those used in this work. This presents an opportunity to compare with

Table 5.1: Available packages

Package	Language	Capabilities
GULP	Fortran	mode-level (harmonic)
LAMMPS	C++	system-level, mode-level (limited)
phonopy	Python	mode-level (harmonic)

recent experimental measurements spectral linewidths in the frequency range below 1 THz which have been recently reported for a-SiO<sub>2</sub>. In the case of a-Si, these experimental measurements are lacking.[140] A unique opportunity exists to predict the spectral character at low frequency before experiment, which is rare in computational modeling.(cite)

The current correlation function, closely related to the spectral and mode decomposition methods, can even be used to study the spectral character of motions in a fluid.[198] One study showed that the effective dispersion in liquid SiO<sub>2</sub> is nearly identical to a-SiO<sub>2</sub> for low wavevectors (low-frequency).[154]

#### 5.2.4 DFT and Thermal Modeling

AF

CP2K, BigDFT

#### 5.2.5 “Wrapper“ Package for Thermal Transport Calculations

There exist numerous packages for performing calculations necessary for predicting thermal transport properties. No one package can perform all calculations necessary. In particular, no package exists to predict mode-level (bottom-up) and system-level (top-down) thermal transport properties.

LAMMPS, for example, contains most methods for predicting the system-level thermal conductivity. A package to predict the mode-level properties is needed. Ideally, the mode-level

properties could be predicted alongside the system-level calculations, as is necessary to perform the NMD and spectral techniques described in Sections and .

The Python language is an ideal environment for "gluing" together the available codes, and extending their functionality in dynamic ways.

August 16, 2013  
DRAFT

## Appendix A

# Normal Mode Decomposition Technique and Computational Details

### A.1 Derivation of Phonon Spectral Energy Density, $\Phi$ (**WORK,READ**)

To derive the correct expression for the phonon SED,  $\Phi$ , we begin with harmonic lattice dynamics theory.[50, 52] In reciprocal space, the system Hamiltonian,  $H$ , is

$$\begin{aligned} H &= \frac{1}{2} \sum_{\kappa,\nu}^{N,3n} [\dot{q}^*(\kappa; t) \dot{q}(\kappa; t) + \omega_0^2(\nu) q^*(\nu; t) q(\nu; t)] \\ &= \sum_{\kappa,\nu}^{N,3n} [T(\kappa; t) + V(\kappa; t)], \end{aligned} \tag{A.1}$$

where  $t$  is time,  $\omega_0(\kappa)$  is the frequency of the phonon mode denoted by wave vector  $\kappa$  and dispersion branch  $\nu$ , and  $N$  and  $n$  are the total number of unit cells and the number of atoms in the unit cell. The Hamiltonian is the total system energy and is the sum of the mode- and time-dependent kinetic and potential energies,  $T(\kappa; t)$  and  $V(\kappa; t)$ . The phonon normal mode coordinate,  $q(\kappa; t)$

and its time derivative,  $\dot{q}(\boldsymbol{\kappa}; t)$ , are given by

$$q(\boldsymbol{\kappa}; t) = \sum_{\alpha, b, l}^{3, n, N} \sqrt{\frac{m_b}{N}} u_\alpha(l_b; t) e^*(\boldsymbol{\kappa}_\alpha^b) \exp[i\boldsymbol{\kappa} \cdot \mathbf{r}_0(l_0)] \quad (\text{A.2})$$

and

$$\dot{q}(\boldsymbol{\kappa}; t) = \sum_{\alpha, b, l}^{3, n, N} \sqrt{\frac{m_b}{N}} \dot{u}_\alpha(l_b; t) e^*(\boldsymbol{\kappa}_\alpha^b) \exp[i\boldsymbol{\kappa} \cdot \mathbf{r}_0(l_0)], \quad (\text{A.3})$$

where  $m_b$  is the mass of the  $b^{\text{th}}$  atom in the unit cell and  $\mathbf{r}_0(l_0)$  is the equilibrium position vector of the  $l^{\text{th}}$  unit cell. The  $\alpha$ -component of the displacement from equilibrium,  $u_\alpha(l_b; t)$ , and velocity,  $\dot{u}_\alpha(l_b; t)$ , of the  $b^{\text{th}}$  atom in the  $l^{\text{th}}$  unit cell are time-dependent and are related to the phonon mode coordinates through the time-independent eigenvector that has components  $e(\boldsymbol{\kappa}_\alpha^b)$ .

The potential and kinetic energies of the normal mode are

$$V(\boldsymbol{\kappa}; t) = \frac{1}{2} \omega(\boldsymbol{\kappa})^2 q^*(\boldsymbol{\kappa}; t) q(\boldsymbol{\kappa}; t) \quad (\text{A.4})$$

and

$$T(\boldsymbol{\kappa}; t) = \frac{1}{2} \dot{q}^*(\boldsymbol{\kappa}; t) \dot{q}(\boldsymbol{\kappa}; t), \quad (\text{A.5})$$

such that the total energy of the normal mode is

$$E(\boldsymbol{\kappa}; t) = T(\boldsymbol{\kappa}; t) + V(\boldsymbol{\kappa}; t). \quad (\text{A.6})$$

In an anharmonic system, the phonon populations fluctuate about the equilibrium distribution function.[49, 50, 51] The phonon mode coordinate for the mode described by  $(\boldsymbol{\kappa}, \nu)$  and its time

derivative can be written as

$$q(\kappa; t) = q_{SS}(\kappa; t) + q_T(\kappa; t) \quad (\text{A.7})$$

and

$$\dot{q}(\kappa; t) = \dot{q}_{SS}(\kappa; t) + \dot{q}_T(\kappa; t). \quad (\text{A.8})$$

The steady-state ( $SS$ ) and transient ( $T$ ) parts and their time derivatives are given by

$$\begin{aligned} q_{SS}(\kappa; t) &= C_1(\kappa) \exp[i\omega_0(\kappa) t] \\ &\quad + C_2(\kappa) \exp[-i\omega_0(\kappa) t], \end{aligned} \quad (\text{A.9})$$

$$\begin{aligned} q_T(\kappa; t) &= \exp[-\Gamma(\kappa) |t|] \{ C_3(\kappa) \exp[i\omega_0(\kappa) t] \\ &\quad - C_4(\kappa) \exp[-i\omega_0(\kappa) t] \}, \end{aligned} \quad (\text{A.10})$$

$$\dot{q}_{SS}(\kappa; t) = i\omega_0 \{ C_1(\kappa) \exp[i\omega_0(\kappa) t] - C_2(\kappa) \exp[-i\omega_0(\kappa) t] \}, \quad (\text{A.11})$$

and

$$\begin{aligned} \dot{q}_T(\kappa; t) &= \exp[-\Gamma(\kappa) |t|] \{ C_3(\kappa) [i\omega_0(\kappa) - \Gamma(\kappa)] \exp[i\omega_0(\kappa) t] \\ &\quad - C_4(\kappa) [i\omega_0(\kappa) + \Gamma(\kappa)] \exp[-i\omega_0(\kappa) t] \}, \end{aligned} \quad (\text{A.12})$$

where the  $C$ s are constants and  $\omega_0(\kappa)$  and  $\Gamma(\kappa)$  are the phonon mode frequency and linewidth.

The transient part describes the creation of an excess in the population of a phonon mode for  $t < 0$  and its decay back to equilibrium for  $t > 0$ .

Phonon population fluctuations are commonly modeled using the excitation and decay of a single phonon mode (i.e., the single mode relaxation time approximation). In a real system,

there will be multiple phonons in each mode that simultaneously grow or decay with time. Thus, dealing only with  $\dot{q}$ , we let

$$\begin{aligned} \dot{q}(\kappa; t) = & \sum_j i \exp[-\Gamma(\nu) |t - t_j|] \times \\ & \{ A_j(\nu) [\omega_0(\nu) + i\Gamma(\nu)] \exp[i\omega_0(\nu) (t - t_j)] \\ & - B_j(\nu) [\omega_0(\nu) - i\Gamma(\nu)] \exp[-i\omega_0(\nu) (t - t_j)] \}, \end{aligned} \quad (\text{A.13})$$

where many phonons in each mode, indexed by  $j$ , are simultaneously being created and destroyed. The phonons grow for  $t < t_j$ , decay for  $t > t_j$ , and  $A_j$  and  $B_j$  are constants. We are not concerned with the values of  $t_j$ ,  $A_j$ , and  $B_j$ , though they should satisfy the long-time average  $\langle \dot{q}^*(\nu; t) \dot{q}(\nu; t) \rangle = \langle \dot{q}_{SS}^*(\nu; t) \dot{q}_{SS}(\nu; t) \rangle$ .

The expectation value of the kinetic energy of the normal mode in the time domain is

$$\langle T(\nu) \rangle = \frac{1}{2} \lim_{\tau_0 \rightarrow \infty} \frac{1}{\tau_0} \int_0^{\tau_0} \dot{q}^*(\nu; t) \dot{q}(\nu; t) dt. \quad (\text{A.14})$$

The expectation value of the kinetic energy of the normal mode can be transformed from the time domain to the frequency domain by Parseval's theorem,[83] giving

$$T(\nu; \omega) = \lim_{\tau_0 \rightarrow \infty} \frac{1}{2\tau_0} \left| \frac{1}{\sqrt{2\pi}} \int_0^{\tau_0} \dot{q}(\nu; t) \exp(-i\omega t) dt \right|^2. \quad (\text{A.15})$$

By substituting Eq. (A.13) into Eq. (A.15) and performing the time integration we find

$$\begin{aligned} T(\nu; \omega) = & \frac{1}{16\pi\tau_0} \left| \sum_j \exp[-i\omega t_j] \left\{ A_j(\nu) \frac{\omega_0(\nu) + i\Gamma(\nu)}{\omega_0(\nu) - \omega + i\Gamma(\nu)} \right. \right. \\ & \left. \left. + B_j(\nu) \frac{\omega_0(\nu) - i\Gamma(\nu)}{\omega_0(\nu) + \omega - i\Gamma(\nu)} \right\} \right|^2. \end{aligned} \quad (\text{A.16})$$

We are primarily interested in values of  $\omega$  where  $\omega \approx \omega_0$  when  $\Gamma \ll \omega_0$ . When  $\omega \approx \omega_0$ , the term involving  $A_j$  becomes large and the term involving  $B_j$  can be neglected (alternatively, we

could ignore the term involving  $A_j$  when  $\omega \approx -\omega_0$ ). Hence, we find

$$T(\boldsymbol{\nu}; \omega) = \frac{1}{16\pi\tau_0} \sum_j \sum_{j'} \cos [\omega(t_{j'} - t_j)] A_j(\boldsymbol{\nu}) A_{j'}(\boldsymbol{\nu}) \\ \times \frac{\omega_0^2(\boldsymbol{\nu}) + \Gamma^2(\boldsymbol{\nu})}{\Gamma(\boldsymbol{\nu})} \frac{\Gamma(\boldsymbol{\nu})}{[\omega_0(\boldsymbol{\nu}) - \omega]^2 + \Gamma^2(\boldsymbol{\nu})}. \quad (\text{A.17})$$

We arrive at the expression for the phonon spectral energy density for the wavevector  $\boldsymbol{\kappa}$  by summing Eq. (A.17) over the different polarizations  $\nu$ ,

$$\Phi(\boldsymbol{\kappa}, \omega) = 2 \sum_{\nu}^{3n} T(\boldsymbol{\nu}; \omega) = \sum_{\nu}^{3n} C_0(\boldsymbol{\nu}) \frac{\Gamma(\boldsymbol{\nu}) / \pi}{[\omega_0(\boldsymbol{\nu}) - \omega]^2 + \Gamma^2(\boldsymbol{\nu})}, \quad (\text{A.18})$$

where the factor of two comes from equipartition of kinetic and potential energy (valid for a harmonic classical system, see Section 2.3.3), and

$$C_0(\boldsymbol{\nu}) = \sum_j \sum_{j'} \cos [\omega(t_{j'} - t_j)] A_j(\boldsymbol{\nu}) A_{j'}(\boldsymbol{\nu}) \frac{\omega_0^2(\boldsymbol{\nu}) + \Gamma^2(\boldsymbol{\nu})}{8\tau_0\Gamma(\boldsymbol{\nu})}. \quad (\text{A.19})$$

Thus, the phonon spectral energy density  $\Phi(\boldsymbol{\kappa}, \omega)$  is a superposition of  $3n$  Lorentzian functions with centers at  $\omega_0(\boldsymbol{\nu})$  (one for each polarization) with a linewidth (half-width at half-maximum) of  $\Gamma(\boldsymbol{\nu})$ .  $\Phi$  is a spectral energy density since its integral over all wavevectors and frequencies is the total crystal energy, i.e., the Hamiltonian is

$$H = \int_{V_{BZ}} \int_0^{\infty} \Phi(\boldsymbol{\kappa}, \omega) d\omega d\boldsymbol{\kappa}, \quad (\text{A.20})$$

where  $V_{BZ}$  is the volume of the first Brillouin zone. Like the frequency broadening, there is also a broadening of the SED in wavevector. [27] For a finite sampling of the first Brillouin zone, the Hamiltonian can be approximated by

$$H \approx 2 \sum_{\boldsymbol{\kappa}, \nu}^{N, 3n} \langle T(\boldsymbol{\nu}; t) \rangle = \sum_{\boldsymbol{\kappa}}^N \int_0^{\infty} \Phi(\omega, \boldsymbol{\kappa}) d\omega. \quad (\text{A.21})$$

## A.2 Interpretation of $\Phi'$ (WORK,READ)

As demonstrated in Section 2.4.1,  $\Phi'$  is not the phonon spectral energy density,  $\Phi$ , defined by Eq. (2.3). Our findings and those of others, [73, 75, 77, 78, 79] however, suggest that  $\Phi'$  does contain accurate information about the phonon frequencies. To understand this expression, we start with the real-space atomic velocities as represented by the normal mode velocities,  $\dot{q}(\kappa'_\nu; t)$  [52],

$$\dot{u}_\alpha(l_b; t) = \sum_{\kappa'_\nu, \nu}^{N, 3n} \frac{1}{\sqrt{m_b N}} \exp[i\kappa'_\nu \cdot \mathbf{r}_0(l_b)] e^*(\kappa'_\nu \cdot \mathbf{r}_0(l_b)) \dot{q}(\kappa'_\nu; t). \quad (\text{A.22})$$

Fourier transforming both sides of Equation (A.22) in time and space, taking the complex modulus, and summing over the atoms in the unit cell and the Cartesian directions yields

$$\begin{aligned} \lim_{\tau_0 \rightarrow \infty} \frac{1}{4\pi\tau_0} \sum_\alpha^3 \sum_b^n \frac{m_b}{N} \left| \sum_l^N \int_0^{\tau_0} \dot{u}_\alpha(l_b; t) \exp[\Theta] dt \right|^2 = \\ \lim_{\tau_0 \rightarrow \infty} \frac{1}{4\pi\tau_0} \sum_\alpha^3 \sum_b^n \left| \frac{m_b^{3/2}}{\sqrt{N}} \sum_l^N \sum_{\nu}^{3n} e^*(\kappa'_\nu \cdot \mathbf{r}_0(l_b)) \int_0^{\tau_0} \dot{q}(\kappa'_\nu; t) \exp[\Theta] dt \right|^2, \end{aligned} \quad (\text{A.23})$$

where the the sum over  $\kappa'$  on the right-hand-side is reduced to a single wavevector by the orthogonality of the allowed wavevectors over the periodic domain. Equation (2.8) is the finite integration of the left-hand-side of Eq. (A.23).

Under the harmonic approximation, the phonons are non-interacting and have no transient response beyond a harmonic oscillation [see Appendix A.1, Eqs. (A.8) and (A.12)],

$$\begin{aligned} \dot{q}(\kappa_\nu; t) &= \dot{q}_{ss}(\kappa_\nu; t) \\ &= i\omega_0(\kappa_\nu) \{ C_1(\kappa_\nu) \exp[i\omega_0(\kappa_\nu) t] - C_2(\kappa_\nu) \exp[-i\omega_0(\kappa_\nu) t] \}. \end{aligned} \quad (\text{A.24})$$

Inserting Eq. (A.24) into the right hand side of Eq. (A.23) gives

$$\begin{aligned} \sum_{\alpha}^3 \sum_b^n m_b \left| \sum_l^N \int_{-\infty}^{\infty} \dot{u}_{\alpha}(b; t) \exp[i\kappa \cdot \mathbf{r}_0(l) - i\omega t] dt \right|^2 = \\ \sum_{\alpha}^3 \sum_b^n \left| \frac{m_b^{3/2}}{\sqrt{N}} \sum_l^N \sum_{\nu}^{3n} D(\kappa_{\nu}^b) \exp[i\kappa \cdot \mathbf{r}_0(l)] \delta[\omega_0(\nu) - \omega] \right|^2, \end{aligned} \quad (\text{A.25})$$

where  $D(\kappa_{\nu}^b) = i\sqrt{2\pi}\omega_0(\nu)C_1(\kappa)\exp[i\kappa \cdot \mathbf{r}_0(l)]$ ,  $\delta$  is the Dirac function, and values of  $\omega \leq 0$  are ignored. Thus, at zero temperature Eq. (2.8) is a superposition of Dirac functions at the phonon frequencies  $\omega_0(\nu)$ .

Equation (2.8) is similar to the definition of the displacement structure factor [113, 114, 154, 159, 178]

$$S_D(\kappa, \omega) = \frac{1}{4\pi\tau_0} \left| \sum_{\alpha}^3 \sum_b^n \frac{m_b}{N} \sum_l^N \int_0^{\tau_0} \dot{u}_{\alpha}(b; t) \exp[i\kappa \cdot \mathbf{r}_0(l) - i\omega t] dt \right|^2, \quad (\text{A.26})$$

which is related to the static structure factor [2, 45, 46, 100, 113, 150, 156, 160, 162, 177, 179, 180, 181] (see Sections 3.3.2 and 4.4.2). [113]. The difference between Eqs. (2.8) and (A.26) is that the summations over  $\alpha$  and  $b$  occur inside the square modulus for Eq. (A.26). With the summations inside the square modulus, the orthonormality of the mode eigenvectors can be used to show that the static and dynamic structure factors are equivalent under the harmonic approximation. [113]

## A.3 Unit Cell and Supercell Representations (WORK)

### A.3.1 Primitive and Conventional Unit Cells (WORK)

Harmonic lattice dynamics is a framework for determining the frequencies and mode shapes of a linear mass-spring system. For a periodic system, the unit cell (i.e., the basis) and lattice vectors are first specified based on the atomic structure. This specification is not unique. For example,

as shown in Table A.1, one can choose a one atom-basis and a face-centered cubic lattice (the primitive unit cell) or a four-atom basis and the simple cubic lattice (the conventional unit cell) to describe the same structure. The unit cell choice may be related to theoretical or computational complexity, but will not affect the bulk properties (e.g., heat capacity or thermal conductivity).

The choice of unit cell and supercell size determines the allowed wavevectors of a system (see Section ). The choice of unit cell, however, does not affect the allowed wavevectors, only their representation.

Let's use the LJ argon FCC crystal as an example. The system has a one atom basis with the primitive unit cell.

For supercells constructed using the conventional

In general, there may not be a mapping There exists a mapping between

The code works by recognizing that the reciprocal space for an FCC lattice is a BCC lattice.

lennard-jones FCC primitive conventional mapping

Note: this script can be run using the open-source package octave.

The selection of the unit cell sets the shape of the Brillouin zone and the points that will be resolved inside it (i.e., the allowed wave vectors,  $\kappa$ ). For a simulation cell with  $N$  atoms, there are  $3N$  normal modes. If the unit cell has one atom, there will be  $N$  allowed wave vectors, each with three polarizations (i.e., dispersion branches, which we will denote by  $\nu$ ). For a four-atom unit cell, there will be  $N/4$  allowed wave vectors, each with 12 polarizations. In general, the choice of an  $n$ -atom unit cell will lead to  $N/n$  allowed wave vectors, each with  $3n$  polarizations. As such, there are always  $3N$  normal modes.

### A.3.2 Crystal Symmetries (WORK)

Symmetry operations define a crystal. This applies to any vector or tensor property of the crystal. The symmetries do not depend on the unit cell representation, although conventional unit cells may have additional symmetries compared to the primitive unit cells which is due to the

Unit Cell	Primitive (one atom)	Conventional (four atoms)
Basis	Face-centered Cubic	Simple Cubic
Lattice Vectors	$(a/2, a/2, 0),$ $(a/2, 0, a/2),$ $(0, a/2, a/2)$	$(a, 0, 0),$ $(0, a, 0),$ $(0, 0, a)$
Brillouin Zone	Truncated Octahedron	Cube
Number of Wave Vectors	$N$	$N/4$
Polarizations/ Wave Vector	3	12

Table A.1: The unit cell for a face-centered cubic crystal can be chosen in different ways.

redundant information of using a conventional cell.

Ab initio codes such as abinit and quantum espresso also print the symmetry operations information. The spglib package contains a library of routines for utilizing the symmetry operations of.

Contact Ankit Jain for more information on symmetry operations and their application to thermal transport calculations.

For the crystalline systems studied in Section , the wavevectors are averaged over according to their symmetries, which reduces the list of wavevectors to the first octant of the cubic BZ.[28]

This reduction is equivalent to applying rotations of the SO(3) Group, or the group of 90 degree rotations in Euclidean (3-dimensional) space. Any successive combination of 90 degree rotations is also a symmetry operation. This property leads to the identity

$$\boldsymbol{\kappa} = -\boldsymbol{\kappa}, \quad (\text{A.27})$$

which is the application of two 90 degree rotations, and is a general property of any crystal.

Here is a matlab function which compares two vectors and checks if they are related by any number of orthogonal rotations.

For the LJ argon example, further reduction of the wavectors is possible by using all symmetry rotation operations of the face centered cubic lattice. Additional translational symmetry operations may exist. For example, for the cubic conventional cell of LJ argon, translational symmetries ensure that all four atoms in the unit cell are equivalent. Thus, the conventional cell has more total symmetries (rotational plus translational) than the primitive cell, which is due to the redundant information contained within it. Similar to conventional unit cells, crystalline supercells also have a larger number of translational symmetries.

### A.3.3 Primitive, Conventional, and Supercell Representations using Normal Mode Decomposition (WORK)

Having described the normal mode decomposition theoretical approach and computational methodology in Sections ?? and ??, we now carry out a case study on a LJ crystal at a dimensionless temperature of 0.0827 (corresponding to an argon temperature of 10 K). While this temperature is low (the LJ argon Debye temperature is around 85 K), it will allow for a clean demonstration of the technique. The LJ interatomic potential is computationally inexpensive and is thus ideal for use in code development and testing. All results will be presented in dimensionless LJ units

[81]. The zero pressure lattice constant is 1.556 (Ref. 28) and the potential energy is cutoff and shifted at a distance of 2.5.

From the same simulation cell and atomic data, one can perform normal mode decomposition on either the primitive or conventional unit cells. \* The [100] and [111] dispersion curves and density of states obtained from harmonic lattice dynamics calculations are plotted for each unit cell in Figs. A.1(a) and (b). While the dispersion curves in each direction show similarities, they are necessarily different due to the allowed wave vectors and shape of the Brillouin zone (see Table A.1). The density of states, however, are identical, as expected and required. We note that the conventional unit cell description leads to what appear to be optical modes. In reality, these modes are a result of zone folding and can be mapped directly to acoustic modes in the primitive unit cell description.

The MD simulations are run in the *NVE* ensemble, the dimensionless time step is 0.002, and the equations of motion are integrated using the velocity Verlet algorithm. The system is equilibrated for  $2^{20}$  time steps before collecting data every 25 time steps for an additional  $2^{20}$  time steps. In order to capture system-size effects, cubic simulation cells with between 256 and 6912 atoms are considered (corresponding to between four and twelve conventional unit cells,  $N_0$ , in each of the  $x$ ,  $y$ , and  $z$  directions). Ten simulations are performed with different initial velocities and the autocorrelations (or Fourier transforms) are averaged over the initial conditions and symmetric wave vectors before fitting the phonon properties.

The lifetimes predicted from the frequency-domain analysis for the primitive and conventional unit cell representations of the  $N_0 = 10$  system are plotted in Fig. A.2(a). The difference between the lifetimes is less than 5%, which is within the uncertainty of the fitting. A  $1/\omega^2$  scal-

\*The allowed wave vectors are defined by the basis and the supercell used to perform the MD simulations. For a supercell built using the conventional unit cell, as we use, the allowed wave vectors can be labeled using either the conventional or primitive unit cell description. For a supercell built using the primitive unit cell, however, all wave vectors cannot be labeled using the conventional unit cell description.

ing, predicted from theory for phonon-phonon scattering at low frequencies [63], is plotted and is in good agreement with the trend in the data at low frequencies. Also plotted is the Ioffe-Regel (IR) limit [2],

$$\tau_{IR} = \frac{2\pi}{\omega}, \quad (\text{A.28})$$

which corresponds to when the phonon lifetime is equal to its period. All the modes in the perfect system have lifetimes well above this limit. It is interesting to note that the phonon lifetimes do not decrease monotonically with increasing frequency, with a maximum observed near  $\omega = 18$ . Such a maximum is also observed in silicon lifetimes obtained from the SW potential [199] and from DFT calculations [25].

In performing the normal mode decomposition, one is not limited to the primitive or conventional unit cells. As needed for disordered systems (see Sections ?? and ??) one can define the simulation cell as the unit cell, such that all normal modes have  $\kappa = 0$  (i.e., they are all at the Gamma-point). <sup>†</sup> The lifetimes for Gamma-point analysis for the same MD data used to generate the lifetimes in Fig.A.2(a) are plotted in Fig.A.2(b). The trends for the Gamma-point analysis are the same as for the primitive and conventional unit cells. There is more scatter in the Gamma-point data as wave vector symmetry averaging is no longer possible.

The phonon properties obtained from normal mode decomposition and harmonic lattice dynamics calculations can now be used to predict bulk thermal conductivity using Eq.(??). For classical MD simulations the assumption of equipartition of energy is very good and we take the volumetric specific heat to be  $k_B/V$  for all modes [66, 72, 116].

The Gamma point corresponds to bulk translation and therefore does not contribute to thermal conductivity. By discretizing the Brillouin zone, we assign a volume to the Gamma point. The zero contribution of this volume to the thermal conductivity introduces a size effect in the

<sup>†</sup>In Gamma-point analysis, all normal modes have zero group velocity and it is not possible to predict mean free paths or thermal conductivity.

prediction. To predict a bulk thermal conductivity, an extrapolation procedure is used, whereby  $k$  is plotted versus  $1/N_o$  and a line is fit to the data. The point on this line where  $1/N_o = 0$  gives the bulk thermal conductivity [17, 25]. This extrapolation procedure requires that the low-frequency modes be dominated by intrinsic scattering (i.e.,  $\tau \propto \omega^{-2}$ ) and have a similar group velocity [25, 78]. For the LJcrystal, this requirement is satisfied for modest system sizes ( $N_0 \geq 6$ ). The size-dependent and extrapolated thermal conductivities are plotted in Fig.A.3 for both the primitive and conventional unit cells. The Green-Kubo predictions for the same system are also plotted and show no size effect, consistent with previous work [66].

The extrapolated thermal conductivities from the primitive and conventional unit cells are  $177 \pm 15$  and  $176 \pm 14$  W/m-K. The Green-Kubo thermal conductivity is  $173 \pm 13$  W/m-K. All thermal conductivities agree well within their respective uncertainties.

For the perfect LJ crystal, there is no clear advantage of performing the analysis in the time or frequency domains or for the primitive or conventional unit cells. Challenges may emerge for high thermal conductivity materials like silicon or carbon nanotubes, where the time-domain decay may not be well described by an exponential and the peaks in frequency space get narrow or are not well-fit by a Lorentzian. The failure of the fitting for a perfect crystal is an indication that the relaxation time approximation may not be appropriate and that care should be taken when interpreting the results. In general, new materials should be investigated on a case-by-case basis to determine the approach that minimizes the uncertainty.

## A.4 NMD using Non-Exact Normal Modes (WORK)

In Section ??, we showed how normal mode decomposition is applied to a perfect crystal. In reality, any crystal will have some deviation from perfect periodicity, which may be caused by a point defect, a dislocation, a grain boundary, or a free surface. In extreme cases, these deviations from periodicity will lead to the emergence of modified normal modes. For small perturbations,

however, it is reasonable to assume that the frequencies and mode shapes of the normal modes will be unchanged and that the effect of the perturbation will be on the lifetimes. Under this assumption, one can still project the atomic positions and velocities onto the normal modes of the unperturbed system.

While one could perform the normal mode decomposition by projecting the atomic positions and velocities onto the modes of the unperturbed system, it is more appropriate to use the virtual crystal approximation [22, 24, 26, 37]. Under the virtual crystal approximation, the system is replaced by one where all atoms have the same mass, equal to the average of the atomic masses in the system of interest. This system will have the same mode shapes as the original system, but the frequencies are modified due to the change in the average atomic mass.

Results for the time- and frequency domain approaches to normal mode decomposition are shown for two modes in Figs. A.4(a)-(d). These two modes are equivalent to those shown in the perfect crystal case study in Figs. A.1(b), 2.1(a), and 2.1(b). For a concentration,  $c$ , of 0.05, both peaks in the frequency domain are well-formed and a lifetime can be extracted by fitting the data to a Lorentzian function. This behavior is typical of all modes at a concentration of 0.05. The downward frequency shift is related to the increased average atomic mass.

For a normal mode of the lattice supercell used for the MD simulations (i.e., a Gamma mode), the total energy autocorrelation is an exponential function with a decay time  $\tau(\kappa)$  and the kinetic energy autocorrelation is a exponentially-damped sinusoidal oscillation with frequency  $2\omega(\kappa)$ .[200] When projecting MD simulations of the explicitly disordered lattice supercells onto the VC normal modes, the energy autocorrelation functions do not always follow these simple functional forms, as shown in Fig. 3.11 for two modes in the LJ alloy at a concentration of 0.5. By calculating the mode kinetic energy in the frequency-domain,  $\Phi$ ,[116] artifacts such as multiple peaks are observed (see main plot).

These artifacts are not surprising given two considerations: (i) the MD simulations contain explicit disorder that influences the atomic trajectories, and (ii) the VC-normal modes are not the exact normal modes of the explicitly-disordered lattice supercells. An effective lifetime can be

predicted using Eq. (3.11) because the VC total mode energy autocorrelations still decay to zero in a finite time. This result is to be expected given that the atomic trajectories contain information about the lattice energy, which from general statistical physics principles will have exponential relaxation behavior in an equilibrium ensemble. [49, 201, 202]

For an alloy concentration of 0.5, the lower frequency mode still has a well-formed peak. The higher-frequency mode does not, however, such that a lifetime cannot be extracted by fitting to a Lorentzian function. Such behavior is typical of the higher frequency modes at high alloy concentrations. This change in behavior is also seen in the time domain, where the decay of the autocorrelation of the total mode energy is no longer a smooth exponential function. This behavior indicates that the virtual crystal normal mode is not a good description of the true normal mode. As such, we use Eq. (??) to approximate a lifetime, as shown in Figs. A.4(c) and A.4(d).

## A.5 Effect of Metastability for Amorphous Solids on Normal Mode Decomposition (WORK)

For systems with a large degree of disorder, the normal mode analysis can always be performed by treating the simulation cell as the unit cell (i.e., Gamma-point analysis). This approach has the disadvantage of not being able to provide a phonon group velocity, such that it is not possible to predict a mean free path or thermal conductivity. That being said, the analysis still allows for an understanding of relevant time scales and assistance in the identification of non-phonon like modes. [100]

We now perform a case study on an amorphous LJ system at a dimensionless temperature of 0.0413. The amorphous solid is generated by liquifying the crystal, instantaneously removing all kinetic energy, and then relaxing the structure. The MD simulation parameters are the same

as for the crystal and alloy. One system with 2048 atoms is modeled. The LJ amorphous solid is metastable at this temperature and intermittently moves between very similar low-energy states. Evidence for the metastability can be found by analyzing the time-histories of the atomic displacements. As such, normal mode decomposition, which requires the average atomic positions, will be an approximation.

The time- and frequency-domain approaches to normal mode decomposition are shown for two mode in the amorphous system in Figs.A.5(a) and A.5(b). Because the analysis is performed at the Gamma-point, the peaks are well formed, but they are not Lorentzian, which may be due to non-plane wave behavior. We believe that the oscillations in the total energy correlation for the low frequency mode is a consequence of the metastability of the amorphous phase. As such, we extract the lifetimes by using Eq.(??), as shown in the inset to Fig.A.5(b).

The lifetimes for the amorphous system are plotted in Fig.A.6. Compared to the crystal, the lifetimes show little frequency dependence and a significant number at low frequencies fall below the Ioffe-Regel limit. Many of the normal modes in amorphous solids do not propagate and their contribution to thermal conductivity can be predicted using theory proposed by Allen and Feldman, which is based on calculating the mode diffusivity [44, 45, 110, 118]. An important direction for future work is to determine how the lifetimes from normal mode decomposition for an amorphous phase can be related to the diffusivities from Allen-Feldman theory.

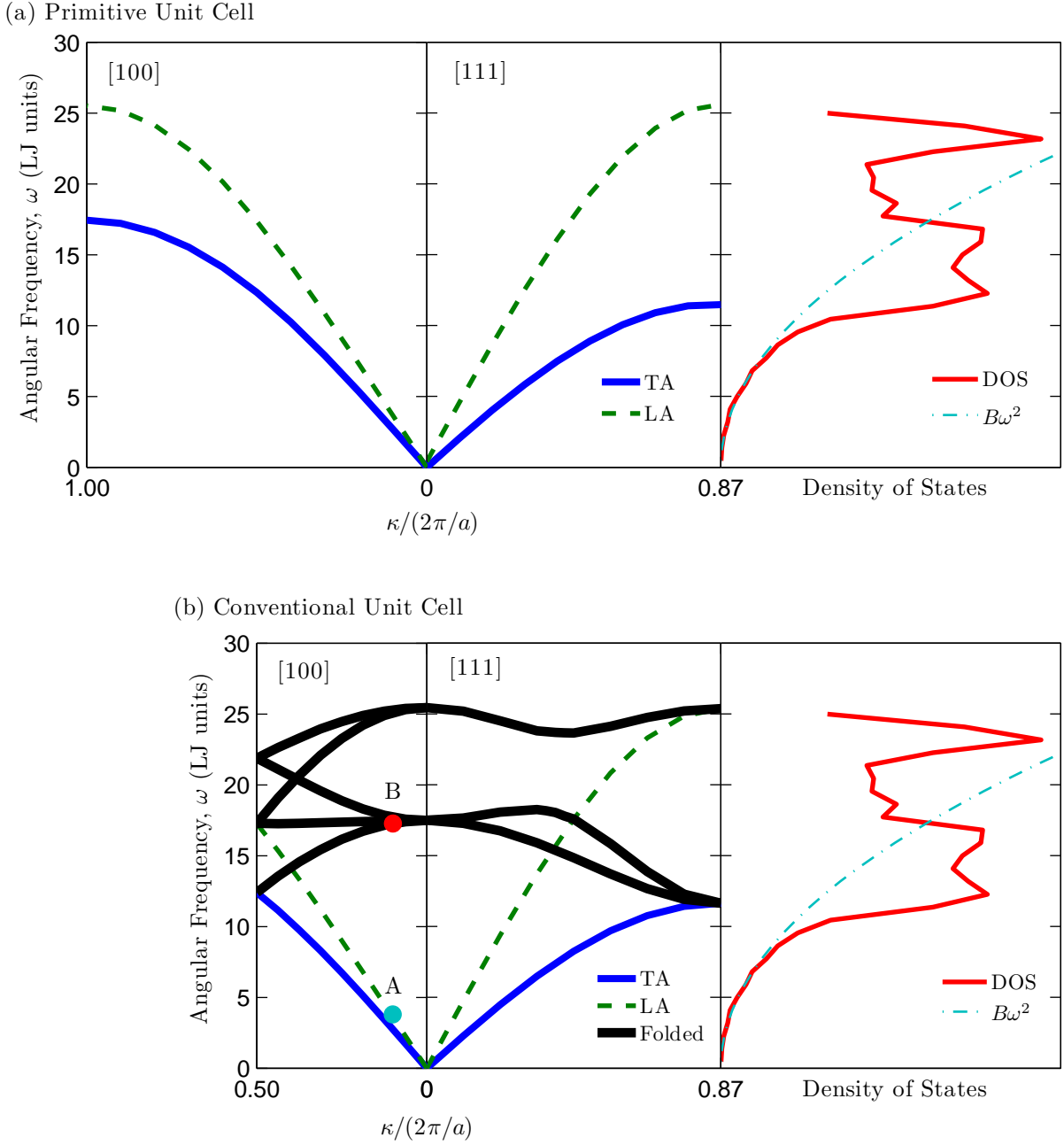


Figure A.1: Dispersion curves and full Brillouin zone density of states for a LJ crystal at a dimensionless temperature of 0.0827. (a) [100] and [111] dispersion curves and density of states based on the primitive (i.e., one atom) unit cell. (b) [100] and [111] dispersion curves and density of states based on the conventional (i.e., four atom) unit cell. The harmonic lattice dynamics calculations are performed using a resolution of sixteen wave vectors along the reciprocal lattice vectors of the conventional unit cell. The red and blue dots in (b) are the modes considered in Fig. 2.1.

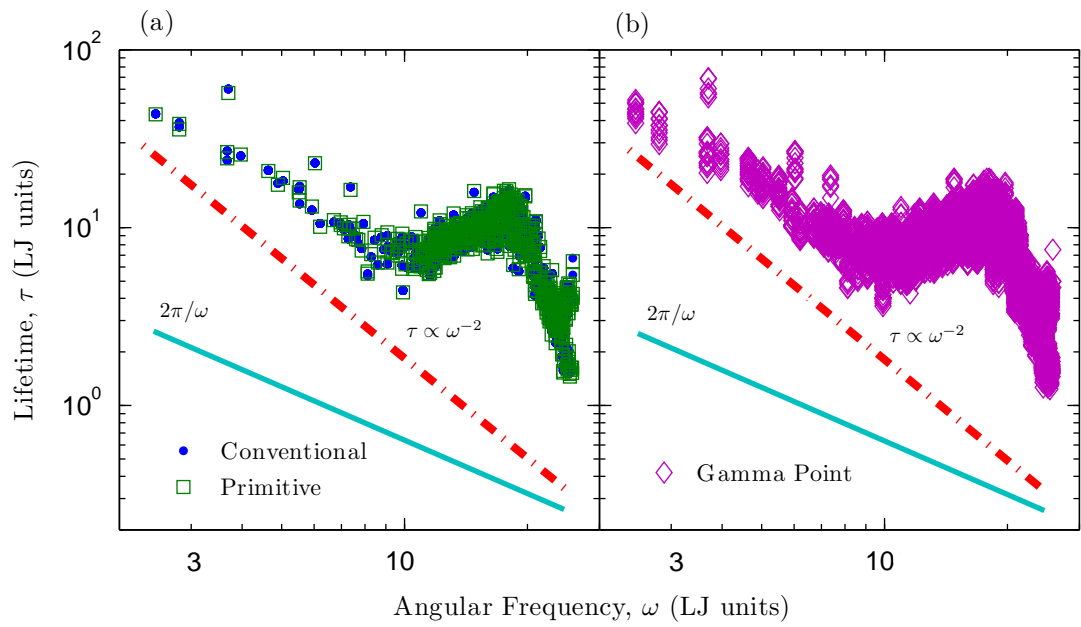


Figure A.2: Lennard-Jones lifetimes from a  $N_0 = 10$  system at a temperature of 0.0827 predicted from normal mode decomposition analysis on (a) the primitive and conventional unit cells, and (b) treating the simulation cell as the unit cell (i.e., Gamma-point analysis). All lifetimes extracted from time-domain analysis.

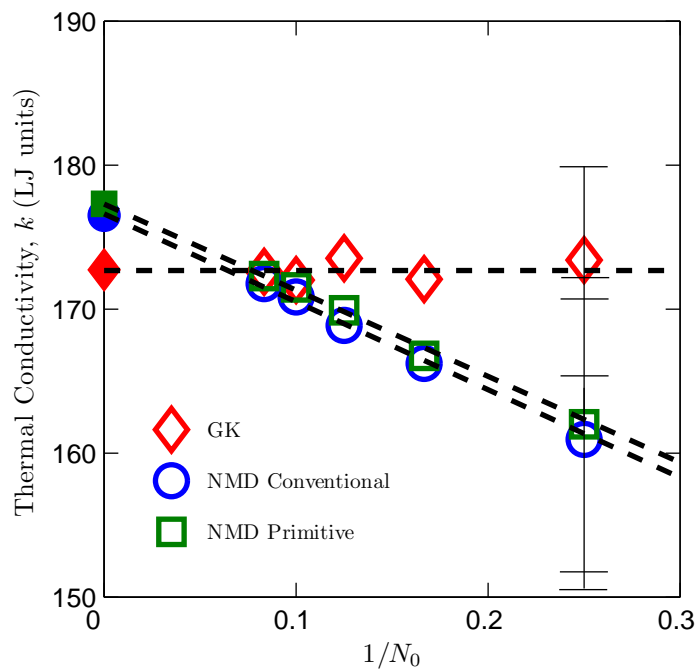


Figure A.3: Size dependence of thermal conductivity for the LJ crystal at a temperature of 0.0827 from normal mode decomposition and the Green-Kubo method.

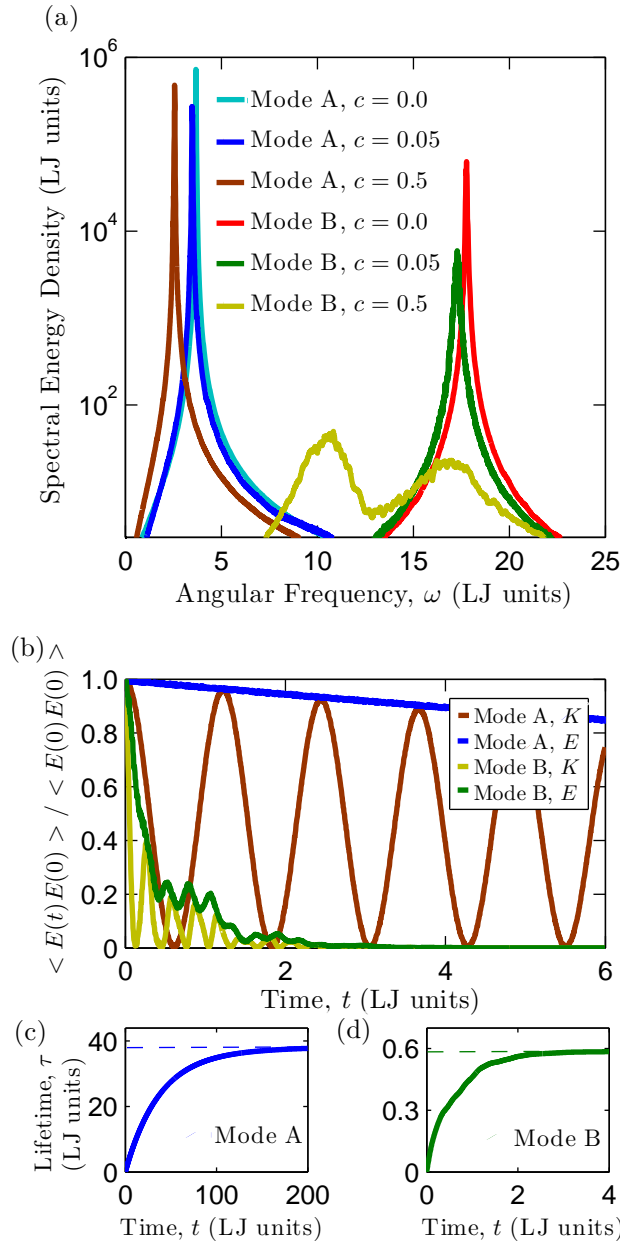


Figure A.4: Virtual crystal (a) frequency-domain and (b) time-domain normal mode decomposition analysis for two modes in LJ alloys with concentrations of 0.05 and 0.5. For modes that are not well-approximated by the virtual crystal modes, the lifetime can be approximated using Eq. (??), as shown in (d).

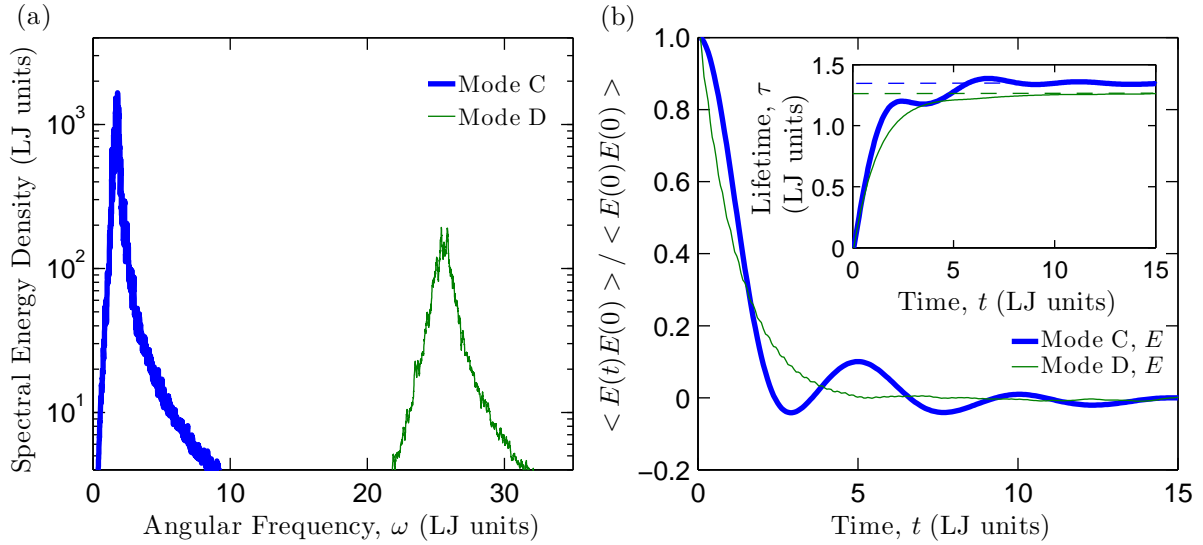


Figure A.5: (a) Time-domain and (b) frequency domain normal mode decomposition analysis for two modes in an amorphous LJ solid at a dimensionless temperature of 0.0413.

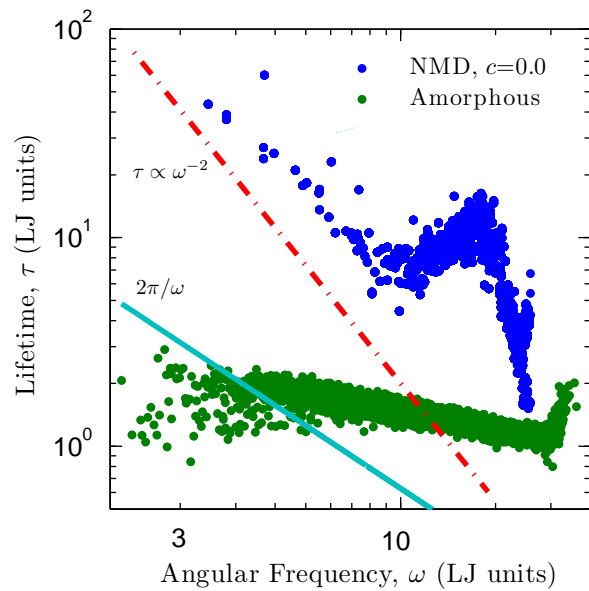


Figure A.6: Lifetimes predicted by normal mode decomposition for an amorphous LJ phase at a dimensionless temperature of 0.0413. The lifetimes for the crystal at a dimensionless temperature of 0.0827 are provided for comparison.

## A.6 Finite Simulation-Size Scaling for Thermal Conductivity (WORK)

(WORK): add discussion from vc and mfp papers.

For the LJ argon system studied in Section 2.4.1, a finite simulation-size scaling procedure [17, 18] is used to compare the thermal conductivity predictions from  $\Phi$  and  $\Phi'$  to those from the Green-Kubo method. The scaling procedure is demonstrated in Fig. A.7. The thermal conductivity is predicted from  $\Phi$  or  $\Phi'$  and MD simulations with  $N_0 = 4, 6, 8$ , and 10. The bulk conductivity,  $k_\infty$ , is then estimated by fitting the data to

$$1/k = 1/k_\infty + A/N_0, \quad (\text{A.29})$$

where  $A$  is a constant. This procedure is necessary because the first Brillouin zone is only sampled at a finite number of points for a finite simulation size, with no contribution from the volume at its center. To predict a bulk thermal conductivity, it is important to sample points near the Brillouin zone center, where the modes can have large lifetimes and group velocities.[17, 68] As with the extrapolated bulk thermal conductivities at temperatures of 5 and 20 K (see Table 3.1), the predicted thermal conductivities at each system size ( $N_0 = 4, 6, 8$ , and 10) are systematically smaller and outside the prediction uncertainties for  $\Phi'$  compared to  $\Phi$ .

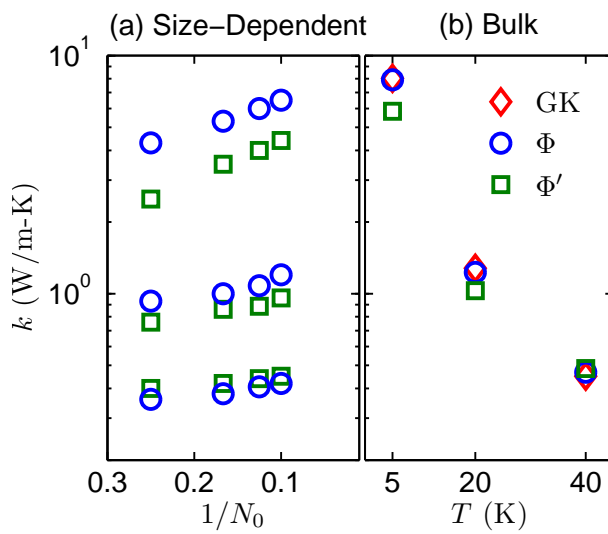


Figure A.7: Thermal conductivity predictions for LJ argon calculated using phonon lifetimes predicted by  $\Phi$  and  $\Phi'$ . (a) The finite simulation-size scaling extrapolation [17, 18] is used to compare the results to bulk predictions made using the Green-Kubo method. (b) The bulk results for  $\Phi$  and Green-Kubo are in good agreement temperatures of 20 and 40 K with those of other atomistic simulation methods,[17] while those from  $\Phi'$  differ (see Table 3.1).

August 16, 2013  
DRAFT

## Appendix B

# Research using High Performance Computing (WORK)

## B.1 Setting Up Computing Environment

### B.1.1 Hardware and Operating System Choice

The choice of hardware determines the operating system. The three main choices for operating system are Windows, Apple OS, and Linux. Each operating system has limitations depending on the hardware it operates on. For example, Apple OS is primarily used on Apple hardware.

Linux: world's most widely used software Linux runs on cell phones to the world's largest supercomputers. Recommend the most widely used linux version ubuntu. well-documented, large-community discussion Apple OS is an adequate substitute as it is unix-like.

There are many options for installing Ubuntu and the instructions can be found on <http://www.ubuntu.com/>. Ubuntu is certified on many top PC's from many computer companies and a company, system 76, builds computers with Ubuntu pre-installed. I used the Pangolin Performance for over a year of

my PhD. However, I recommend using the lightest, most-portable, and longest-battery life notebook available such as the Samsung Series 9 or Macbook Air. You will typically be using this notebook to access large computing clusters remotely, so there is a benefit of having portability and long battery life over large computational power.

### B.1.2 Linux/Unix Terminal, Commands, and Environment Variables

These instructions work best for Ubuntu operating system, and will work well for other versions of Linux. Systems commands are executed by the system terminal.

Useful Linux Commands:

sed, grep, ls, cd, pwd, export, setenv, scp -r, ssh, sudo, nohup, vi, cat, which, echo

google: linux sed

environment variable such as \$PATH. Here is how we determine what PATH is set to:

Set PATH for lammps (see Section ).

Permanent changes to environment variables can be made in the user's .bashrc file, which is typically located in the /home/user/ directory. The .bashrc file is a hidden file noted by its name starting with ". ". Other

Here is an example .bashrc which demonstrates how to add permanent paths and how to define new functions within the operating system. For example, to copy the output of the pwd command to the system's clipboard, use cpyc then "ctrl-v" elsewhere.

This file modifies environment variables such as PATH when a bash terminal session is launched. Changes to environment variables are made when a new terminal session is started. The location of this file is typically: /home/user/.bashrc. The

.bashrc from Kevin Parrish.

Shell scripts are relatively low-level sets of system commands which can manipulate environment variables (Section ) and the Linux operating system.

Here is a simple tutorial on writing shell scripts <http://linuxcommand.org/wss0010.php>

Running Linux system commands in Python can be an effective way of generating and manipulating many files with one script. Python is a more robust language than lower-level shell scripting. Here is an example:

```
lmp.in.iseed
```

### B.1.3 Working on Remote Resources

At some point during research you will need to execute code on remote resources which are typically large ( $> 100$  cpu) computing clusters. You will be provided with a terminal session similar to the session provided by Ubuntu with most of the same system commands.

While I recommend Filezilla for handling the transfer of data and files, the functionality of Filezilla is contained in several shell commands:

```
ssh user@gilgamesh.cheme.cmu.edu
```

or equivalently by the machine's ip address:

```
ssh user@xxx.xxx.xxx.xxx
```

Files can be transferred using the following command:

```
scp -r user@gilgamesh.cheme.cmu.edu:/home/user/directory/ ./
```

which will place the "directory" and its contents into the pwd (.) of the local terminal session.

There are many variants of the operating systems used for remote computing clusters, but the differences are usually superficial. During my work I used the gilgamesh computing cluster maintained by John Kitchin. Gilgamesh's documentation is a good resource for learning how to run calculations on a computing cluster.

## B.2 Installing, Writing and Executing Programs

### B.2.1 Installing Available Packages

Before writing any of your own code, it is best to utilize any useful code which may already exist. There are numerous available packages for performing calculations in fields such as genetics, computational, fluid mechanics, and (of course) thermal transport modeling (see the following Section ).

Most linux OS have automatic software installation. For Ubuntu, program management is achieved using the apt-get system command:

```
jason@jason-900X3C / (master) $ sudo apt-get install gfortran [sudo] password for jason:
Reading package lists... Done Building dependency tree Reading state information... Done
gfortran is already the newest version. The following package was automatically installed and is
no longer required: kde-l10n-engb Use 'apt-get autoremove' to remove it. 0 upgraded, 0 newly
installed, 0 to remove and 129 not upgraded.
```

To check that the package has been installed, use:

```
jason@jason-900X3C-900X3D-900X3E-900X4C-900X4D / (master) $ which gfortran /us-
r/bin/gfortran
```

This shows that gfortran program is installed in the /usr/bin/ folder, a common location where automatically installed programs are located. Because the folder /usr/bin is in the PATH environment variable:

the program gfortran is always available no matter where you are in the system terminal.

To get more information about the gfortran, use:

```
jason@jason-900X3C / (master) $ ls -l /usr/bin/gfortran lrwxrwxrwx 1 root root 12 Apr 22
03:44 /usr/bin/gfortran -> gfortran-4.7
```

where we see that /usr/bin/gfortran "points" to gfortran-4.7. This is called a symbolic link, which can be created using:

```
jason@jason-900X3C /disorder/pcbm/topotools-tutorial-part2 (master) $ ls -l /usr/bin/gfortran
lrwxrwxrwx 1 root root 12 Apr 22 03:44 /usr/bin/gfortran -> gfortran-4.7
```

## B.2.2 Available Programs and Packages for Thermal Transport Modeling

Available programs represent opportunities to perform research quickly and easily. I suggest you read their documentation carefully and try the tutorials which are typically computationally inexpensive.

Most of the packages listed below cannot be installed using Ubuntu's apt-get command, although this feature does exist for LAMMPS and more packages are likely to be added in the future. It is important to read the installation documentation carefully. It is also helpful to contact any system linux/unix system administration staff or other researchers who are experienced with installing packages. These people can usually be found at campus or local computing centers, or in your own research group!

For a first-time user, I recommend trying to install the LAMMPS package as it is one of the easiest and most versatile. It has standard installation files for systems ranging from your personal computer up to massively-parallel supercomputer.

Install lammps:

Set PATH for lammps

gnu compilers vs intel: gnu freely available tar -zvxf lammps.tar, make serial, sudo apt-get install openmpi, make openmpi

open-source:

LAMMPS, including the particularly useful mailing list (use ctrl-f to search on any topic) and python interface which is used with the package ntpy. GULP, ABINIT, Quantum Espresso, VESTA, phonopy, VMD (with topotools) ntpy, VASP DL\_POLY, siesta, GAMESS, CP2K, BOLTZTRAP, PHON,

I recommend trying this install.sh created by Kevin Parrish which installs many programs and

packages, including lammps for parallel computing with openmpi.

### B.2.3 Writing Programs

its in this section B.2.3.1

#### B.2.3.1 Coding Languages: Compiled versus Interpreted

There are many languages used for the open-source and lisenced packages(REF) that can be used to study nanoscale transport. These packages use compiled and interpreted languages and often a miture of the two.

The most commonly used compiled languages are C/C++ (linux, LAMMPS) and Fortran (GULP, quantum espresso, VASP).

A good discussion on the strengths of C++ versus Fortran.

excellent c++ tutorial

excellent fortran tutorial

The two interpreted languages you are likely to use are matlab and python.

The key to maximizing the potential of interpreted languages is by using the built-in “vector” functions and operations provided by the matlab and python programming libraries.

matlab has an excellent built-in guide, google search will typically yield useful results. A good open-source substitute for matlab is octave which is capable to running most matlab scripts.

#### B.2.3.2 Case-study(a): Compiled Language, Lennard-Jones Argon Molecular Dynamics

The first case study is a single C code to perform Molecular Dynamics on LJ argon. The code uses simple subroutines and operates using a single (serial) processor. The arrays in this code are built statically. Arrays can be created dynamically, which allows for the input of systems with varying number of atoms. Addtionally, vectors can be created and destroyed dynamically and have some advantages over arrays.

The code is compiled using the GNU project's C++ compiler, g++:

```
1 jason@jason-900X3C ~ / disorder / md_serial ( master ) $  
2 g++ ArgonMD.cpp -o ArgonMD_O_g++
```

The code can be run and the output can be directed using a useful shell operation called piping, which is demonstrated below:

```
1 jason@jason-900X3C ~ / disorder / md_serial ( master ) $  
2 ArgonMD_O_g++ > ./ArgonMD_O / output . txt
```

The code can be compiled using optimization flags, such as -O and -O3:

```
1 jason@jason-900X3C ~ / disorder / md_serial ( master ) $  
2 g++ -O3 ArgonMD.cpp -o ArgonMD_O3_g++
```

which greatly decreases the run time of this particular code. The total run time can displayed by using the shell command grep, which shows for no optimization:

```
1 jason@jason-900X3C ~ / disorder / md_serial ( master ) $  
2 grep -A 1 "Total Time" ./ArgonMD / output . txt  
3 Total Time: 38.42 ( s )
```

for -O optimization:

```
1 jason@jason-900X3C ~ / disorder / md_serial ( master ) $  
2 grep -A 1 "Total Time" ./ArgonMD_O / output . txt  
3 Total Time: 18.06 ( s )
```

and for -O3 optimization:

```
1 jason@jason-900X3C ~ / disorder / md_serial ( master ) $  
2 grep -A 1 "Total Time" ./ArgonMD_O3 / output . txt  
3 Total Time: 11.74 ( s )
```

A useful shell command is vi, a shell-based text editor, which can display the output within a shell terminal:

```
1 jason@jason-900X3C ~/disorder/md_serial (master)
2 $ vi ./ArgonMD/output.txt
3 0      1      5.61358 2.01864 5.26596
4 ...
```

To compare with the above results, the lammps code is compiled in serial using no optimization, -O, and -O3. The results are contained in folders beginning with “lmp”. A useful shell function is tab-twice, where tapping the tab key twice will display files and folders which begin with the same characters:

```
1 jason@jason-900X3C ~/disorder/md_serial (master) $
2 grep -A 1 "Loop time" ./lmp
3 lmp.in.1j~      lmp_serial/    lmp_serial_O/  lmp_serial_O3/
```

The tab key can also be used for command-line completion to complete directory and file names.

The run time for no optimization is:

```
1 jason@jason-900X3C ~/disorder/md_serial (master) $
2 grep -A 1 "Loop time" ./lmp_serial/log.lammps
3 Loop time of 0.718188 on 1 procs for 1000 steps with 256 atoms
4
5 ---
6 Loop time of 3.4892 on 1 procs for 5000 steps with 256 atoms
```

for -O optimization:

```
1 jason@jason-900X3C ~/disorder/md_serial (master) $
2 grep -A 1 "Loop time" ./lmp_serial_O/log.lammps
3 Loop time of 0.19842 on 1 procs for 1000 steps with 256 atoms
```

```
4  
5 ---  
6 Loop time of 0.917175 on 1 procs for 5000 steps with 256 atoms
```

and for -O3 optimization:

```
1 jason@jason-900X3C ~/disorder/md_serial (master) $  
2 grep -A 1 "Loop time" ./lmp_serial_O3/log.lammps  
3 Loop time of 0.164066 on 1 procs for 1000 steps with 256 atoms  
4  
5 ---  
6 Loop time of 0.786311 on 1 procs for 5000 steps with 256 atoms
```

The decrease in run time with increasing optimization for lammps is roughly the same as for my code. However, for every optimization the lammps code is approximately an order of magnitude faster. This is due to several factors, the most important being the implementation of neighbor lists as discussed in the lammps documentation. The interested reader is encouraged to investigate the lammps code further for useful C++ coding practices.

### B.2.3.3 Compiled versus Interpreted Case-study(b): Lennard-Jones Dispersion

With interpreted languages traditional programming practice of using loops (for/do/while, etc) will slow the code down.

Matlab version using mixture of loops and vectorized functions.

Fortran version (GULP)

### B.2.3.4 Compiled versus Interpreted Case-study(c): Allen-Feldman Diffusivity Calculation

Two systems, my local laptop:

<http://www.samsung.com/us/computer/series-9-notebooks>

```
1 jason@jason-900X3C ~/disorder (master) $$$$ cat /proc/cpuinfo
2 processor : 0
3 vendor_id : GenuineIntel
4 cpu family : 6
5 model    : 58
6 model name : Intel(R) Core(TM) i5-3317U CPU @ 1.70GHz
7 stepping : 9
8 microcode : 0x17
9 cpu MHz   : 782.000
10 cache size : 3072 KB
11 physical id : 0
12 siblings   : 4
13 core id    : 0
14 cpu cores  : 2
15 apicid     : 0
16 initial apicid : 0
```

gilgamesh

```
1 jason@gilgamesh > cat /proc/cpuinfo
2 processor : 0
3 vendor_id : AuthenticAMD
4 cpu family : 16
5 model    : 9
6 model name : AMD Opteron(tm) Processor 6128 HE
7 stepping : 1
8 cpu MHz   : 2000.003
```

```

9 cache size    : 512 KB
10 physical id : 1
11 siblings     : 8
12 core id     : 0
13 cpu cores   : 8
14 apicid      : 16

```

## B.2.4 Executing Programs

### B.2.4.1 Executing Locally: Rapid Development

### B.2.4.2 Executing Remotely: Portable Batch Systems

### B.2.4.3 Scaling Calculations

The majority of the methods used in this work scale poorly with the number of atoms,  $N_a^\alpha$  with  $\alpha > 1$ .

Let's take the scaling cost  $N_a^3$ , which is the scaling for eigenvalue solution used in Sections . The cost of performing this calculation for a large system size  $N_{a,large}$  and every successive system which is half the size of the former is given by the geometric series with common ratio  $r = 1/8$

$$cost_{total} = N_{a,large} \frac{1}{1 - r} = 1.143 N_{a,large} \quad (\text{B.1})$$

It costs a minimal amount ( $\approx 14\%$ ) to study systems smaller than the largest system considered. Even a linear scaling  $N_a$  has  $cost_{total} = 2N_{a,large}$ . Because of this I recommend picking the system of maximum size and then start calculations with the smallest system of interest. Publication drafts can be developed much faster by performing computationally cheap calculations

first, documenting the results, and then iterating to more computationally expensive calculations. This scheme for performing calculations can follow these time-scales for calculation costs: one second, minute, hour, day, and week. I have performed countless calculations costing around one second, and very few which cost more than one week. Publication quality results will typically cost between one hour and one week.

## B.3 Preparing Journal Articles and Thesis

recommendation: student advisor should try and exchange editing a written research document at least every week. The exchange of such a document

Such a research document could be the running collection of journal articles which turn into the thesis. Maintenance of this document can be achieved with Dropbox or Github. Github offers to advantage of smart version control and a built-in wiki.

### B.3.1 Journal Articles

The job of the student is to prepare, submit, and publish peer-reviewed journal articles. There are many journals suitable for nanoscale transport topics. All of them accept Latex prepared manuscripts. I recommend the Latex editor Kile, while the simple gedit works well and comes pre-installed with Ubuntu. Here is a simple latex example and how to generate a portable document format (PDF) from the latex document.

To maintain the reference library I recommend zotero. Here is an example reference.bib file which is exported automatically by zotero. The references are generated from the latex document using bibtex which compiles the contents of the reference.bib.

Here is an example of the latex files used to create an article published from this work:  
Predicting alloy properties.

This file uses revtex, which is an article class used by Physical Review, Journal of Applied

Physics, and others.

### B.3.2 Thesis

These can be used as templates

Here is a Carnegie Mellon thesis template:

<https://github.com/robsimmons/cmu-thesis>

J. Larkin thesis files.

Article on structuring large documents.

### B.3.3 Producing Figures

Python has a plotting module, matplotlib, which has many examples. Here is a simple example demonstrating how to generate and save data, load that data, and plot.

Here is a simple example demonstrating how to

## B.4 Technical Advice

In addition to your advisor and close mentors, I recommend communicating with experts in the field as much as possible without being annoying. How often to communicate depends on the situation. It is best to let the expert dictate the pace of the conversation.

### B.4.1 Expert Advice

Here is a list of experts I used as resources for this work. They will typically answer emails within 24-48 hours:

Alan McGaughey, Jon Malen, Julian Gale (GULP author), Keivan Esfarjani, normand.mousseau@umontreal.ca, guido.raos@polimi.it, Joseph Feldman, Junchiyo Shiomi, Davide Donadio, Craig Maloney, Jivtesh

Garg, John Duda, Wissam Al-Saidi, Dan Sellan, Ankit Jain, Wee-Liat Ong, John Kitchin, Steve Plimpton via the LAMMPS mailing list Axel Kolhmeyer via the LAMMPS mailing list and email

Atz Togo, creator of phonopy

me

## B.4.2 Online Resources

wikipedia

sklogwiki

we can do better, needs to be organization.

<http://nanohub.org/>

does not provide good HPC resources.

# Bibliography

- [1] Koichi Momma and Fujio Izumi. VESTA: a three-dimensional visualization system for electronic and structural analysis. *Journal of Applied Crystallography*, 41(3):653658, June 2008. (document), 3.1, 3.2, 4.1
- [2] S. N. Taraskin and S. R. Elliott. Determination of the ioffe-regel limit for vibrational excitations in disordered materials. *Philosophical Magazine Part B*, 79(11-12):17471754, 1999. (document), 3.3.3.1, 3.5, 3.6, 4.2, 4.4.2, 4.4.2, 4.4.4, A.2, A.3.3
- [3] E. S. Landry and A. J. H. McGaughey. Effect of film thickness on the thermal resistance of confined semiconductor thin films. *Journal of Applied Physics*, 107:013521, 2010. (document), 2.1, 4.2
- [4] A. J. H. McGaughey and M. Kaviany. Thermal conductivity decomposition and analysis using molecular dynamics simulations. part II. complex silica structures. *International Journal of Heat and Mass Transfer*, 47:17991816, 2004. (document), 4.3.1, 4.4.1, 4.2, 4.4.2, 4.5.1, 4.6
- [5] Ralph Walter Graystone Wyckoff and RWG Wyckoff. *Crystal structures*, volume 1. Interscience publishers New York, 1963. (document), 4.4.2, 4.3
- [6] F. H. Stillinger and T. A. Weber. Computer simulation of local order in condensed phases of silicon. *Physical Review B*, 31:52625271, 1985. (document), 1.1.2, 2.1, 2.4.2, 3.1, 3.3.3.2, 4.3.1, 4.4.2, 4.3, 4.6



*Transfer*, 45(12):2439–2447, 2002. (document), 4.1, 4.5.2, 4.7

- [15] Xiao Liu, J. L. Feldman, D. G. Cahill, R. S. Crandall, N. Bernstein, D. M. Photiadis, M. J. Mehl, and D. A. Papaconstantopoulos. High thermal conductivity of a hydrogenated amorphous silicon film. *Phys. Rev. Lett.*, 102(3):035901, January 2009. (document), 4.1, 4.2, 4.2, 4.2, 4.4.3, 4.5.1, 4.5.1, 4.5.2, 4.5.2, 4.7, 4.6
- [16] Ho-Soon Yang, David G. Cahill, X. Liu, J. L. Feldman, R. S. Crandall, B. A. Sperling, and J. R. Abelson. Anomalously high thermal conductivity of amorphous si deposited by hot-wire chemical vapor deposition. *Phys. Rev. B*, 81(10):104203, March 2010. (document), 4.1, 4.2, 4.2, 4.2, 4.5.1, 4.5.1, 4.5.2, 4.5.2, 4.7, 4.6
- [17] J. E. Turney, E. S. Landry, A. J. H. McGaughey, and C. H. Amon. Predicting phonon properties and thermal conductivity from anharmonic lattice dynamics calculations and molecular dynamics simulations. *Physical Review B*, 79:064301, 2009. (document), 1.1.2, 2.1, 2.2.2, 2.3.1, 2.3.2, 2.4.1, 2.4.1, 2.4.1, 2.1, 3.2.2, 3.3.3.1, 3.3.3.2, 3.4, 4.4.4, 4.4.4, A.3.3, A.6, A.6, A.7
- [18] Yuping He, Davide Donadio, Joo-Hyoung Lee, Jeffrey C. Grossman, and Giulia Galli. Thermal transport in nanoporous silicon: Interplay between disorder at mesoscopic and atomic scales. *ACS Nano*, 5(3):1839–1844, 2011. (document), 2.1, 2.2.2, 2.1, 3.3.2, 3.4, 4.4.3, 4.4.4, A.6, A.7
- [19] J. M. Ziman. *Electrons and Phonons*. Oxford, New York, 2001. 1.1.2, 2.3.3, 3.1, 3.2.1, 3.3.3.2, 4.2, 4.2, 4.2, 4.2, 4.5.1
- [20] D. A. Broido, M. Maloney, G. Birner, N. Mingo, and D. Stewart. Intrinsic lattice thermal conductivity of semiconductors from first principles. *Applied Physics Letters*, 91:231922, 2007. 1.1.2, 2.1, 3.1, 3.2.1
- [21] A. Ward and D. A. Broido. Intrinsic phonon relaxation times from first-principles studies of the thermal conductivities of si and ge. *Phys. Rev. B*, 81(8):085205, February 2010.

1.1.2, 3.1, 3.2.1, 3.6

- [22] Jivtesh Garg, Nicola Bonini, Boris Kozinsky, and Nicola Marzari. Role of disorder and anharmonicity in the thermal conductivity of silicon-germanium alloys: A first-principles study. *Phys. Rev. Lett.*, 106(4):045901, January 2011. 1.1.2, 3.1, 3.2.1, 3.2.2, 3.3.1, 3.3.3.2, 3.3.3.2, 3.5, 3.6, A.4
- [23] A. Ward, D. A. Broido, Derek A. Stewart, and G. Deinzer. Ab initio theory of the lattice thermal conductivity in diamond. *Phys. Rev. B*, 80(12):125203, September 2009. 1.1.2, 3.1, 3.2.1
- [24] L. Lindsay, D. A. Broido, and T. L. Reinecke. Thermal conductivity and large isotope effect in GaN from first principles. *Phys. Rev. Lett.*, 109(9):095901, August 2012. 1.1.2, 3.1, 3.2.1, 3.2.2, 3.5, 3.6, A.4
- [25] Keivan Esfarjani, Gang Chen, and Harold T. Stokes. Heat transport in silicon from first-principles calculations. *Physical Review B*, 84(8):085204, August 2011. 1.1.2, 2.1, 3.1, 3.2.2, 3.4, 3.5, 3.6, 4.5.1, A.3.3, A.3.3
- [26] Zhiting Tian, Jivtesh Garg, Keivan Esfarjani, Takuma Shiga, Junichiro Shiomi, and Gang Chen. Phonon conduction in PbSe, PbTe, and PbTe $_1$ - $x$ Se $_x$  from first-principles calculations. *Phys. Rev. B*, 85(18):184303, May 2012. 1.1.2, 3.1, 3.2.2, 3.3.3.2, 3.3.3.2, 3.5, 3.6, A.4
- [27] J. E. Turney. *Predicting phonon properties and thermal conductivity using anharmonic lattice dynamics calculations*. PhD thesis, Carnegie Mellon University, Pittsburgh, PA, 2009. 1.1.2, 1.1.4, 3.3.3.1, 3.3.3.1, 3.3.3.1, 3.3.3.2, 3.3.3.2, 3.3.3.2, A.1
- [28] Alan J. H. McGaughey. *Phonon transport in molecular dynamics simulations: Formulation and thermal conductivity prediction*. PhD thesis, University of Michigan, Ann Arbor, MI, 2004. 1.1.2, 2.4.1, 2.4.2, 3.2.3, 3.3.3.2, A.3.2, A.3.3
- [29] D. J. Ecsedy and P. G. Klemens. Thermal resistivity of dielectric crystals due to four-

- phonon processes and optical modes. *Phys. Rev. B*, 15(12):59575962, June 1977. 1.1.2, 3.3.3.2, 3.3.3.2
- [30] P. G. Klemens. The scattering of low-frequency lattice waves by static imperfections. *Proceedings of the Physical Society. Section A*, 68(1113), 1955. 1.1.2, 3.2.2, 3.3.3.1, 3.3.3.2, 4.2
- [31] P. G. Klemens. Thermal resistance due to isotopic mass variation. *Proceedings of the Physical Society. Section A*, 70(11):833, 1957. 1.1.2, 3.2.2, 3.3.3.1, 3.3.3.2
- [32] Daniel Charles Mattis. Phonon free path in an isotopic mixture. *Phys. Rev.*, 107(6):17361736, September 1957. 1.1.2, 3.2.2, 3.3.3.1, 3.3.3.2
- [33] Shin-ichiro Tamura. Isotope scattering of dispersive phonons in ge. *Phys. Rev. B*, 27(2):858866, January 1983. 1.1.2, 3.1, 3.2.2, 3.3.3.1, 3.3.3.2, 3.3.3.2, †, 3.5
- [34] W. A. Kamitakahara and B. N. Brockhouse. Vibrations of a mixed crystal: Neutron scattering from  $\text{Ni}_{.55}\text{Pd}_{.45}$ . *Phys. Rev. B*, 10(4):12001212, August 1974. 1.1.2, 3.2.2, 3.6
- [35] Wu Li, L. Lindsay, D. A. Broido, Derek A. Stewart, and Natalio Mingo. Thermal conductivity of bulk and nanowire  $\text{Mg}_{.2}\text{Si}_{.x}\text{Sn}_{.1-x}$  alloys from first principles. *Phys. Rev. B*, 86(17):174307, November 2012. 1.1.2, 3.1, 3.2.2, 3.3.3.2, 3.6
- [36] Maria N. Luckyanova, Jivtesh Garg, Keivan Esfarjani, Adam Jndl, Mayank T. Bulsara, Aaron J. Schmidt, Austin J. Minnich, Shuo Chen, Mildred S. Dresselhaus, Zhifeng Ren, Eugene A. Fitzgerald, and Gang Chen. Coherent phonon heat conduction in superlattices. *Science*, 338(6109):936939, 2012. 1.1.2, 3.1, 3.2.2, 3.6
- [37] B. Abeles. Lattice thermal conductivity of disordered semiconductor alloys at high temperatures. *Physical Review*, 131(5):19061911, September 1963. 1.1.2, 3.1, 3.2.2, 3.6, A.4

- [38] David G. Cahill and Fumiya Watanabe. Thermal conductivity of isotopically pure and ge-doped si epitaxial layers from \$300\textbackslash textbackslash textbackslash textbackslash textbackslash phantom\textbackslash textbackslash textbackslash textbackslash textbackslash rule0.3em\$. *Phys. Rev. B*, 70(23):235322, December 2004. 1.1.2, 3.2.2, 3.6
- [39] David G. Cahill, Fumiya Watanabe, Angus Rockett, and Cronin B. Vining. Thermal conductivity of epitaxial layers of dilute SiGe alloys. *Phys. Rev. B*, 71(23):235202, June 2005. 1.1.2, 3.2.2, 3.6
- [40] D.G. Cahill and RO Pohl. Lattice vibrations and heat transport in crystals and glasses. *Annual Review of Physical Chemistry*, 39(1):93121, 1988. 1.1.2, 1.1.3, 3.1, 3.2.1, 3.2.2, 3.3.2, 3.3.4, 3.3.4, 3.6, 4.1, 4.4.5, 4.5.1, 4.5.1, 4.6
- [41] Takuma Shiga, Junichiro Shiomi, Jie Ma, Olivier Delaire, Tomasz Radzynski, Andrzej Lusakowski, Keivan Esfarjani, and Gang Chen. Microscopic mechanism of low thermal conductivity in lead telluride. *Phys. Rev. B*, 85(15):155203, April 2012. 1.1.2, 3.1, 3.2.2, 3.6
- [42] I. Kudman. Thermoelectric properties of p-type PbTe-PbSe alloys. *Journal of Materials Science*, 7(9):10271029, 1972. 1.1.2, 3.2.2
- [43] Yanzhong Pei, Xiaoya Shi, Aaron LaLonde, Heng Wang, Lidong Chen, and G. Jeffrey Snyder. Convergence of electronic bands for high performance bulk thermoelectrics. *Nature*, 473(7345):6669, May 2011. 1.1.2, 3.2.2
- [44] Philip B. Allen and Joseph L. Feldman. Thermal conductivity of disordered harmonic solids. *Physical Review B*, 48(17):1258112588, November 1993. 1.1.3, 3.2.1, 3.2.1, 3.3.4, ‡, 3.3.5, 3.6, 4.1, 4.2, 4.2, A.5
- [45] Joseph L. Feldman, Mark D. Kluge, Philip B. Allen, and Frederick Wooten. Thermal conductivity and localization in glasses: Numerical study of a model of amorphous silicon. *Physical Review B*, 48(17):1258912602, November 1993. 1.1.3, 1.1.4, 3.1, 3.2.1, \*, 3.3.4,

3.3.4, 3.3.5, 4.1, 4.2, 4.2, 4.2, 4.2, 4.3.2, 4.4.2, 4.4.2, 4.4.4, 4.4.5, 4.4.5, 4.4.5, 4.5.1, 4.5.1, 4.5.2, 4.6, A.2, A.5

- [46] Joseph L. Feldman, Philip B. Allen, and Scott R. Bickham. Numerical study of low-frequency vibrations in amorphous silicon. *Phys. Rev. B*, 59(5):35513559, February 1999.
- 1.1.3, 3.2.1, 3.3.2, 3.3.2, 3.3.4, 3.3.5, 4.1, 4.2, 4.2, 4.2, 4.2, 4.3.1, 4.3.2, 4.4.2, 4.4.2, 4.4.4, 4.4.5, 4.5.1, 4.5.1, 4.5.2, 4.6, A.2
- [47] D. G. Cahill, W. K. Ford, K. E. Goodson, G. D. Mahan, A. Majumdar, H. J. Maris, R. Merlin, and S. R. Phillpot. Nanoscale thermal transport. *Journal of Applied Physics*, 93:793818, 2003. 2.1
- [48] A. D. McConnell and K. E. Goodson. Thermal conduction in silicon micro and nanostructures. *Annual Review of Heat Transfer*, 14:129168, 2005. 2.1
- [49] G. P. Srivastava. *The Physics of Phonons*. Adam Hilger, Bristol, 1990. 2.1, 2.2.1, A.1, A.4
- [50] D. C. Wallace. *Thermodynamics of Crystals*. Cambridge Univ. Press, Cambridge, UK, 1972. 2.1, 2.2.1, A.1, A.1
- [51] A. A. Maradudin. Dynamical properties of solids, volume 1. In G. K. Horton and A. A. Maradudin, editors, *Dynamical Properties of Solids, Volume 1*, page 182. Elsevier, New York, 1974. 2.1, 2.2.1, A.1
- [52] M. T. Dove. *Introduction to Lattice Dynamics*. Cambridge, Cambridge, 1993. 2.1, 2.2.1, 2.2.1, 2.3.1, 2.3.2, 3.3.3.1, 4.2, 4.4.2, 4.4.4, A.1, A.2
- [53] M. Asheghi, Y. K. Leung, S. S. Wong, and K. E. Goodson. Phonon-boundary scattering in thin silicon layers. *Applied Physics Letters*, 71:17981800, 1997. 2.1
- [54] Alexander Balandin and Kang L. Wang. Significant decrease of the lattice thermal conductivity due to phonon confinement in a free-standing semiconductor quantum well. *Physical Review B*, 58(3):15441549, July 1998. 2.1

- [55] Zhitong Tian, Keivan Esfarjani, Junichiro Shiomi, Asegun S. Henry, and Gang Chen. On the importance of optical phonons to thermal conductivity in nanostructures. *Applied Physics Letters*, 99(5):053122, 2011. 2.1
- [56] A. I. Hochbaum, R. Chen, R. D. Delgado, W. Liang, E. C. Garnett, M. Najarian, A. Majumdar, and P. Yang. Enhanced thermoelectric performance of rough silicon nanowires. *Nature*, 451:163167, 2008. 2.1
- [57] P. Martin, Z. Aksamija, E. Pop, and U. Ravaioli. Impact of phonon-surface roughness scattering on thermal conductivity of thin si nanowires. *Physical Review Letters*, 102:125503, 2009. 2.1
- [58] Patrick E. Hopkins, Charles M. Reinke, Mehmet F. Su, Roy H. Olsson, Eric A. Shaner, Zayd C. Leseman, Justin R. Serrano, Leslie M. Phinney, and Ihab El-Kady. Reduction in the thermal conductivity of single crystalline silicon by phononic crystal patterning. *Nano Letters*, 11(1):107112, 2011. 2.1
- [59] E. S. Landry, M. I. Hussein, and A. J. H. McGaughey. Complex superlattice unit cell designs for reduced thermal conductivity. *Physical Review B*, 77:184302, 2008. 2.1, 3.4
- [60] A. J. H. McGaughey, E. S. Landry, D. P. Sellan, and C. H. Amon. Size-dependent model for thin film and nanowire thermal conductivity. *Applied Physics Letters*, 99:131904, 2011. 2.1, 2.5
- [61] E. S. Landry and A. J. H. McGaughey. Effect of interfacial species mixing on phonon transport in semiconductor superlattices. *Physical Review B*, 79:075316, 2009. 2.1
- [62] E. S. Landry. *Thermal transport by phonons across semiconductor interfaces, thin films, and superlattices*. PhD thesis, Carnegie Mellon University, Pittsburgh, PA, 2009. 2.1, 3.2.2
- [63] J. Callaway. Model for lattice thermal conductivity at low temperatures. *Physical Review*, 113:1046, 1959. 2.1, 3.2.2, 3.3.3.1, 4.2, A.3.3

- [64] M. G. Holland. Analysis of lattice thermal conductivity. *Physical Review*, 132:2461, 1963. 2.1
- [65] A. J. C. Ladd, B. Moran, and W. G. Hoover. Lattice thermal conductivity: A comparison of molecular dynamics and anharmonic lattice dynamics. *Physical Review B*, 34:50585064, 1986. 2.1, 2.2.2, 3.3.3.1, 3.3.3.1, 4.4.4, 4.4.4
- [66] A. J. H. McGaughey and M. Kaviany. Quantitative validation of the boltzmann transport equation phonon thermal conductivity model under the single-mode relaxation time approximation. *Physical Review B*, 69:094303, 2004. 2.1, 2.2.2, 2.3.1, 2.3.3, ‡, 2.4.1, 3.2.1, 3.3.3.1, 3.4, 4.2, 4.4.4, A.3.3
- [67] P. K. Schelling, S. R. Phillpot, and P. Kebinski. Comparison of atomic-level simulation methods for computing thermal conductivity. *Physical Review B*, 65:144306, 2002. 2.1
- [68] D. P. Sellan, E. S. Landry, J. E. Turney, A. J. H. McGaughey, and C. H. Amon. Size effects in molecular dynamics thermal conductivity prediction. *Physical Review B*, 81:214305, 2010. 2.1, 2.3.1, 3.5, A.6
- [69] A. A. Maradudin and A. E. Fein. Scattering of neutrons by an anharmonic crystal. *Physical Review*, 128:25892608, 1962. 2.1, 3.3.3.1, 3.3.3.2
- [70] J. E. Turney, A. J. H. McGaughey, and C. H. Amon. Assessing the applicability of quantum corrections to classical thermal conductivity predictions. *Physical Review B*, 79:224305, 2009. 2.1
- [71] A. S. Henry and G. Chen. Spectral phonon transport properties of silicon based on molecular dynamics simulations and lattice dynamics. *Journal of Computational and Theoretical Nanoscience*, 5:112, 2008. 2.1, 2.2.2, 4.4.4
- [72] J. V. Goicochea, M. Madrid, and C. H. Amon. Thermal properties for bulk silicon based on the determination of relaxation times using molecular dynamics. *Journal of Heat Transfer*, 132:012401, 2010. 2.1, 2.2.2, 2.3.3, 3.2.1, 3.2.3, A.3.3



- [81] N. W. Ashcroft and N. D. Mermin. *Solid State Physics*. Saunders, Fort Worth, 1976. 2.1, 2.3.1, 3.1, 3.3.1, 3.3.3.1, 4.2, 4.2, 4.2, A.3.3
- [82] D. W. Brenner, O. A. Shenderova, J. A. Harrison, S. J. Stuart, B. Ni, and S. B. Sinnott. A second-generation reactive empirical bond order (REBO) potential energy expression for hydrocarbons. *Journal of Physics: Condensed Matter*, 14:783802, 2002. 2.1, 2.4.3
- [83] W. Rudin. *Real and Complex Analysis*. McGraw-Hill, New York, 1987. 2.2.2, A.1
- [84] A. J. H. McGaughey and M. Kaviany. Phonon transport in molecular dynamics simulations: Formulation and thermal conductivity prediction. In G. A. Greene, Y. I. Cho, J. P. Hartnett, and A. Bar-Cohen, editors, *Advances in Heat Transfer, Volume 39*, page 169255. Elsevier, 2006. 2.3.2, 2.4.1, 3.3.2
- [85] D. A. McQuarrie. *Statistical Mechanics*. University Science Books, Sausalito, 2000. 2.3.3, 2.4.1, 2.4.1, 2.4.2, 2.4.3, 3.2.1, 4.2, 4.3.2
- [86] J. D. Gale and A. L. Rohl. The general utility lattice program. *Molecular Simulation*, 29:291, 2003. 2.3.4, 2.4.1, 2.4.2, 3.3.1, 3.3.2, 3.3.4, 4.3.2, 4.4.3, 4.4.3
- [87] Steve Plimpton. Fast parallel algorithms for short-range molecular dynamics. *Journal of Computational Physics*, 117(1):1–19, 1995. 2.3.4, 2.4.1, 2.4.2, 3.2.3, 4.3.1
- [88] Paul F. Dubois, Konrad Hinsen, and James Hugunin. Numerical python. *Computers in Physics*, 10(3), June 1996. 2.3.4
- [89] J. A. Thomas. *water flow and thermal transport through carbon nanotubes*. PhD thesis, Carnegie Mellon University, Pittsburgh, PA, 2010. 2.3.4
- [90] J. E. Graebner, B. Golding, and L. C. Allen. Phonon localization in glasses. *Phys. Rev. B*, 34(8):56965701, October 1986. 3.1, 3.6, 4.1, 4.2
- [91] X. Lu, M. C. Arduini-Schuster, J. Kuhn, O. Nilsson, J. Fricke, and R. W. Pekala. Thermal conductivity of monolithic organic aerogels. *Science*, 255(5047):971972, 1992. 3.1
- [92] G Chen, M S Dresselhaus, G Dresselhaus, J Fleurial, and T Caillat. Recent developments

- in thermoelectric materials. *International Materials Reviews*, 48(1):4566, 2003. 3.1
- [93] D. R. Clarke and S. R. Phillipot. Thermal barrier coating materials. *Materials Today*, June:2229, 2005. 3.1
- [94] G. J. Snyder and E. S. Toberer. Complex thermoelectric materials. *Nature Materials*, 7:105114, 2008. 3.1
- [95] A. J. Minnich, M. S. Dresselhaus, Z. F. Ren, and G. Chen. Bulk nanostructured thermoelectric materials: current research and future prospects. *Energy Environ. Sci.*, 2(5):, 2009. 3.1
- [96] Eric S. Toberer, Alex Zevalkink, and G. Jeffrey Snyder. Phonon engineering through crystal chemistry. *J. Mater. Chem.*, 21(40), 2011. 3.1
- [97] M. Zebarjadi, K. Esfarjani, M. S. Dresselhaus, Z. F. Ren, and G. Chen. Perspectives on thermoelectrics: from fundamentals to device applications. *Energy Environ. Sci.*, 5(1):51475162, 2012. 3.1
- [98] Scott N. Schiffres, Kyu Hun Kim, Lin Hu, Alan J. H. McGaughey, Mohammad F. Islam, and Jonathan A. Malen. Gas diffusion, energy transport, and thermal accommodation in single-walled carbon nanotube aerogels. *Advanced Functional Materials*, page DOI:10.1002/adfm.201201285, 2012. 3.1
- [99] B. Abeles, D. S. Beers, G. D. Cody, and J. P. Dismukes. Thermal conductivity of ge-si alloys at high temperatures. *Phys. Rev.*, 125(1):4446, January 1962. 3.1, 3.6
- [100] P. B. Allen, J. L. Feldman, J. Fabian, and F. Wooten. Diffusons, locons, and propagons: character of atomic vibrations in amorphous si. *Philosophical Magazine B*, 79:17151731, 1999. 3.1, 3.3.2, 3.3.2, 3.6, 4.1, 4.4.1, 4.4.2, 4.4.2, 4.4.3, 4.4.4, 4.6, A.2, A.5
- [101] Hua Bao, Bo Qiu, Yu Zhang, and Xiulin Ruan. A first-principles molecular dynamics approach for predicting optical phonon lifetimes and far-infrared reflectance of polar materials. *Journal of Quantitative Spectroscopy and Radiative Transfer*, 113(13):1683–1688,

2012. 3.1

- [102] Gabriele C. Sosso, Davide Donadio, Sebastiano Caravati, Jrg Behler, and Marco Bernasconi. Thermal transport in phase-change materials from atomistic simulations. *Phys. Rev. B*, 86(10):104301, September 2012. 3.1
- [103] Ashton Skye and Patrick K. Schelling. Thermal resistivity of SiGe alloys by molecular-dynamics simulation. *Journal of Applied Physics*, 103(11):113524, 2008. 3.2.2
- [104] Zhiting Tian, Keivan Esfarjani, and Gang Chen. Enhancing phonon transmission across a Si/Ge interface by atomic roughness: First-principles study with the green's function method. *Phys. Rev. B*, 86(23):235304, December 2012. 3.2.2
- [105] Yuping He, Ivana Savic, Davide Donadio, and Giulia Galli. Lattice thermal conductivity of semiconducting bulk materials: Atomistic simulations. *Phys. Chem. Chem. Phys.*, page , 2012. 3.2.3, 3.3.3.1, 3.4, 4.4.4, 4.4.4
- [106] D. P. Sellan, J. E. Turney, A. J. H. McGaughey, and C. H. Amon. Cross-plane phonon transport in thin films. *Journal of Applied Physics*, 108:113524, 2010. 3.2.3, 3.5
- [107] A. M. Bouchard, R. Biswas, W. A. Kamitakahara, G. S. Grest, and C. M. Soukoulis. Vibrational properties of amorphous silicon-germanium alloys and superlattices. *Phys. Rev. B*, 38(15):1049910506, November 1988. 3.3.1
- [108] John C. Duda, Timothy S. English, Donald A. Jordan, Pamela M. Norris, and William A. Soffa. Reducing thermal conductivity of binary alloys below the alloy limit via chemical ordering. *Journal of Physics: Condensed Matter*, 23(20):205401, 2011. 3.3.1, 3.3.2, 4.4.3
- [109] Qian-Jin Chu and Zhao-Qing Zhang. Effect of correlations on the localization properties of electrons and phonons in the long-wavelength limit. *Phys. Rev. B*, 39(10):71207131, April 1989. 3.3.1
- [110] Yuping He, Davide Donadio, and Giulia Galli. Heat transport in amorphous silicon: Interplay between morphology and disorder. *Applied Physics Letters*, 98(14):144101, 2011.

3.3.2, 3.3.3.1, 4.1, 4.2, 4.2, 4.3.1, 4.4.3, 4.4.4, 4.4.4, 4.4.5, 4.5.1, 4.5.1, A.5, B.4.2

- [111] Davide Donadio and Giulia Galli. Atomistic simulations of heat transport in silicon nanowires. *Phys. Rev. Lett.*, 102(19):195901, May 2009. 3.3.2, 3.3.3.1, 4.4.1, 4.4.3
- [112] Takuma Hori, Takuma Shiga, and Junichiro Shiomi. Phonon transport analysis of silicon germanium alloys using molecular dynamics simulations. *Journal of Applied Physics*, 113(20):203514, 2013. 3.3.2, 3.3.3.1, 4.4.3, 4.4.4
- [113] Y. M. Beltukov, V. I. Kozub, and D. A. Parshin. Ioffe-regel criterion and diffusion of vibrations in random lattices. *Phys. Rev. B*, 87(13):134203, April 2013. 3.3.2, 3.3.5, 3.6, 4.4.2, 4.4.2, 4.4.5, A.2, A.2
- [114] S. Volz and G. Chen. Molecular-dynamics simulation of thermal conductivity of silicon crystals. *Physical Review B*, 61:26512656, 2000. 3.3.2, 4.4.2, A.2
- [115] N. L. Green, D. Kaya, C. E. Maloney, and M. F. Islam. Density invariant vibrational modes in disordered colloidal crystals. *Physical Review E*, 83(5):051404, May 2011. 3.3.2, 4.4.2
- [116] J. M. Larkin, J. E. Turney, A. D. Massicotte, C. H. Amon, and A. J. H. McGaughey. Comparison and evaluation of spectral energy methods for predicting phonon properties. *to appear in Journal of Computational and Theoretical Nanoscience*, 2012. 3.3.3.1, 3.3.3.1, 4.2, 4.4.4, 4.4.4, 4.5.1, A.3.3, A.4
- [117] Yuping He, Davide Donadio, and Giulia Galli. Morphology and temperature dependence of the thermal conductivity of nanoporous SiGe. *Nano Letters*, 11(9):3608–3611, August 2011. 3.3.3.1, 3.5, 4.4.3, 4.4.4
- [118] Sergei Shenogin, Arun Bodapati, Paweł Keblinski, and Alan J. H. McGaughey. Predicting the thermal conductivity of inorganic and polymeric glasses: The role of anharmonicity. *Journal of Applied Physics*, 105(3):034906, 2009. 3.3.4, 4.5.1, A.5
- [119] Ping Sheng. *Introduction to Wave Scattering: Localization and Mesoscopic Phenomena*. Springer, April 2006. 3.3.4

- [120] Vincenzo Vitelli, Ning Xu, Matthieu Wyart, Andrea J. Liu, and Sidney R. Nagel. Heat transport in model jammed solids. *Phys. Rev. E*, 81(2):021301, February 2010. 3.3.4, 3.3.5, 3.6, 4.2, 4.4.5
- [121] Ning Xu, Vincenzo Vitelli, Matthieu Wyart, Andrea J. Liu, and Sidney R. Nagel. Energy transport in jammed sphere packings. *Phys. Rev. Lett.*, 102(3):038001, January 2009. 3.3.5, 3.6, 4.2, 4.4.5
- [122] Ping Sheng and Minyao Zhou. Heat conductivity of amorphous solids: Simulation results on model structures. *Science*, 253(5019):539542, 1991. 3.3.5, 3.6, 4.4.4, 4.4.5
- [123] K. Esfarjani and H. T. Stokes. Method to extract anharmonic force constants from first principles calculations. *Physical Review B*, 77:144112, 2008. 3.5
- [124] Laurent Chaput, Atsushi Togo, Isao Tanaka, and Gilles Hug. Phonon-phonon interactions in transition metals. *Phys. Rev. B*, 84(9):094302, September 2011. 3.5
- [125] Ramez Cheaito, John C. Duda, Thomas E. Beechem, Khalid Hattar, Jon F. Ihlefeld, Douglas L. Medlin, Mark A. Rodriguez, Michael J. Campion, Edward S. Piekos, and Patrick E. Hopkins. Experimental investigation of size effects on the thermal conductivity of silicon-germanium alloy thin films. *Phys. Rev. Lett.*, 109(19):195901, November 2012. 3.6
- [126] C. Kittel. Interpretation of the thermal conductivity of glasses. *Physical Review*, 75:974, 1949. 3.6
- [127] David M. Leitner. Vibrational energy transfer and heat conduction in a one-dimensional glass. *Physical Review B*, 64(9):094201, August 2001. 4.1
- [128] Rubina Sultan, A. D. Avery, J. M. Underwood, S. J. Mason, D. Bassett, and B. L. Zink. Heat transport by long mean free path vibrations in amorphous silicon nitride near room temperature. *Phys. Rev. B*, 87(21):214305, June 2013. 4.1
- [129] M. S. Love and A. C. Anderson. Estimate of phonon thermal transport in amorphous materials above 50 k. *Phys. Rev. B*, 42(3):18451847, July 1990. 4.1, 4.2, 4.2, 4.5.1, 4.6

- [130] G. Baldi, V. M. Giordano, G. Monaco, F. Sette, E. Fabiani, A. Fontana, and G. Ruocco. Thermal conductivity and terahertz vibrational dynamics of vitreous silica. *Phys. Rev. B*, 77(21):214309, June 2008. 4.1, 4.2, 4.2, 4.4.2, 4.4.2, 4.4.5, 4.5.1, 4.6
- [131] Yee Kan Koh and David G. Cahill. Frequency dependence of the thermal conductivity of semiconductor alloys. *Phys. Rev. B*, 76(7):075207, August 2007. 4.1, 4.5.2, 4.6
- [132] C. Dames and G. Chen. Thermal conductivity of nanostructured thermoelectric materials. In D. M. Rowe, editor, *Thermoelectrics Handbook: Macro to Nano*, pages 421–42–11. Taylor & Francis, 2005. 4.1, 4.5.2
- [133] A. J. Minnich, J. A. Johnson, A. J. Schmidt, K. Esfarjani, M. S. Dresselhaus, K. A. Nelson, and G. Chen. Thermal conductivity spectroscopy technique to measure phonon mean free paths. *Phys. Rev. Lett.*, 107(9):095901, August 2011. 4.1, 4.6
- [134] Fan Yang and Chris Dames. Mean free path spectra as a tool to understand thermal conductivity in bulk and nanostructures. *Physical Review B*, 87(3):035437, January 2013. 4.1, 4.5.2
- [135] A. D. Christianson, M. D. Lumsden, O. Delaire, M. B. Stone, D. L. Abernathy, M. A. McGuire, A. S. Sefat, R. Jin, B. C. Sales, D. Mandrus, E. D. Mun, P. C. Canfield, J. Y. Y. Lin, M. Lucas, M. Kresch, J. B. Keith, B. Fultz, E. A. Goremychkin, and R. J. McQueeney. Phonon density of states of  $\text{LaFeAsO}_{1-x}\text{F}_x$ . *Phys. Rev. Lett.*, 101(15):157004, October 2008. 4.1
- [136] R. C. Zeller and R. O. Pohl. Thermal conductivity and specific heat of noncrystalline solids. *Phys. Rev. B*, 4(6):20292041, September 1971. 4.1
- [137] J. J. Freeman and A. C. Anderson. Thermal conductivity of amorphous solids. *Phys. Rev. B*, 34(8):56845690, October 1986. 4.1, 4.2, 4.6
- [138] David G. Cahill and R. O. Pohl. Heat flow and lattice vibrations in glasses. *Solid State Communications*, 70(10):927–930, 1989. 4.1

- [139] B L Zink, R Pietri, and F Hellman. Thermal conductivity and specific heat of thin-film amorphous silicon. *Physical Review Letters*, 96(5):055902, 2006. 4.1, 4.5.2
- [140] D. B. Hondongwa, B. C. Daly, T. B. Norris, B. Yan, J. Yang, and S. Guha. Ultrasonic attenuation in amorphous silicon at 50 and 100 GHz. *Phys. Rev. B*, 83(12):121303, March 2011. 4.1, 4.4.5, 5.2.3
- [141] C. Masciovecchio, G. Baldi, S. Caponi, L. Comez, S. Di Fonzo, D. Fioretto, A. Fontana, A. Gessini, S. C. Santucci, F. Sette, G. Viliani, P. Vilmercati, and G. Ruocco. Evidence for a crossover in the frequency dependence of the acoustic attenuation in vitreous silica. *Phys. Rev. Lett.*, 97(3):035501, July 2006. 4.1, 4.2, 4.4.5, 4.6
- [142] G. Baldi, V. M. Giordano, G. Monaco, and B. Ruta. Sound attenuation at terahertz frequencies and the boson peak of vitreous silica. *Phys. Rev. Lett.*, 104(19):195501, May 2010. 4.1, 4.2, 4.4.2, 4.4.2, 4.4.5, 4.6
- [143] Giacomo Baldi, Valentina M. Giordano, and Giulio Monaco. Elastic anomalies at terahertz frequencies and excess density of vibrational states in silica glass. *Phys. Rev. B*, 83(17):174203, May 2011. 4.1, 4.2, 4.4.5
- [144] G. Baldi, M. Zanatta, E. Gilioli, V. Milman, K. Refson, B. Wehinger, B. Winkler, A. Fontana, and G. Monaco. Emergence of crystal-like atomic dynamics in glasses at the nanometer scale. *Phys. Rev. Lett.*, 110(18):185503, May 2013. 4.1, 4.2, 4.4.2, 4.4.2, 4.4.5, 4.6
- [145] G. Pompe and E. Hegenbarth. Thermal conductivity of amorphous si at low temperatures. *physica status solidi (b)*, 147(1):103–108, May 1988. 4.1
- [146] B. L. Zink, R. Islam, David J. Smith, and F. Hellman. Excess modes and enhanced scattering in rare-earth-doped amorphous silicon thin films. *Phys. Rev. B*, 74(20):205209, November 2006. 4.1, 4.5.2
- [147] D. G. Cahill, H. E. Fischer, T. Klitsner, E. T. Swartz, and R. O. Pohl. Thermal conduc-

tivity of thin films: Measurements and understanding. *Journal of Vacuum Science and Technology A*, 7:12591266, 1989. 4.1, 4.6

- [148] C. J. Morath and H. J. Maris. Phonon attenuation in amorphous solids studied by picosecond ultrasonics. *Phys. Rev. B*, 54(1):203213, July 1996. 4.2
- [149] P. Benassi, M. Krisch, C. Masciovecchio, V. Mazzacurati, G. Monaco, G. Ruocco, F. Sette, and R. Verbeni. Evidence of high frequency propagating modes in vitreous silica. *Phys. Rev. Lett.*, 77(18):38353838, October 1996. 4.2, 4.4.2, 4.4.3
- [150] S. N. Taraskin and S. R. Elliott. Propagation of plane-wave vibrational excitations in disordered systems. *Phys. Rev. B*, 61(18):1201712030, May 2000. 4.2, 4.4.2, A.2
- [151] W. Gtze and M. R. Mayr. Evolution of vibrational excitations in glassy systems. *Phys. Rev. E*, 61(1):587606, January 2000. 4.2, 4.4.2
- [152] G. Ruocco, F. Sette, R. Di Leonardo, G. Monaco, M. Sampoli, T. Scopigno, and G. Viliani. Relaxation processes in harmonic glasses? *Phys. Rev. Lett.*, 84(25):57885791, June 2000. 4.2, 4.4.2, 5.2.2
- [153] Giancarlo Ruocco and Francesco Sette. High-frequency vibrational dynamics in glasses. *Journal of Physics: Condensed Matter*, 13(41):9141, 2001. 4.2, 4.4.2, 4.4.2, 4.4.3
- [154] J. Horbach, W. Kob, and K. Binder. High frequency sound and the boson peak in amorphous silica. *The European Physical Journal B - Condensed Matter and Complex Systems*, 19(4):531–543, 2001. 4.2, 4.4.2, 4.4.2, 4.4.3, 5.2.3, A.2
- [155] A. Matic, D. Engberg, C. Masciovecchio, and L. Brjesson. Sound wave scattering in network glasses. *Phys. Rev. Lett.*, 86(17):38033806, April 2001. 4.2
- [156] J. L. Feldman. Calculations of the generalized dynamic structure factor for amorphous silicon. *Journal of Non-Crystalline Solids*, 307310(0):128 – 134, 2002. 4.2, 4.4.2, 4.4.2, 4.4.3, A.2
- [157] B. Ruffl, M. Foret, E. Courtens, R. Vacher, and G. Monaco. Observation of the onset of

strong scattering on high frequency acoustic phonons in densified silica glass. *Phys. Rev.*

*Lett.*, 90(9):095502, March 2003. 4.2

- [158] W. Schirmacher, G. Ruocco, and T. Scopigno. Acoustic attenuation in glasses and its relation with the boson peak. *Phys. Rev. Lett.*, 98(2):025501, January 2007. 4.2
- [159] J. K. Christie, S. N. Taraskin, and S. R. Elliott. Vibrational behavior of a realistic amorphous-silicon model. *Journal of Non-Crystalline Solids*, 353(2223):2272 – 2279, 2007. 4.2, 4.4.2, 4.4.3, A.2
- [160] Hiroshi Shintani and Hajime Tanaka. Universal link between the boson peak and transverse phonons in glass. *Nat Mater*, 7(11):870–877, November 2008. 4.2, 4.4.2, A.2
- [161] Carl Ganter and Walter Schirmacher. Rayleigh scattering, long-time tails, and the harmonic spectrum of topologically disordered systems. *Phys. Rev. B*, 82(9):094205, September 2010. 4.2
- [162] M. Wyart. Scaling of phononic transport with connectivity in amorphous solids. *EPL (Europhysics Letters)*, 89(6):64001, 2010. 4.2, 4.4.2, A.2
- [163] S. Ayrinhac, M. Foret, A. Devos, B. Ruffl, E. Courtens, and R. Vacher. Subterahertz hypersound attenuation in silica glass studied via picosecond acoustics. *Phys. Rev. B*, 83(1):014204, January 2011. 4.2
- [164] The summation in Eq. (4.10) is performed over all modes  $j \neq i$  including modes with  $\omega < \omega_{cut}$ . 4.2
- [165] B. W. H. van Beest, G. J. Kramer, and R. A. van Santen. Force fields for silicas and aluminophosphates based on ab initio calculations. *Physical Review Letters*, 64(16):19551958, April 1990. 4.3.1, 4.4.2, 4.6
- [166] G. J. Kramer, N. P. Farragher, B. W. H. van Beest, and R. A. van Santen. Interatomic force fields for silicas, aluminophosphates, and zeolites: Derivation based on ab initio calculations. *Physical Review B*, 43(6):50685080, February 1991. 4.3.1, 4.4.2, 4.6

- [167] Yves Guissani and Bertrand Guillot. A numerical investigation of the liquidvapor coexistence curve of silica. *The Journal of Chemical Physics*, 104(19):7633–7644, 1996. 4.3.1, 4.4.2, 4.6
- [168] D. Wolf, P. Kebelinski, S. R. Phillpot, and J. Eggebrecht. Exact method for the simulation of coulombic systems by spherically truncated, pairwise  $r^{[-1]}$  summation. *The Journal of Chemical Physics*, 110(17):8254–8282, 1999. 4.3.1
- [169] G. T. Barkema and Normandousseau. High-quality continuous random networks. *Phys. Rev. B*, 62(8):49854990, August 2000. 4.3.1, 4.4.2, 4.4.3, 4.6
- [170] U. Buchenau, H. M. Zhou, N. Nucker, K. S. Gilroy, and W. A. Phillips. Structural relaxation in vitreous silica. *Phys. Rev. Lett.*, 60(13):13181321, March 1988. 4.3.1
- [171] Murat Durandurdu and D. A. Drabold. *Ab initio* simulation of pressure-induced low-energy excitations in amorphous silicon. *Phys. Rev. B*, 66(15):155205, October 2002. 4.3.1
- [172] N. Bernstein, J. L. Feldman, and M. Fornari. Structural model of amorphous silicon annealed with tight binding. *Phys. Rev. B*, 74(20):205202, November 2006. 4.3.1
- [173] Jie Chen, Gang Zhang, and Baowen Li. How to improve the accuracy of equilibrium molecular dynamics for computation of thermal conductivity? *Physics Letters A*, 374(23):23922396, May 2010. 4.3.2
- [174] Francesco Sette, Michael H. Krisch, Claudio Masciovecchio, Giancarlo Ruocco, and Giulio Monaco. Dynamics of glasses and glass-forming liquids studied by inelastic x-ray scattering. *Science*, 280(5369):1550–1555, 1998. 4.4.2
- [175] B. Ruzicka, T. Scopigno, S. Caponi, A. Fontana, O. Pilla, P. Giura, G. Monaco, E. Pontecorvo, G. Ruocco, and F. Sette. Evidence of anomalous dispersion of the generalized sound velocity in glasses. *Phys. Rev. B*, 69(10):100201, March 2004. 4.4.2, 4.4.2, 4.4.3
- [176] D. Kaya, N. L. Green, C. E. Maloney, and M. F. Islam. Normal modes and density of

states of disordered colloidal solids. *Science*, 329(5992):656–658, 2010. 4.4.2

- [177] R. Biswas, A. M. Bouchard, W. A. Kamitakahara, G. S. Grest, and C. M. Soukoulis. Vibrational localization in amorphous silicon. *Phys. Rev. Lett.*, 60(22):22802283, May 1988. 4.4.2, 4.4.2, 4.4.3, 4.6, A.2
- [178] Victor Martin-Mayor, Marc Mezard, Giorgio Parisi, and Paolo Verrocchio. The dynamical structure factor in topologically disordered systems. *The Journal of Chemical Physics*, 114(18):8068–8081, 2001. 4.4.2, A.2
- [179] S. Ciliberti, T. S. Grigera, V. Martin-Mayor, G. Parisi, and P. Verrocchio. Brillouin and boson peaks in glasses from vector euclidean random matrix theory. *The Journal of Chemical Physics*, 119(16):8577–8591, 2003. 4.4.2, A.2
- [180] Jason M. Larkin and Alan J. H. McGaughey. Predicting alloy vibrational mode properties using lattice dynamics calculations, molecular dynamics simulations, and the virtual crystal approximation. *Journal of Applied Physics*, 114(2):023507, 2013. 4.4.2, 4.4.4, 4.4.4, 4.4.5, A.2
- [181] Alessia Marruzzo, Walter Schirmacher, Andrea Fratocchia, and Giancarlo Ruocco. Heterogeneous shear elasticity of glasses: the origin of the boson peak. *Sci. Rep.*, 3, March 2013. 4.4.2, A.2
- [182] J.S. Cowpe, J.S. Astin, R.D. Pilkington, and A.E. Hill. Temporally resolved laser induced plasma diagnostics of single crystal silicon effects of ambient pressure. *A collection of papers presented at the Euro Mediterranean Symposium on Laser Induced Breakdown Spectroscopy (EMSLIBS 2007)*, 63(10):1066–1071, October 2008. 4.4.2
- [183] R. Vacher, J. Pelous, F. Plicque, and A. Zarembowitch. Ultrasonic and brillouin scattering study of the elastic properties of vitreous silica between 10 and 300 k. *Journal of Non-Crystalline Solids*, 45(3):397–410, September 1981. 4.4.3
- [184] A. Polian, Dung Vo-Thanh, and P. Richet. Elastic properties of a-SiO<sub>2</sub> up to 2300 k from

- brillouin scattering measurements. *EPL (Europhysics Letters)*, 57(3):375, 2002. 4.4.3
- [185] Mark D. Kluge and John R. Ray. Elastic constants and density of states of a molecular-dynamics model of amorphous silicon. *Phys. Rev. B*, 37(8):41324136, March 1988. 4.4.3
- [186] J. L. Feldman, J. Q. Broughton, and F. Wooten. Elastic properties of amorphous si and derived debye temperatures and grneisen parameters: Model calculation. *Phys. Rev. B*, 43(3):21522158, January 1991. 4.4.3
- [187] F Wooten, K Winer, D Weaire, et al. Computer generation of structural models of amorphous si and ge. *Physical review letters*, 54(13):13921395, 1985. 4.4.3
- [188] R. Vacher, H. Sussner, and M. Schmidt. Attenuation of surface phonons in opaque materials measured by brillouin scattering. *Solid State Communications*, 34(5):279 – 281, 1980. 4.4.3, 4.5.1
- [189] V. Mazzacurati, G. Ruocco, and M. Sampoli. Low-frequency atomic motion in a model glass. *EPL (Europhysics Letters)*, 34(9):681, 1996. 4.4.4, 5.2.2
- [190] S. R. Bickham and J. L. Feldman. Calculation of vibrational lifetimes in amorphous silicon using molecular dynamics simulations. *Phys. Rev. B*, 57(19):1223412238, May 1998. 4.4.4
- [191] S. R. Bickham. Numerical calculation of relaxation rates in amorphous silicon. *Phys. Rev. B*, 59(7):48944897, February 1999. 4.4.4
- [192] Jaroslav Fabian and Philip B. Allen. Anharmonic decay of vibrational states in amorphous silicon. *Phys. Rev. Lett.*, 77(18):38393842, October 1996. 4.4.4
- [193] Jaroslav Fabian, Joseph L. Feldman, C. Stephen Hellberg, and S. M. Nakhmanson. Numerical study of anharmonic vibrational decay in amorphous and paracrystalline silicon. *Phys. Rev. B*, 67(22):224302, June 2003. 4.4.4
- [194] P. Jund and R. Jullien. Molecular-dynamics calculation of the thermal conductivity of vitreous silica. *Physical Review B*, 59:1370713711, 1999. 4.5.1

- [195] We do not observe that tiling the a-Si model increases the thermal conductivity above the expected linear scaling as was found in Ref. 110 using the MD-based direct method. This finding is likely due to the small model used to perform the tiling in that study (512 atoms), while we use a large model (100,000 atoms). 4.5.1
- [196] K. T. Regner, S. Majumdar, and J. A. Malen. Instrumentation of broadband frequency domain thermoreflectance for measuring thermal conductivity accumulation functions. *Review of Scientific Instruments*, 84(6):064901, 2013. 4.6
- [197] Gene H Golub and Charles F Van Loan. *Matrix computations*, volume 3. JHU Press, 2012. 5.2.2
- [198] Jean Pierre Boom and Sideney Yip. *Molecular Hydrodynamics*. DoverPublications. com, 1980. 5.2.3
- [199] J. E. Turney, A. J. H. McGaughey, and C. H. Amon. In-plane phonon transport in thin films. *Journal of Applied Physics*, 107(2):024317, 2010. A.3.3
- [200] A. J. H. McGaughey and J. M. Larkin. Predicting phonon properties from equilibrium molecular dynamics simulations. *to appear in Annual Review of Heat Transfer*, 17, 2013. A.4
- [201] L.D. Landau, E.M. Lifshitz, and L.P. Pitaevskii. *Statistical Physics, Part 2 : Volume 9*. Pt 2. Elsevier Science & Technology Books, 1980. A.4
- [202] A. Rajabpour and S. Volz. Thermal boundary resistance from mode energy relaxation times: Case study of argon-like crystals by molecular dynamics. *Journal of Applied Physics*, 108:094324, 2010. A.4